Studies on the Role of Surfactant Self-Assembly Templates in Pyrrole Polymerization and the Properties of Polypyrrole Particles

THANEEYA SAMWANG

NOVEMBER 2024

Studies on the Role of Surfactant Self-Assembly Templates in Pyrrole Polymerization and the Properties of Polypyrrole Particles

A dissertation submitted to

THE GRADUATE SCHOOL OF ENGINEERING SCIENCE

OSAKA UNIVERSITY

in partial fulfillment of the requirements for the degree of

DOCTOR OF PHILOSOPHY IN ENGINEERING

BY

THANEEYA SAMWANG

NOVEMBER 2024

Preface

This dissertation was conducted under the supervision of Professor Hiroshi Umakoshi in the Division of Chemical Engineering, Graduate School of Engineering Science, Osaka University, from 2021 to 2024.

This study has unveiled the novel and significant role of surfactants and polymerization methods in shaping morphology and enhancing the conductivity of polypyrrole based on the understanding of bipolaron structure, polaron structure, optical band gap and acyl chain packing density during self-assembly.

By understanding these factors, the author hopes that this research will spark a new wave of interest in the polypyrrole field and contribute to laying a foundation for future exploration to further design and develop particle morphology and alignment to improve the electrical performance of various electronic devices.

Thaneeya Samwang

Division of Chemical Engineering
Graduate School of Engineering Science
Osaka University
Toyonaka, Osaka, 560-8531, Japan

Abstract

PPy is a conductive polymer with applications in sensors, batteries, and electronics. Its electrical properties are strongly influenced by morphology and preparation methods. Despite advances in electrical and chemical polymerization, optimizing PPy's morphology and particle organization remains challenging. This work studied the impact of surfactant self-assembly templates on the polymerization of PPy, highlighting their role in shaping its structure and electrical properties. The scope was investigating the band gap, electrical conductivity, and the formation of bipolarons and polarons structures in PPy.

In Chapter 2, the study investigated the impact of SDS on PPy polymerization and its properties. SDS acted as a template, influencing PPy's morphology, electrical, and chemical characteristics. PPy polymerized in SDS formed sheet-like structures, while in its absence, only sphere-like forms appeared. The Raman spectra revealed that SDS altered the ratio of bipolarons to polarons, enhancing conductivity. While an increase in APS/Py ratio led to similar improvements in morphology and conductivity. The findings emphasize the role of SDS, Py, and APS proportions in shaping PPy's properties, offering insights for material design.

In Chapter 3, this chapter researched the relationship between the morphology of PPy and its electrical characteristics, with specific emphasis on the architecture of bipolarons and polarons. The study examined the impact of surfactants such as SDS, CTAB, and Tween 80 on the electrical conductivity of PPy. Out of these options, SDS greatly increased conductivity by enhancing the topologies of bipolarons. The study in this chapter proposed that the electrostatic interactions between positively charged PPy and negatively charged SDS facilitate the creation of bipolarons, which was essential for enhancing electrical performance.

In Chapter 4, the study showed that varying CTAB-SDS catanionic composition altered particle size, shape, and conductivity of PPy, with a 1:1 ratio leading to disc-like morphologies. Raman spectra and UV-Vis-NIR spectroscopy showed that higher SDS composition enhanced bipolaron formation and conductivity. A packing density study also indicated that surfactant composition affected the catanionic surfactant system's

ordered or disordered acyl chain arrangement, further influencing the morphology and electronic properties of PPy. These findings offered insights into designing conductive polymers using the CTAB-SDS system for tailored applications.

Chapter 5 presents a comprehensive strategy for preparing PPy particles, focusing on their physical structure and electrical conductivity. It included a survey of PPy film preparation methods and proposes an approach to building PPy films using preformed particles. The chapter also provided a comparative case study, evaluating various methodologies for PPY film construction. The cyclic voltammetry analysis highlighted vital differences in particle behavior, film structure, and resultant electrical performance, offering information for optimizing future conductive material designs.

Chapter 6 provides a summary of the findings from this study in the form of General Conclusions. Additionally, it offers suggestions for future work, building on the ideas presented and identifying new avenues for continued research and application of PPy material.

Contents

Chapter 1

General Introduction

1. Polypyrrole

Pyrrole is an organic compound that serves as the monomer unit for polypyrrole (PPy), a widely studied conductive polymer. Chemically, pyrrole is a five-membered aromatic heterocycle with the molecular formula C_4H_5N. It consists of four carbon atoms and one nitrogen atom in the ring, with a hydrogen atom attached to each carbon and one hydrogen attached to the nitrogen as illustrated in **Figure 1-1** (Balint et al., 2014). The unique properties of PPy arise from its conjugated polymer backbone, which features alternating single and double bonds that facilitate the delocalization of π-electrons along the polymer chain (Kausaite-Minkstimiene et al., 2015). This delocalization is crucial for electrical conductivity, as it allows π-electrons to move freely within the polymer.

PPy is renowned for its remarkable electrical conductivity, environmental stability, and ease of synthesis, making it one of the most extensively researched conducting polymers (Meng & Lin, 2023). Since its discovery, ongoing research into PPy has driven innovations across a wide range of applications, including biomaterials (George et al., 2005; Lin et al., 2018; Veisi et al., 2023), where its biocompatibility and stability offer significant advantages (Ashery et al., 2018; Ramanaviciene et al., 2010), biosensors (De Aguiar et al., 2021; Miah et al., 2022; Miao et al., 2018; Xiaoqiang et al., 2020), where its conductive and surface properties enhance sensitivity, and energy storage (X. Han et al., 2020; Shabeeba et al., 2022; Zang et al., 2017), where its efficient charge transfer capabilities are critical.

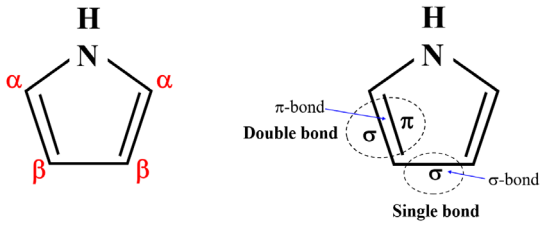

Figure 1-1. Pyrrole monomer and a simplified schematic of a conjugated backbone containing single and double bonds.

2. Pyrrole Polymerization and Properties Characteristics

PPy synthesis begins with the polymerization of pyrrole monomers, initiated either electrochemically or chemically. This process involves the oxidative coupling of pyrrole units to form conjugated PPy chains, as illustrated in **Figure 1-2**. During polymerization, oxidized pyrrole (Py) molecules react with other oxidized Py units to form dimers, trimers, and oligomers (Hou et al., 2014; Y. Wang et al., 2022). These oligomers serve as nuclei for the growth of PPy chains. The polymerization results in varying oxidative levels, which directly influence the structural and electrical properties of the resulting PPy.

The electrical conductivity of PPy, like that of other semiconductors, is related to its optical band gap, which represents the energy gap between its valence and conduction bands (**Figure 1-3**). The optical band gap is a critical property that affects charge carrier mobility and the material's reactivity (Iurchenkova et al., 2021; Salzner et al., 1998). PPy typically exhibits band gaps ranging from 1.00 eV to 3.10 eV (Atta et al., 2023; Bayat et al., 2021), depending on various pre- and post-synthesis parameters in the polymerization process, such as the type of counterions, degree of doping, and oxidation state (Chitte et al., 2011; Choudhury & Choudhury, 2012; Thompson et al., 2011; Y. Yang et al., 2010).

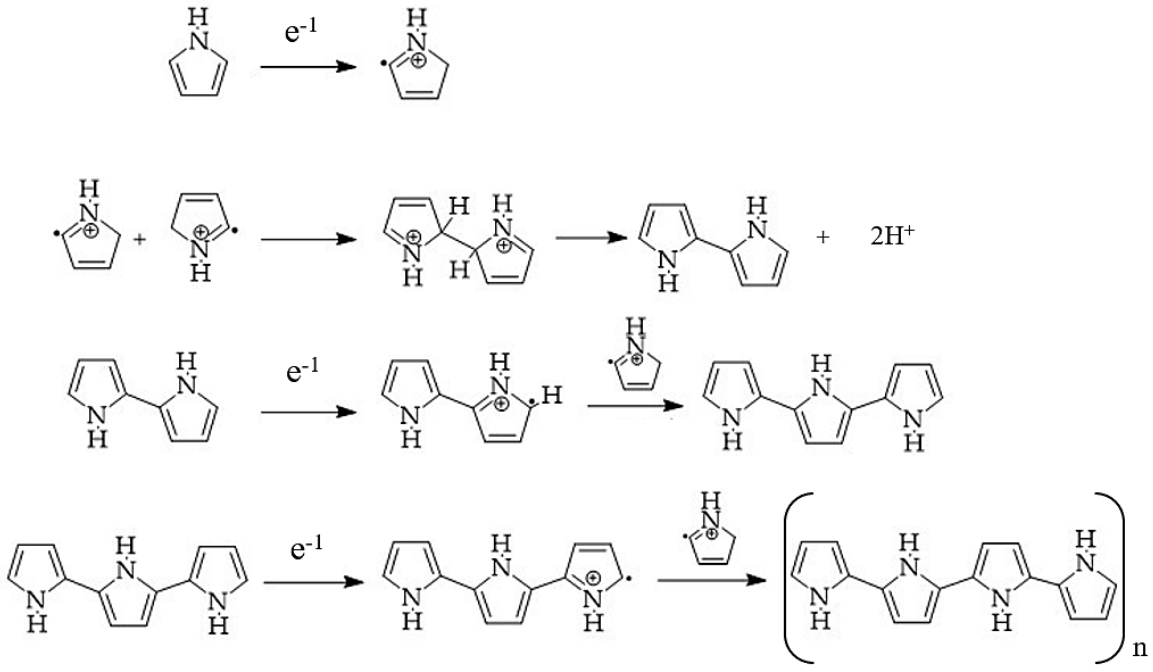

Figure 1-2. Illustration of the pyrrole polymerization.

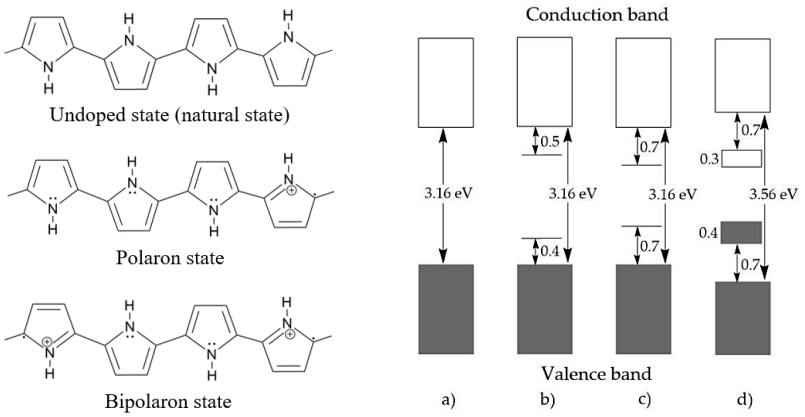

Figure 1-3. Chemical structure and electronic bands: a) undoped state, b) polaron state, c) bipolaron state, and d) fully doped state of PPy (Le et al., 2017).

The degree of oxidation in PPy is strongly associated with the formation of polarons and bipolarons, which are localized lattice distortions that increase the mobility of charge carriers (Gupta, 2008; Patil et al., 1988; M. Zhou et al., 2002). Brédas et al. (Scott et al., 1984) and Santos et al. (Santos et al., 2007) have shown that polarons are associated with lower oxidation states, whereas bipolarons are suggestive of greater oxidation levels. For instance, Bober et al. showed that the use of acid blue dyes in the production of PPy results in fluctuations in conductivity and affects the configuration of bipolarons and polarons, which can be analyzed using Raman spectroscopy (Bober et al., 2018).

Appel et al. utilized Ultraviolet photoemission spectroscopy (UPS) and Near edge X-ray absorption spectroscopy (NEXAFS) to examine how modifications in the dopant anion affected the electronic structure of PPy films (Appel et al., 1999). Their study found that pyrrole rings preferentially bind at the alpha-alpha (α-α) positions, although connections at the beta-beta (β-β) and beta-alpha (β-α) positions are also possible, as illustrated in **Figure 1-4**. These binding positions significantly influence the molecular structures of dimers and trimers and their corresponding oxidative states, which, in turn, impact the formation of polarons and bipolarons within PPy (Hong et al., 2024).

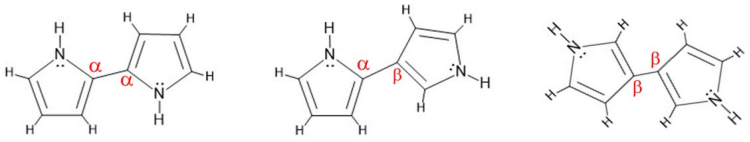

Figure 1-4. The molecular configuration of dimers with different interaction sites.

3. Polypyrrole Synthesis Methods

Electrochemical polymerization is a widely used method for synthesizing PPy. In this process, pyrrole monomers are polymerized on an electrode surface under an applied potential, allowing for precise control over the polymer's thickness, morphology, and doping level. This method is highly reversible and enables the doping of PPy with various anions, such as Cl^- and HSO_4^-, through the electrolyte solution, resulting in different conductivity levels. The fine-tuning of these parameters directly influences the electrical properties of the resulting PPy films, which often exhibit high conductivity, making them ideal for various electronic applications. However, this method requires specific equipment and controlled conditions.

Chemical polymerization involves the oxidation of pyrrole monomers using chemical oxidants, such as hydrogen peroxide (H_2O_2), ferric chloride ($FeCl_3$) or ammonium persulfate (APS) (Veisi et al., 2023; Wen et al., 2017). This method is well-suited for the bulk synthesis of PPy due to its scalability and relatively simple design. However, the morphology and properties of the resulting PPy can vary significantly based on the conditions of polymerization, for example concentration or type of the oxidant and the presence of surfactants. By carefully controlling these parameters, the electrical properties and morphology of PPy can be precisely tailored.

In addition to the substantial influence of the synthesis technique on the oxidation state in PPy, the selection of a dopant or template also enables a diverse range of morphologies. Researchers such as Ishpal et. al., (Ishpal & Kaur, 2013), Bober et al. (Bober et al., 2018), Trchová and Stejskal (Trchová & Stejskal, 2018), and Šetka et al. (Šetka et al., 2019) synthesized various PPy nanostructures, including nanorods, nanoparticles, and nanospheres, through chemical polymerization. Their investigations also revealed that the Raman spectra of these structures exhibited peak shifts that were directly associated with bipolarons and polarons. These shifts were correlated with the electrical characteristics of the PPy and were directly linked to the synthesis conditions.

An example of synthesis methods and conditions, including the use of oxidizers and surfactants, is provided in **Table 1-1**. PPy films are typically produced using the electrochemical polymerization method, as this process allows for the direct fabrication of PPy on an electrode. In contrast, chemical polymerization can yield a variety of PPy

morphologies, depending on the choice of oxidizer and template. **Table 1-2** provides a concise comparison of the advantages associated with each method in the context of polymerization, particularly for pyrrole. Each method has specific benefits that make it suitable for different types of polymerization processes.

Table 1-1. Summary of synthesis method and PPy product form.

Synthesis Method	Starting Material or Oxidizer	Template	Product Form	Ref.
Electrochemical polymerization	Py, alkoxysilanes, HCl	-	Film	Castro-Beltran et al., 2023
Electrochemical polymerization	Py, KCl	-	Thick film	Lakard et al., 2009
Electrochemical polymerization	Py, IC, KC, APS, methanol, ITO glass slides	-	Film	Rahaman et al., 2018
Electrochemical polymerization	Py, $NaClO_4$, NaCl, Na_2SO_4, $NaNO_3$, $NaBF_4$	SDS, CTAB, PVP	Thin film	Wysocka-Żołopa & Winkler, 2017
Electrochemical polymerization	Py	Anodized alumina oxide	Nanorod	Šetka et al., 2019
Chemical polymerization	Py, $FeCl_3$	PVA	Nanoparticles	Šetka et al., 2019
Chemical polymerization	Py, $FeCl_3$, APS	SDS	Particle	Yussuf et al., 2018
Chemical polymerization	Py, APS	SDS-CTAB	Nanoparticle	Dubey, 2023
Chemical polymerization	Py, KPS	CTAB, SDS	String bead, nanofiber	Khadem et al., 2017
Chemical polymerization	Py, HCl, H_2O_2	SDS	Nanoparticle	Leonavicius et al., 2011
Chemical polymerization	Py, APS	CTAB	Nanowire	Ren et al., 2023
Chemical polymerization	Py, $FeCl_3$	PVA	Nanosphere	Ren et al., 2023
Chemical polymerization	Py, $FeCl_3$	SDS	Nanoparticles	Ishpal & Kaur, 2013
Chemical polymerization	Py, $FeCl_3$	Methyl orange	Nanotube	Trchová & Stejskal, 2018

Table 1-2. Comparable aspect between chemical and electrical polymerization.

Aspect	Chemical Polymerization	Electrochemical Polymerization
Polymerization Method	Chemical reaction initiated by an oxidizing agent.	Electrochemical reaction initiated by applying a voltage to a monomer solution.
Initiation	Initiated by the oxidizing agent reacting with pyrrole monomers.	Initiated by applying a potential to the monomer solution, causing oxidation at the electrode surface.
Propagation	Pyrrole radical cations form and react with additional monomers, forming long chains.	Polymer chains grow directly on the electrode surface as the monomer is oxidized.
Termination	Chain growth terminates when monomers are depleted, or chains meet.	Chain growth stops when the applied potential is removed, or the monomer is depleted.
Morphologies	Nanoparticles, nanotubes, nanosheets, films, depending on conditions.	Typically films directly on the electrode; can be tailored by electrode type and applied potential.
Oxidizing Agent	Common oxidants include $FeCl_3$, APS, H_2O_2.	The oxidant is generated in situ at the electrode; no need for external oxidizing agent.
Role of Surfactants	Surfactants like SDS and CTAB guide morphology formation.	Surfactants are less commonly used but can influence film morphology when applied.
Doping	Doping occurs via incorporation of anions from the oxidant, leading to high levels of polarons/bipolarons.	Doping occurs simultaneously with polymerization; the dopant is usually the counterion from the electrolyte.
Control Over Properties	Morphology and properties depend on reaction conditions (e.g., oxidant, surfactant concentration).	High control over thickness, morphology, and uniformity by adjusting the applied voltage and time.
Scalability	Easily scalable for industrial applications.	Scale but more complex due to the need for electrochemical equipment.
Purity	Lower purity may contain residual oxidants and by-products.	Higher purity; fewer impurities as polymer forms directly on the electrode.
Cost-Effectiveness	Generally cost-effective due to simple reagents and conditions.	More expensive due to the need for specialized electrochemical equipment.
Applications	Sensors, energy storage devices, actuators, films.	Primarily used for films in sensors, electrochemical devices, and coatings.

4. Tuning PPy Morphology by Template

Template-assisted polymerization is a well-known technique that utilizes soft or hard templates in forming a certain physical morphology of a polymer. The use of templates enables the formation of well-defined nanostructures, such as nanospheres (Fan et al., 2015; Z. Zhou et al., 2019), nanotubes or nanowires (Deljoo Kojabad & Shojaosadati, 2016; Mao et al., 2017; Roohi et al., 2022), nanorings (Qin & Qiu, 2019), and nanosheets (Guan et al., 2019; Xie et al., 2023; X. Yang et al., 2016).

Hard templates, such as porous anodic alumina membranes (Deljoo Kojabad & Shojaosadati, 2016), silicon wafer (Shen et al., 2023), or polymers (Parayangattil Jyothibasu & Lee, 2020), guide the polymerization of pyrrole into specific nanostructures. After polymerization, the hard template is typically removed through chemical etching, leaving behind a nanostructured replica of the original template in the form of PPy. This technique is useful for creating well-defined geometries such as nanowires or hollow tubes.

The utilization of soft templates in polymerization has several notable benefits, particularly regarding the flexibility and ease it provides to the polymer structure. Soft templates, typically composed of organic compounds or block copolymers, allow for a more controlled and flexible synthesis process (Rahman Poolakkandy & Mol Menamparambath, 2020). The inherent flexibility of soft templates allows for a wider range of polymer sizes and shapes, tailored to specific application needs. Surfactants like fatty alcohol polyoxyethylene ether (Zhou et al., 2019), sodium dodecyl benzene sulfonate (SDBS) (J. Wang et al., 2023), or sodium dodecyl sulfate (SDS) (Jamdegni & Kaur, 2020) are commonly used as soft templates. These surfactants create nanoscale templates by self-assembling into micelles or other structures in solution, guiding the polymerization of monomers into various morphologies and sizes (Antony & Jayakannan, 2007; Dubey, 2023b; Molina et al., 2018; Zhang et al., 2006).

In addition to shaping the polymer's structure, surfactants like SDS and SDBS can also enhance the electrical conductivity of PPy (Omastová et al., 2003; Xing & Zhao, 2007). Interestingly, studies have shown that non-spherical PPy structures synthesized using cetyltrimethylammonium bromide (CTAB) exhibit higher electrical properties compared to spherical ones (Ren et al., 2023). Khadem et al. reported that PPy prepared with CTAB formed string-bead shapes with better conductivity than spherical structures

made with SDS under similar conditions (Khadem et al., 2017). Similarly, Yussuf et al. found that PPy synthesized in SDS with ferric chloride ($FeCl_3$) as an oxidizing agent developed a fibrillar morphology with slightly higher conductivity compared to PPy synthesized using ammonium persulfate (APS) as the oxidant (Yussuf et al., 2018). Surfactants can self-assemble into nanostructures like micelles, bilayers, and vesicles, making them effective in shaping the morphology of PPy. By using surfactants, PPy can be synthesized into specific forms such as sheets, fibres, or spheres.

5. Self-Assembly of Surfactant

Surfactants are amphiphilic molecules characterized by having both hydrophobic (water-repelling) and hydrophilic (water-attracting) regions. Due to this dual nature, surfactants can spontaneously arrange themselves into organized structures such as micelles or vesicles when dispersed in a solvent, particularly in aqueous solutions. This self-assembly is driven by the minimization of free energy as the hydrophobic parts seek to avoid water while the hydrophilic heads interact with it. These resultant structures can serve as versatile soft templates in various chemical processes, including the polymerization of pyrrole. This technique allows for the controlled synthesis of PPy with tailored morphologies that are essential for specific applications in electronics, sensors, and other advanced materials.

5.1. The packing parameter by Israelachvili

The type and shape of aggregates formed by surfactants in solution can be predicted using the concept of the packing parameter (P), introduced by Jacob Israelachvili (Israelachvili J., 2011). The packing parameter is a dimensionless number that provides insight into the preferred morphology of the amphiphilic molecules when they self-assemble. It is calculated using the formula:

$$P = \frac{V}{a_0 \cdot l_c}$$

where V presents the volume of the hydrophobic tail, a_0 presents the area of the hydrophilic head group, l_c presents the length of the hydrophobic tail.

Depending on the value of *P*, different self-assembled structures can form various structures. Surfactants with a small hydrophobic volume (low *P* value) tend to form small spherical micelles in aqueous solutions. These micelles, typically 5 nm to 10 nm in diameter, represent the simplest form of surfactant aggregates. When the hydrophobic portion is slightly larger, cylindrical micelles or rod-like structures can form. As the hydrophobic volume increases further, surfactants may arrange into bilayers or lamellar phases, which are more complex and can be seen in the formation of vesicles or lipid bilayers, summarily as shown in **Figure 1-5**. These formations are also influenced by external factors such as amphiphile concentration, temperature, ionic strength, and pH. Therefore, while the molecular structure provides a basic guide, the actual morphology can vary based on environmental conditions.

5.2. Critical micelle concentration (CMC)

CMC is a fundamental concept in surfactant chemistry. It defines a low concentration range of surfactants that are required to form micelles, which are one of the colloidal association structures (Kim & Lim, 2004). Below the CMC, surfactant molecules exist primarily as monomers. However, as the concentration increases and surpasses the CMC, these monomers start to aggregate into micelles. The CMC is not a fixed point but rather a dynamic equilibrium where there is a constant exchange between free surfactant molecules and those assembled into micelles. This exchange is essential for maintaining the structural integrity of micelles in reaction to environmental changes, such as dilution or temperature fluctuations. Understanding the CMC of a surfactant is crucial for its effective use in various applications, including the controlled polymerization of pyrrole, where the concentration must be carefully managed to achieve the desired morphological outcomes. Examples of surfactants used with PPy, along with their chemical structures and respective CMC values, are briefly summarized in **Table 1-3**.

(a)

Packing parameter of factor $= \frac{v}{a_0 l_c}$

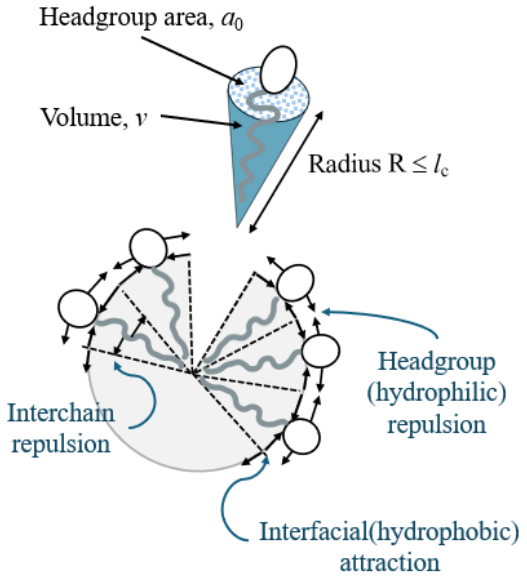

(b)

Critical packing parameter $v/a_0 l_c$	Critical packing shape	Structures formed
< 1/3		
1/3 – 1/2		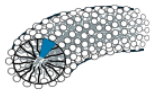
1/2 – 1		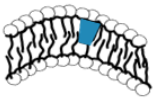
=1		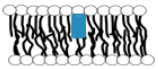
>1		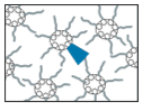

Figure 1-5. (a) The interiors structure of micelles: v represents the chain volume, l_c represents chain length, a_0 represents head group area and (b) critical packing shape depends on critical packing parameter (Israelachvili J., 2011).

Table 1-3. Type of surfactants.

Surfactant Name	Chemical Formula	Chemical Structure	Type of Surfactant	Approximate CMC (mM)	Advantage	Disadvantage
Sodium Dodecyl Sulfate (SDS)	$C_{12}H_{25}NaO_4S$	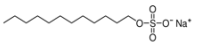	Anionic	8	Cost-effective, good solubility	High Ionic strength, sensitivity to pH
Cetyltrimethylammonium Bromide (CTAB)	$[(C_{16}H_{33})N(CH_3)_3]Br$	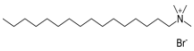	Cationic	0.9	Good micelle formation	Expensive, potential toxicity
Polysorbate 80 (Tween 80)	$C_{64}H_{124}O_{26}$	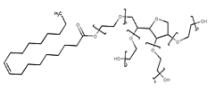	Non-ionic	0.02	Biocompatible	Lower surface activity, high viscosity
Triton X-100	$C_{14}H_{22}O(C_2H_4O)n$	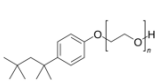	Non-ionic	0.24	Mild conditions	Non-biodegradable, lower efficiency
Dodecylbenzenesulfonic Acid (DBSA)	$C_{18}H_{29}SO_3H$	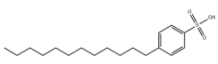	Anionic	1.0	Strong anionic surfactant, good emulsifier	Corrosive, expensive
Hexadecyltrimethylammonium Chloride (CTAC)	$C_{19}H_{42}ClN$	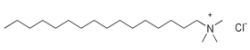	Cationic	0.3	Stable micelle formation	Expensive, potential toxicity

6. Overview of This Study

PPy is a conductive polymer with applications in sensors, batteries, and electronics. Its electrical properties are strongly influenced by morphology and preparation methods. Despite advances in electrical and chemical polymerization, optimizing PPy's morphology and particle organization remains challenging. This work studies the impact of surfactant self-assembly templates on the polymerization of PPy, highlighting their role in shaping its structure and electrical properties. The scope is investigating the band gap, electrical conductivity, and the formation of bipolaron and polaron structures in PPy.

In Chapter 2, the study investigated the impact of varying monomer concentrations, SDS, and concentrations on the polymerization and morphology of PPy. It highlighted the role of SDS in chemical polymerization, where the formation of micelles led to sheet-like morphologies, with conductivity increasing as the band gap decreased. Notably, varying SDS concentrations between 0.01 M to 0.30 M revealed that significant morphological changes occur, affecting the electronic properties. An increase in the APS/Py ratio similarly caused changes in morphology, resulting in enhanced conductivity. In the absence of SDS, however, no substantial variations in morphology were observed, underscoring the critical role of surfactants in modifying PPy properties.

In Chapter 3, the study focused on the relationship between PPy morphology and its electronic properties, particularly in terms of bipolaron and polaron structures. Using different surfactants such as SDS, CTAB, and Tween 80, this study examined how these agents influence the C–H deformation region and ultimately affect conductivity. SDS was found to have the most significant impact, improving conductivity by enhancing the bipolaron structure. This work suggested that the electrostatic interaction between the positively charged PPy and negatively charged SDS molecules may play a crucial role in improving electrical performance by promoting bipolaron formation.

In Chapter 4, the catanionic system composed of CTAB and SDS was investigated in this chapter, particularly its influence on PPy morphology and electronic properties. The study revealed that varying the CTAB-SDS composition significantly affected particle size, shape, and packing density, with a 1:1 ratio leading to disc-like morphologies. Raman spectroscopy indicated that SDS-rich samples exhibited enhanced

bipolaron structures, which correlate with higher conductivity. This work also discussed the importance of surfactant composition in determining the oxidative structure and electrical properties of PPy, providing insighted into the role of packing density and micelle formation in defining its morphology and performance.

In Chapter 5, the chapter presents a strategy for preparing PPy particles, focusing on their physical structure and electrical conductivity. It includes a survey of PPy film preparation methods and proposes an approach to building PPy films using preformed particles. The chapter also provides a comparative case study, evaluating various methodologies for PPY film construction. The cyclic voltammetry analysis highlighted vital differences in particle behaviour, film structure, and resultant electrical performance, offering information for optimizing future conductive material designs.

Chapter 6 provides a summary of the findings from this study in the form of General Conclusions. Additionally, it outlines Suggestions for Future Works as an expansion of the ideas presented in this thesis.

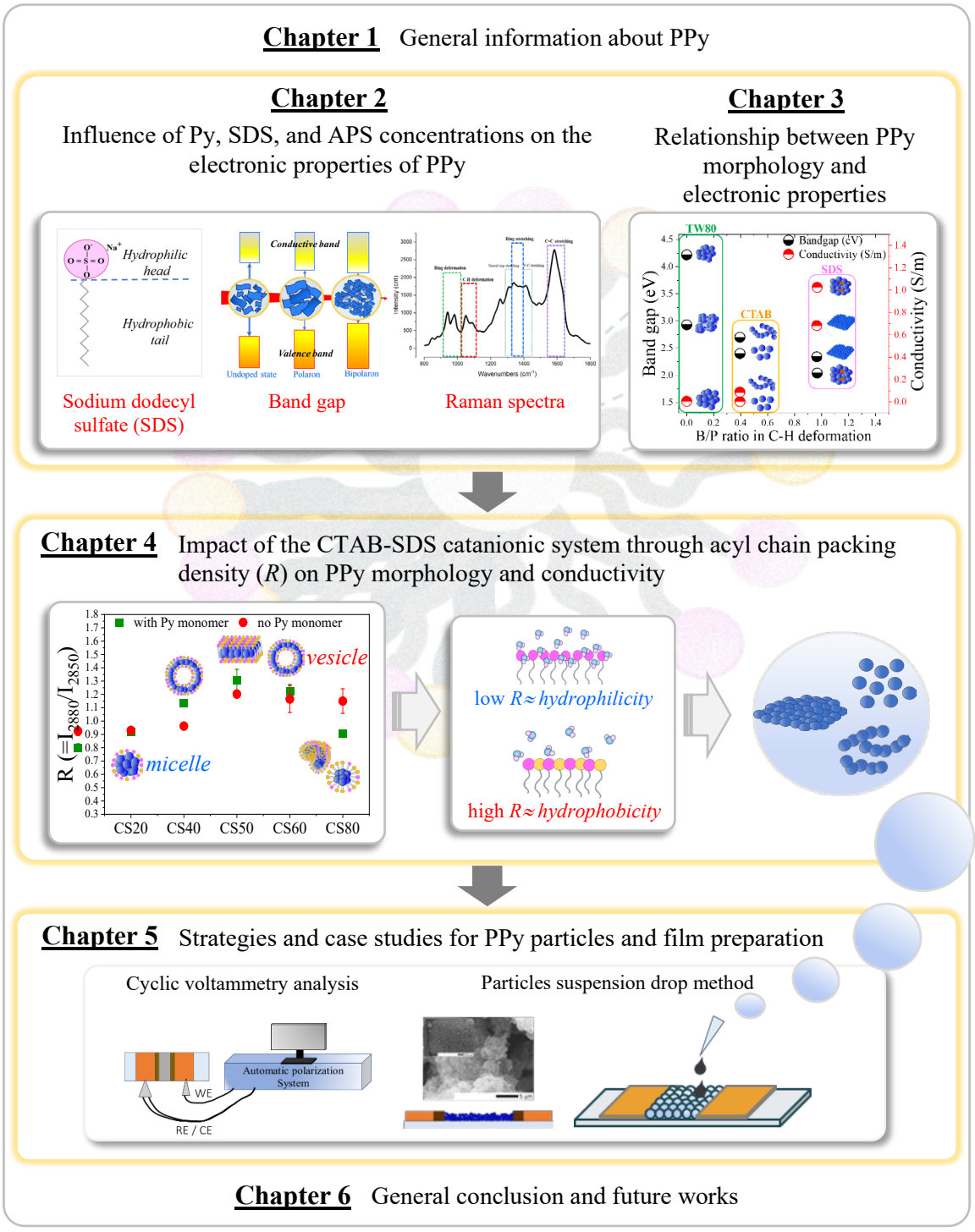

Figure 1-6. Concept map of the present study.

General Information

Chapter 1: General Information

1. Polypyrrole
2. Pyrrole Polymerization and Properties Characteristics
3. Polypyrrole Synthesis Methods
4. Tuning PPy Morphology by Template
5. Self-Assembly of Surfactant
6. Overview of This Study

Pyrrole Polymerization and Characterization

Chapter 2: Study of Chemical Polymerization of Polypyrrole with SDS Soft Template: Physical, Chemical, and Electrical Properties (Paper 1)

- Define the optimal concentration of Py, SDS and APS for chemical polymerization.
- Evaluate electronic properties of PPy prepared with and without using SDS as soft template.
- Define the relationship between electronic properties and PPy size.
- Evaluate the effect of SDS on bipolarons and polarons structure by determining the ratio of peak intensity from Raman spectra.

Chapter 3: Exploring the Influence of Morphology on Bipolaron–Polaron Ratios and Conductivity in Polypyrrole in the Presence of Surfactants (Paper 2)

- Analysis of bipolaron and polaron ratio in the C–H deformation region of PPy prepared with different surfactants and oxidizing agents.
- Exploring the importance of SDS existence in PPy for electrical conductivity improvement.

Tailoring Polypyrrole Morphology and Electronic Properties

Chapter 4: Tailoring Polypyrrole Morphology and Electronic Properties through CTAB-SDS Self-Assembly (Paper 3)

- Study the Py polymerization in a combination surfactant between CTAB and SDS.
- Evaluate morphology and electronic properties of PPy.
- Investigate acyl chain packing to interpret the behaviours of CTAB-SDS assembly when Py or PPy presence.

Strategies and Case Studies

Chapter 5: Strategies and Case Studies for PPy Particles and Film Preparation

- Strategies for Py polymerization using surfactant self-assembly template.
- Survey of PPy film fabrication.
- Case studies for film preparation.

Conclusion

Chapter 6: General Conclusion

- General conclusion.
- Challenging in the future.

Figure 1-7. Framework of the present study.

Chapter 2

Study of Chemical Polymerization of Polypyrrole with SDS Soft Template: Physical, Chemical, and Electrical Properties

1. Introduction

Conductive polymers are a group of conjugated polymers that have the ability to incorporate counter ions and become semi-conductive material. They are flexible, lightweight, and easy to process, similar to a polymer. They enable charge transfer and offer moderate conductivity akin to that of semiconductors. These outstanding properties of conductive polymers make them promising candidates for various applications, including sensor devices, surface coatings, electronic circuits, energy storage devices, and medical equipment (George et al., 2005; Lin et al., 2018; Veisi et al., 2023). Example of conductive polymers include polythiophene, polyaniline, and polypyrrole (PPy). PPy has gained considerable attention from researchers worldwide because of its high conductivity, thermal stability and biocompatibility (Ashery et al., 2018; Ramanaviciene et al., 2010).

The electrical conductivity of a semiconductor is associated with its optical band gap, which is the difference between the gap energy of its valence and conduction bands. The optical band gap of a semiconductor is one of its crucial properties that indicates the mobility of the charge carriers in the semiconductor and the activities involved in the reactions and interactions within it (Iurchenkova et al., 2021; Salzner et al., 1998). PPy offers band gaps of 1.00 eV and 3.10 eV depending on its pre- and post-synthesis parameters in the polymerization process (Atta et al., 2023; Bayat et al., 2021), such as the type of counter ions, degree of doping, and oxidation state (Chitte et al., 2011; Choudhury & Choudhury, 2012; Thompson et al., 2011; Y. Yang et al., 2010). Chemical polymerization is a simple method of synthesizing PPy via an oxidation-reduction reaction and applying it to industrial-scale production. This method requires the use of oxidizing agents, such as ferric chloride or ammonium persulfate, to oxidize the pyrrole monomer (Py) and initiate the polymerization process.

The oxidized Py reacts with the remaining Py or other oxidized Py to form dimers, trimers, and oligomers (Hou et al., 2014; Y. Wang et al., 2022). The oligomers produce nuclei and PPy. The degree of oxidation of PPy is associated with the presence of polarons and bipolarons – localized lattice distortion defects in polymeric structure that drive charge carrier mobility (Gupta, 2008; M. Zhou et al., 2002), in which polarons and bipolarons represent a low and high oxidative states, respectively (Appel et al., 1999; Brédas et al., 1984; Santos et al., 2007). The formation of polarons and bipolarons depends heavily on synthesis conditions and contributes to the morphology, chemical, and electrical properties of the PPy. Santos et al. and Pang studied chemical polymerization of PPy relying on Raman spectroscopy analysis (Pang, 2020; Santos et al., 2007). They reported that Py rings preferentially bind at the alpha-alpha (α-α) positions but can connect at the beta-beta (β-β) and beta-alpha (β-α) positions. The binding positions affect molecular structures of dimers and trimers as well as their oxidative states, which are represented in terms of bipolarons and polarons of the PPy. Ishpal et al., Bober et al., Trchová et al., and Šetka et al. synthesized the different PPy nanostructures, such as nanorods, nanoparticles, and nanospheres, based on chemical polymerizations (Bober et al., 2018; Ishpal & Kaur, 2013; Šetka et al., 2019; Trchová & Stejskal, 2018). Raman spectra showed that peak spectra of bipolarons and polarons were associated with synthesis conditions, and were correlated to morphological, chemical, and electrical properties of the PPy.

Template-assisted polymerization is a well-known technique that utilizes soft or hard templates in forming a certain physical morphology of a polymer. The technique was demonstrated in a synthesis of various PPy nanostructures, including nanospheres (Fan et al., 2015; Z. Zhou et al., 2019), nanotubes or nanowires (Deljoo Kojabad & Shojaosadati, 2016; Mao et al., 2017; Roohi et al., 2022), nanorings (Qin & Qiu, 2019), and nanosheets (Guan et al., 2019; Xie et al., 2023; X. Yang et al., 2016). In a hard template technique, a solid mold was applied for a polymerization, providing the physical morphology that the polymer grew in and subsequently adopted. The soft template, on the other hand, exercised the concept of self-assembly polymerization, relying on a unique reaction/interaction between a monomer and a soft template substance in attaining a designed physical morphology. Sodium dodecyl sulfate (SDS) is an anionic surfactant that has widely been studied for its ability as a soft template. Utilization of SDS in a soft-

template polymerization of PPy yielded icosahedrons (Zhang et al., 2006) spherical, (Direksilp & Sirivat, 2020; Gangopadhyay, 2012; Hazarika & Kumar, 2013), cylindrical and elongated structures (Gangopadhyay, 2012; Hazarika & Kumar, 2013), and was also reported to promote electrical conductivity (Xing & Zhao, 2007; Zhang et al., 2006). Regardless of the popularity of the SDS, the mechanisms underlying the relationship between physical, chemical and electrical conductivity are not fully understood. A study on the use of SDS-assisted chemical polymerization for PPy synthesis can deepen our understanding of the molecular-level phenomena and affect the other properties of PPy.

This chapter aimed to investigate (1) the effects of SDS on the chemical polymerization of PPy and (2) explored the relationship among PPy properties, focusing on size, morphology, optical band gap, resistance and bipolarons/polarons ratios. Py was polymerized in the presence of SDS with ammonium persulfate (APS) as an oxidizer. Synthesis parameters, including SDS concentration, Py concentration, and APS/Py ratio, were varied and studied.

2. Materials and Methods

2.1. Materials

The Py used in the experiments (98% reagent grade, Sigma-Aldrich Co. LLC, St. Louis, MO, USA) was refrigerated before its use. SDS and APS were provided by Wako Pure Chemical Industries Ltd., Osaka, Japan. All aqueous solutions were prepared using ultrapure water (18.20 MΩ resistance, Direct-Q 3 UV, Merck Millipore, Osaka, Japan). Indium tin oxide (ITO) glass electrodes were purchased from BAS Inc. Tokyo, Japan. Silver paint (resistance ≤ 1.00 Ω) was purchased from Polycalm, Japan. All the electrochemical tests were conducted using an Automatic polarization system (HZ7000, Hokuto Denko Corporation, Tokyo, Japan).

2.2. Polypyrrole synthesis

Chemical polymerization was employed to synthesize PPy samples. Py was first added to the SDS solution, and the mixture was then agitated for 2 hours at an ambient temperature of 25 °C. Following that, an APS solution was gradually put into the mixture. By altering the APS/Py ratio as well as the Py and SDS concentrations, the author

investigated the impact of Py, SDS, and APS concentrations on polymer synthesis. The mixture was stirred for 24 hours at room temperature (25 °C) (**Scheme 2-1**) and a dark blue PPy powder suspension was obtained. It was dialyzed in ultrapure water to remove any unreacted monomer, as well as SDS, and APS from the synthesized PPy. PPy was obtained as a slurry, freeze-dried, and stored in a desiccator until its use. To study the effect of Py on PPy, the Py concentration (APS/Py ratio is 1.00) was varied while maintaining the SDS concentration constant at 0.10 M. To study the effect of SDS on PPy, the Py and APS concentrations were set at 0.04 M while varying the SDS concentrations. To study the effect of APS on PPy, the APS and Py molar ratio (APS/Py) was varied from 0.05 to 3.50, while the concentration of SDS was 0.10 M and the Py concentration was 0.04 M.

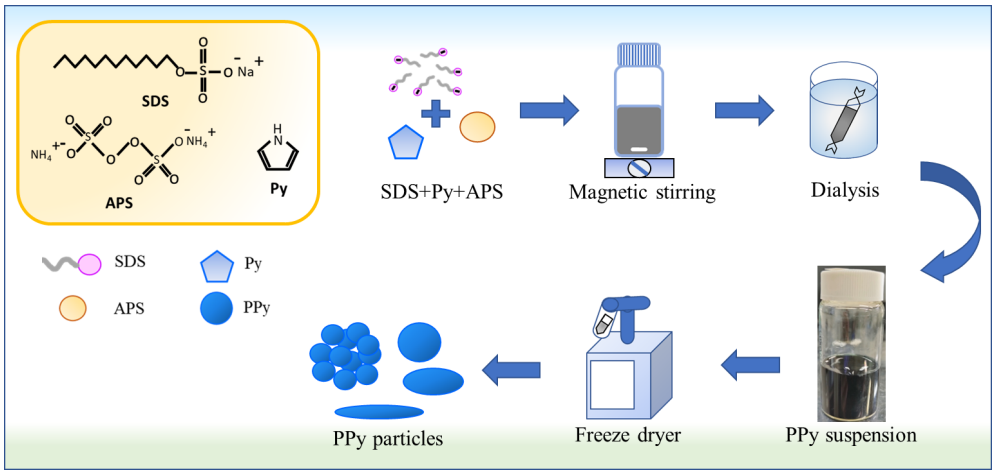

Scheme 2-1. Schematic diagram of PPy polymerization.

2.3. Sample characterizations

2.3.1. Particle size distribution and zeta potential

PPy was suspended in ultrapure water (0.10 – 0.20 mg/ml). The suspension was tested for particle size and zeta potential using Zetasizer apparatus (ZEN5600, Zetasizer manufactured by Malvern Instruments Ltd., Worcestershire, United Kingdom) based on the method of dynamic light scattering (DLS) and electrophoretic light scattering (ELS), respectively.

2.3.2. Scanning Electron Microscopy (SEM)

The dried PPy powder was obtained from the freeze-dryer and stored in a desiccator until analysis. The morphology of dried PPy powder was analysed by a scanning electron microscopy (JCM-7000, JEOL Ltd., Japan).

2.3.3. UV-Vis-NIR absorbance and optical band gap

The optical properties of PPy were analysed using UV-Vis-NIR spectroscopy (UV1800, SHIMADZU, Japan). PPy was diluted and suspended in ultrapure water (0.10 – 0.20 mg/ml) in a quartz cuvette with a 10 mm path length. The light absorbance of the samples was monitored and analysed based on the optical band gap determined using Tauc's correlation, as shown in Equation 1.

$$(\alpha h\nu)^{1/n} = \alpha_0(h\nu - E_g) \quad (1)$$

where α is the absorption coefficient ($2.302 \times A/d$), d is the cell thickness (1 cm), A is the light absorbance, $h\nu$ is the photon energy (eV), h is the Planck's constant (6.6261×10^{-34} J·s), and ν is the photon frequency with $\nu = C/\lambda$ where C = speed of light (2.998×10^{8} m/s) , λ is the wavelength (nm), photon energy (eV) is $1240/\lambda$., E_g is the optical band gap (eV), α_o is a constant band-tailing parameter, and n is the power factor ($n = 2$ for an indirect transition band gap) (Lertthanaphol et al., 2022; Lin et al., 2018). The plot of $(\alpha h\nu)^{1/n}$ versus photon energy ($h\nu$) will be a straight line within a specific region. The band gap was obtained by extrapolating the straight-line intercept along the ($h\nu$)-axis.

2.3.4. Electrical conductivity analysis

The PPy powder was cast into pellets (0.005 g/cm^2) using a hand press and sandwiched between two Indium Tin Oxide (ITO)-coated glass electrodes (**Scheme 2-2**). The distance between the electrodes and the thickness of the pellet were maintained at their initial values by using 0.80 mm thick silicone rubber. The resistance of PPy was monitored using a two-point probe measurement technique in the linear sweep voltammetry mode (LSV) with a potential window between –1.80 V and +1.80 V, scanned at a rate of 50 mV/s with 10 points recorded per scan. The data were monitored and recorded using an Automatic polarization system (HZ-7000, Hokuto Denko Corporation, Tokyo, Japan), connected to a personal computer. The resistance values were measured

and averaged across three separate measurements. After each measurement, the PPy sample was removed and replaced with fresh PPy powder. The resistance value was obtained from the slope of an *I/V* plot based on Ohm's law. The conductivity of PPy was determined using the correlations shown in Equations (2) and (3).

$$\rho = \frac{RA}{L} \tag{2}$$

$$\sigma = \frac{1}{\rho} \tag{3}$$

where R is the resistance of PPy (Ω), ρ is the resistivity of PPy (Ω·m), is the thickness of silicon rubber (8.00 x 10^{-4} m), is the area of the sample (1.96 x 10^{-5} m^2), and is the electrical conductivity (S/m).

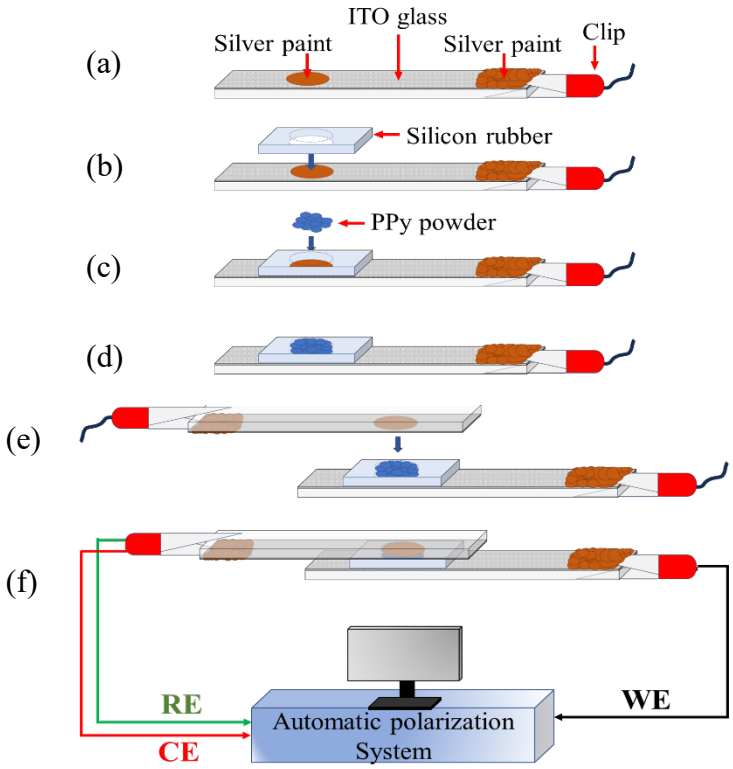

Scheme 2-2. Scheme of resistance measurement system: (a) Silver paint was applied to the ITO glass in the region that contacts the PPy powder, as well as on the clip connected between the ITO electrode and the Automatic polarization system. (b) A silicon rubber sheet with a hole, was placed on the ITO electrode, over the silver paint. (c)-(d) PPy powder was pressed into the hole of the silicon rubber. (e)-(f) Another ITO electrode was then sandwiched with the first ITO electrode and connected to the Automatic polarization system.

2.3.5. Raman spectroscopy

The Raman spectra of PPy were investigated from a Raman spectrometer (HR-800, Horiba Ltd., Kyoto, Japan) with a laser excitation wavelength of 532 nm. The peak intensities (*I*) of the bipolarons and polarons in PPy (**Table 2-1**) were analysed using OriginPro software (OriginPro, Version 2023. OriginLab Corporation, Northampton, MA, USA). The ratio of the peak intensity of bipolarons to that of polarons was then determined.

Table 2-1. Peak attribution reference of Raman spectra at different excitation wavelengths.

	Laser Excitation at			
Attribution	**785 nm***	**633 nm***	**514 nm***	**532 nm**
C-C ring deformation in bipolarons	939, 922-930	935, 934	932	926-927
C-C ring deformation in polaron structure	980, 966-980	985, 969	975	963-985
C-H deformation in polaron structure	1056, 1055	1054	1050	1050-1056
C-H deformation in bipolaron structure	1089, 1079-1083	1087	1083	1079-1084
Neutral ring deformation	1297, 1238	1304-1249	-	1253-1258
Ring stretching in polaron structure	1327,1334-1344	1338-1334	1326	1330-1344
Ring stretching in bipolaron structure	1375, 1374-1383	1381-1385	1378	
C-H and C-N stretching	1414	1417	1410	1410-1417
C=C stretching in polaron structure	1591	1592-1589	1578	1562-1593
C=C stretching in bipolaron structure	1600	1618-1609	-	-

* (Trchová & Stejskal, 2018)

3. Results and Discussion

3.1. Physical characterization

PPy samples were synthesized in the presence of SDS, which served both as a surfactant and as a counter ion. As a surfactant, SDS interacts with Py and other radicals

in polymerization solutions and determines the physical shape of the PPy. As a counter ion, SDS incorporates a negative polar on the polymeric chain, promoting a degree of oxidation for PPy. In the first operation, PPy was synthesized with varied Py (0.01 M to 0.30 M) and a constant SDS concentration (0.10 M). DLS analysis revealed the average particle size of PPy ranged from 88.40 nm to 94.20 nm for a Py concentration of 0.01 M to 0.04 M. The polydispersity index (PdI) is defined by Malvern Panalytical Co. Ltd. as a calculated dimensionless number (**Figure 2-1a**), showing dispersibility between 0.05 (mono disperse) and 0.70 (broad size distribution). At 0.01 M to 0.04 M Py, the PdI decrement suggested a higher degree of uniform distribution in PPy chain length for increased Py concentration. An increase in Py concentration from 0.04 M to 0.30 M raised the particle size from 94.20 nm to 604.50 nm and PdI values from 0.15 to 0.47, which indicated higher chain length distribution. In the second operation, the effects of SDS concentration (0.01 M to 0.30 M) on PPy formation at constant Py concentration (0.04 M) were studied.

The selected range of SDS concentration exceeded the critical micelle concentration (CMC) of 0.008 M (Qin & Qiu, 2019; Roohi et al., 2022), signalling that SDS micelles were formed. As the SDS concentration expanded from 0.01 M to 0.10 M, the average particle size of PPy dropped from 253.90 nm to 100.10 nm, corresponding to a PdI of 0.39 and 0.16. The results agree with those of previous studies (Šetka et al., 2019; X. Yang et al., 2016; M. Zhou et al., 2002), showing a reduction in particle size with increasing surfactant concentration. As the SDS concentration increased from 0.10 to 0.30 M (**Figure 2-1b**), the particle size increased from 100.10 nm to 163.10 nm, and the PdI increased from 0.16 to 0.26. In the third operation, the effect of APS was assessed from the molar ratio of APS/Py. When the APS/Py ratio increased from 0.10 to 3.50, the particle size of PPy increased from 73.50 nm (PdI = 0.25) to 557.90 nm (PdI = 0.37) (**Figure 2-1c**). APS in the mixture served as an oxidizing agent that reacted directly with Py monomer, initiating the chemical polymerization. As the APS/Py ratio increased, the polymerization rate rose, yielding increased particle size. The results provide strong evidence of the direct consistency between the PPy particle size and PdI values.

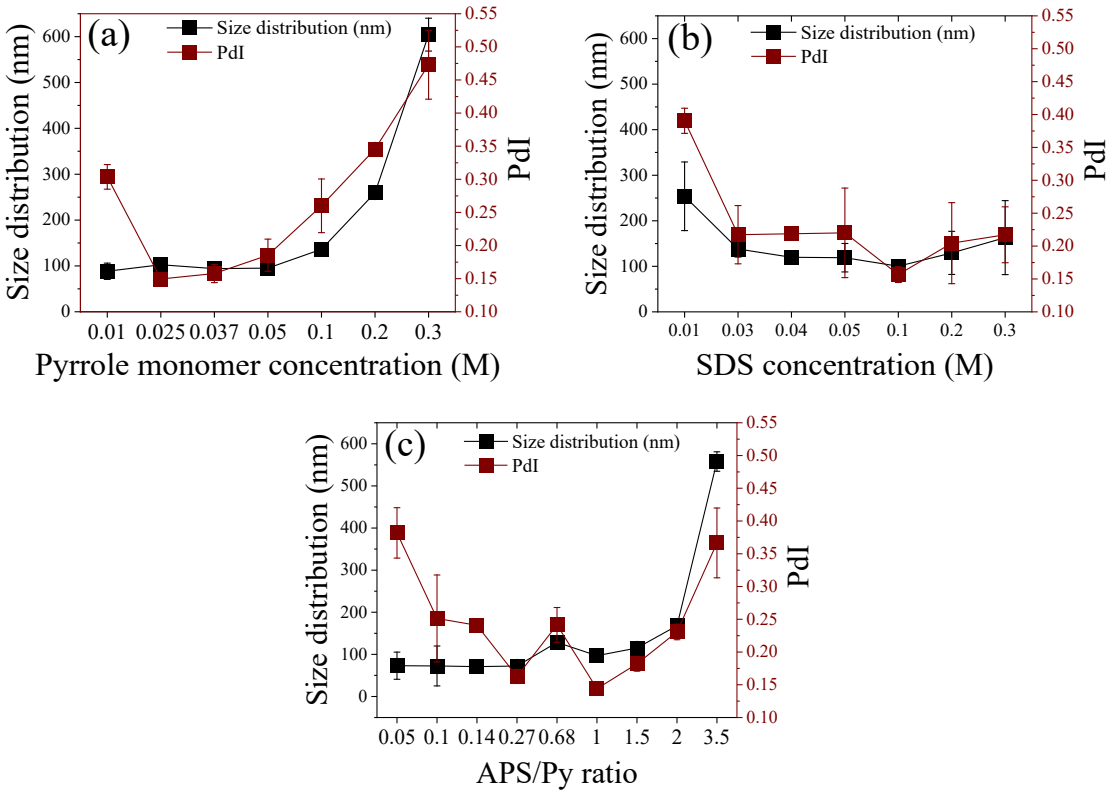

Figure 2-1. Average size distribution and PdI of PPy synthesized using (a) varied Py monomer concentration at 0.10 M SDS and APS/Py ratio of 1.00, (b) varied SDS concentrations, 0.04 M Py, and APS/Py ratio of 1.00, and (c) varied APS concentrations (represented by varying APS/Py molar ratio), 0.10 M SDS, and 0.04 M Py.

SEM was used to analyse the physical morphology of the PPy samples (**Figure 2-2**). The SEM images showed that PPy had a variety of shapes and that it firmly relies on the synthesis parameters, namely Py concentration, SDS concentration, and APS/Py ratio (Xie et al., 2023)**.** The particle size was determined from images using the ImageJ program (ImageJ Version 1.53 K, National Institutes of Health, USA). **Figure 2-2a** shows the SEM images of PPy samples from the first operation, with Py concentrations varying from 0.01 (Left) to 0.04 M, 0.20 M, and 0.30 M (Right). For 0.01 M Py, the PPy sample was a combination of sheets and particles with an average size of 0.94 µm. For 0.04 M Py, PPy became a sheet-like structure with an average length of 8.93 µm. As the Py concentration increased from 0.20 M to 0.30 M, PPy aggregated and acquired an irregular shape with an average particle size of 33.77 µm and 12.55 µm, respectively (**Scheme 2-3**). SEM images of PPy samples from the second operation (**Figure 2-2b**) provided

information on SDS concentration effects on the physical morphology of PPy. The PPy sheets appeared smaller, changing from 11.01 μm to 6.93 μm, as the SDS concentration increased from 0.01 M to 0.10 M. The increase in SDS concentration to 0.20 M and 0.30 M enlarged the size of the PPy sheets into 14.81 μm and 9.27 μm. PPy samples from the third operation revealed that variations in the APS/Py ratio led to different polymerization rates and physical structures (**Figure 2-2c**). As the ratio increased from 0.27 to 0.68, the PPy shape changed from a combination of particle and sheet shape (3.17 μm) to a sheet-like form (11.62 μm). The sheets grew to 21.76 μm and 12.86 μm, corresponding with the ratios of 1.5 and 3.5. A set of control experiments was studied by performing chemical polymerization in the absence of SDS (**Figure 2-2d**) and varying the concentration of Py from 0.01 M to 0.04 M, 0.10 M, and 0.30 M (APS/Py ratio of 1.00). PPy samples were assigned as PPy* (PPy synthesized in the absence of SDS) exhibited particle morphology with average sizes of 646 nm (Left), 614 nm, 718 nm, and 667 nm (Right), respectively.

During chemical polymerization, SDS was a bifunctional substance, acting as a soft template in forming PPy sheets and doping PPy for enhanced electrical conductivity (Qin & Qiu, 2019; Roohi et al., 2022). In its soft template role, SDS established micelles at a concentration higher than its CMC of 0.008 M. The micelles became compact when the SDS concentration increased, yielding micellar lamellae or hexagons at an extra-high SDS concentration (Guan et al., 2019; Hoshina et al., 2012). In the presence of water, the SDS molecules turn hydrophilic parts toward water, hiding hydrophobic branches inside the micelles. The Py monomer is a hydrophobic substance (Log P = 0.75, where P is the partition coefficient between octanol and water), and it could be surrounded by SDS, allowing the hydrogen in the Py to interact with the hydrophobic branches in SDS. The interactions result in Py distribution and particle formation at the micelle centre. The zeta potentials of PPy and PPy* were monitored using DLS, and their observed values were in the ranges of -32 mV to -20 mV and 20 to 25 mV, respectively. The potential suggested that chemical polymerization had occurred and that PPy had been formed and cooperated with the micelles. The polymerized PPy was encapsulated by SDS, which prevented it from aggregating with other particles. The phenomenon resulted in the dispersion of PPy colloids and the formation of a sheet-like PPy structure. Such a phenomenon, however, was limited to synthesis conditions in which the amount of Py, SDS, and APS were balanced. **Figure 2-2a** shows, at a low Py concentration of 0.01 M, PPy consisting of

particles and a sheet-like form. As the Py concentration increased from 0.04 M to 0.10 M, a sheet-like PPy structure was formed. At a Py concentration of 0.20 M and 0.30 M, PPy overgrew to create an irregular structure.

The effect of SDS concentration on PPy growth was studied next (**Figure 2-2b**). The sheet-like PPy structure increased in size as the SDS concentration increased from 0.01 M to 0.04 M, and 0.10 M and appeared to be constant as the SDS concentration of 0.30 M was realized. **Figure 2-2c** presents the effects of the APS/Py ratio on PPy morphology. PPy was polymerized at varied APS/Py ratios, 0.10 M SDS and 0.04 M Py. The APS/Py ratio of 0.27 yielded a combination of PPy particles and sheets, while the ratios of 0.68, 1.50, and 3.50 revealed large PPy sheets. The effects of SDS on PPy formation are summarized in **Scheme 2-4**. SDS micelles were loosely assembled at a low SDS concentration (0.01 M), fully assembled at a moderate SDS concentration (0.04 M) and expanded at high SDS concentrations (0.20 M and 0.30 M) (**Scheme 2-4a**). Py interacted with and was encapsulated within the micelles (**Scheme 2-3b**). As the Py reacted with APS, polymerization occurred (**Scheme 2-4c**) and continued growing inside the micelles (**Scheme 2-4d**). Py polymerized in SDS micelles and formed a sheet-like structure, as observed from the SEM image after freeze-drying (**Scheme 2-4e**).

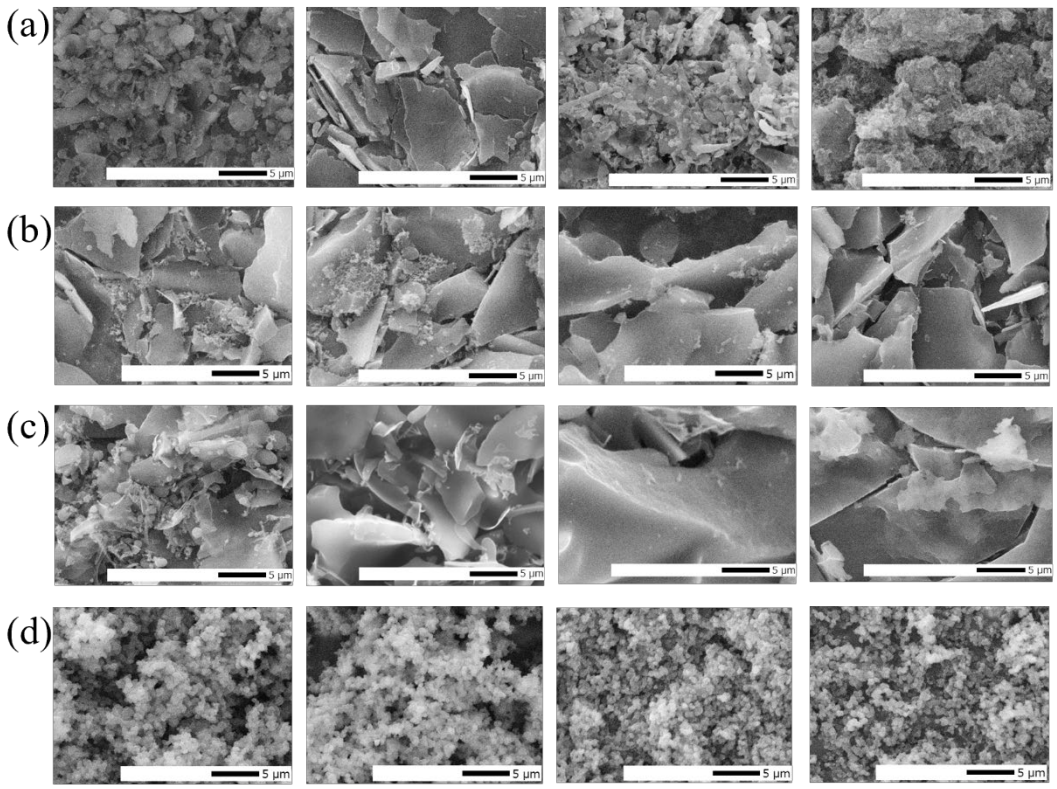

Figure 2-2. SEM images (×5000) of PPy synthesized using (a) Py concentrations of 0.01 M, 0.04 M, 0.10 M, and 0.30 M at 0.10 M SDS and APS/Py = 1.00 (Left to Right), (b) SDS concentrations of 0.01 M, 0.04 M, 0.10 M, and 0.30 M at 0.04 M Py and APS/Py = 1.00, (c) APS/Py ratios of 0.27, 0.68, 1.50, and 3.50 at 0.10 M SDS and 0.04 M Py, and (d) Py concentrations of 0.01 M, 0.04 M, 0.10 M, and 0.30 M with no SDS and APS/Py = 1.00.

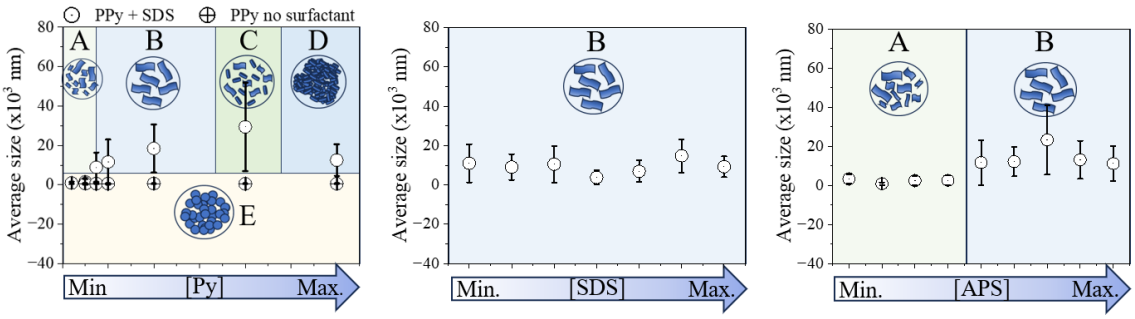

Scheme 2-3. Diagrams showing PPy morphologies for different Py, SDS, and APS concentrations: A = random form, B = sheet-like form, C = flake-like form, D = irregular form, and E = sphere-like form.

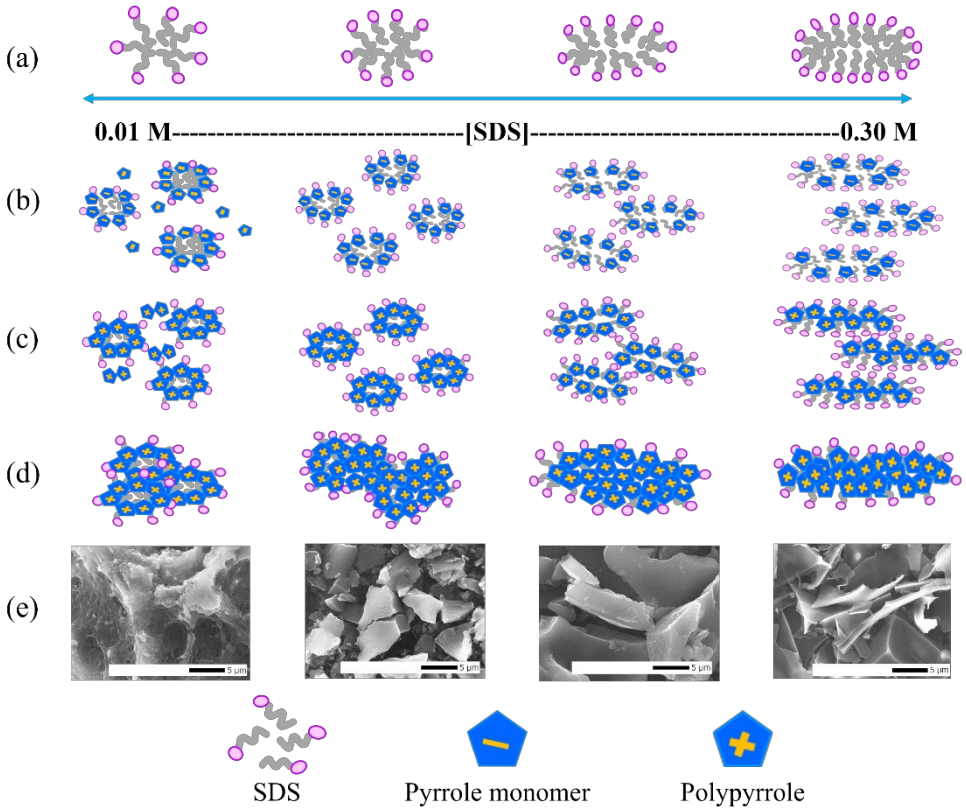

Scheme 2-4. Diagrams proposing mechanisms for PPy formations synthesized in the solutions with (a) SDS, (b) Py and SDS, (c) Py, SDS, and APS, and (d) PPy with APS/Py ratio of 1.00 after 24 hours; SEM images showing PPy samples at ×5000 magnification (freeze-dried powder).

3.2. UV-Vis-NIR absorbance and optical band gap determination

The light absorbance of PPy samples was analysed using UV-Vis-NIR spectroscopy, and the optical band gap of the samples was determined. The absorption spectra of PPy were monitored in 200 – 1000 nm wavelength window. Two absorption peaks were observed: one between 428 nm and 475 nm and the other between 835 nm and 930 nm (**Figures 2-3a–2-3c**). The first peak (428 – 475 nm) corresponds to a π-π* transition, suggesting the presence of neutral and polarons in PPy. The second peak (820 – 930 nm) corresponds to the oxidized bipolarons of the PPy chain.(Brédas et al., 1984; Kausaite-Minkstimiene et al., 2015).

In **Figure 2-3a**, the PPy obtained using 0.01 M and 0.03 M Py shows negligible absorbance at the neutral polarons and oxidative bipolarons spots but shows peaks at

wavelengths of 297 nm and 284 nm. These peaks can be ascribed to the SDS signals (**Figure 2-4**), indicating the SDS incorporation into PPy samples. The PPy samples synthesized at a 0.04 M Py showed light absorption peaks at 448 nm and 841 nm, which correlated to polarons and bipolarons, respectively. When the Py concentration increased from 0.04 M to 0.30 M, the two light absorption peaks shifted from 448 nm to 475 nm and from 841 nm to a longer wavelength (outside the measurement range). The shifts indicated a higher degree of Py oxidation at high Py concentrations (Bayat et al., 2021; Yun et al., 2012), suggesting that a larger-sized PPy was produced for a more concentrated Py solution (**Figure 2-1a**). The increased oxidation degree was also associated with PPy shape transformation from a combination of particles and sheet-like structures to sheet-like structures and irregular shape (0.30 M Py) (**Figure 2-2a**). These can be attributed to a limited number of SDS micelles at elevated Py concentrations, which lowers their effectiveness in facilitating the growth of PPy sheets.

When the SDS concentration was varied while maintaining the Py concentration at 0.04 M, the absorbance peaks of PPy remained more stable than they were during the variation of Py concentration. An increase in SDS concentration from 0.01 M to 0.30 M caused a negligible change in the position of the neutral polarons peak at 447 nm, and a slight shift in the bipolarons peak from 827 nm to 844 nm as shown in **Figure 2-3b**. The results support that SDS has a dual function: (i) as a surfactant in polymerization and (ii) as counter ions of PPy. The shift in bipolarons peak can be attributed to the partial doping of PPy with SDS. When the APS/Py ratio increased from 0.14 to 0.27, the absorbance peaks of the polarons and bipolarons shifted from 428 nm to 431 nm and from 840 nm to 835 nm, respectively. As the ratio increased to 0.68, 1.00, and 1.50, the neutral polarons peak shifted from 438 nm to 442 nm and 448 nm, whereas the oxidative bipolarons peak shifted from 840 nm to 842 nm and 894 nm. As the APS/Py ratio increased from 1.50 to 2.00, the bipolarons peak shifted from 894 nm to 843 nm while the polarons peak remained at 448 nm. At an APS/Py ratio of 3.50, the bipolarons peak disappeared completely. An increase in the APS/Py ratio provides Py with more oxidizing agents, enhancing the growth and oxidative level of PPy. On the other hand, a high APS content can over-oxidize PPy, preventing it from growing further (Paúrová et al., 2020; Vigmond et al., 1995). Thus, the sheet-like structures were formed even at a relatively high APS/Py ratio.

The optical band gap of PPy samples was determined based on the light absorption data from the UV-Vis-NIR and Tauc's correlation (**Figures 2-3d–f** and **Figure 2-5**). The band gap of PPy continued to decrease as the Py concentration increased at a constant SDS concentration and APS/Py ratio. When the concentration of Py rose from 0.01 M to 0.20 M, the optical band gap dropped from 2.63 eV to 2.38 eV. A significant decrease in the band gap to 1.10 eV occurred when the Py concentration reached 0.30 M (**Figure 2-3d**). A reduction in the band gap implies that the energy served for an electron to travel from the valence band to the conductive band is reduced, indicating that the PPy synthesized at a high Py concentration has a high electrical conductivity. These results agree well with the results from the SEM analysis, which shows that morphology changes from particles to sheets and irregular structures correspond to the increase in the Py concentration. The degree of oxidation of PPy was enhanced for increased surface area. An increase in SDS concentration from 0.01 M to 0.30 M, at the constant Py concentration and APS/Py ratio, caused a slight reduction in the PPy band gap, reducing from 2.96 eV to 2.78 eV (**Figure 2-3e**) (Hazarika & Kumar, 2013). The variation of the SDS concentration during the synthesis of PPy did not result in a significant difference in the band gap.

Throughout the alteration of the APS/Py ratio, with constant SDS and Py concentrations, the ratio increments from 0.10 to 0.27 yielded negligible alterations in the optical band gap, ranging from 3.21 eV to 3.03 eV. As the ratio increased from 0.68 to 3.50, the band gap of PPy decreased from 2.52 eV to 1.74 eV (**Figure 2-3f**). It is worth noting that as the APS/Py ratio varied from 0.01 to 3.50, the PPy shape transformed from particles to a sheet-like structure, which can contribute to the band gap reduction of PPy.

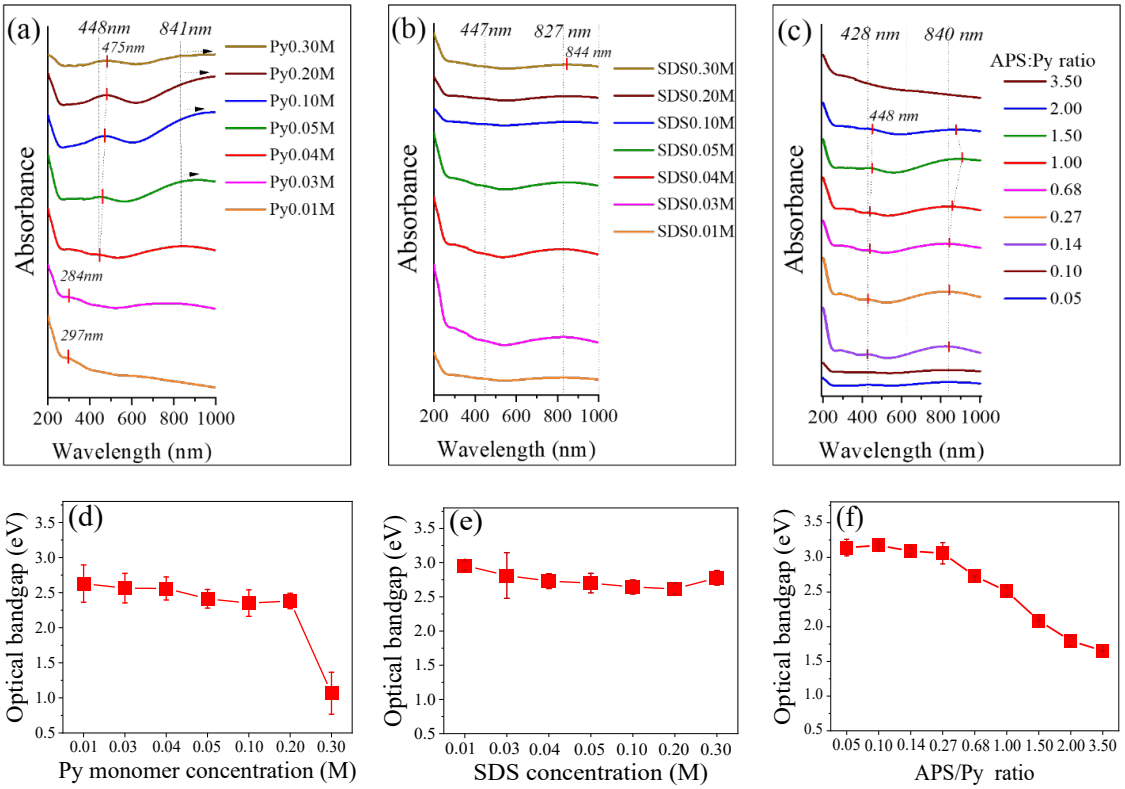

Figure 2-3. Light absorbances of PPy samples synthesized from a solution with (a) varied Py concentrations (0.10 M SDS and APS/Py = 1.00), (b) varied SDS concentrations (0.04 M Py and APS/Py = 1.00) and (c) varied APS/Py ratio (0.10 M SDS, 0.04 M Py); The optical band gap of PPy changing with (d) increased Py concentration, (e) increased SDS concentration, and (f) increased APS/Py ratio.

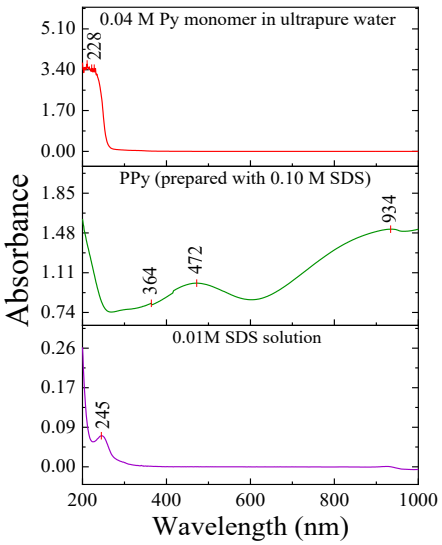

Figure 2-4. Absorbance from UV-Vis NIR spectroscopy.

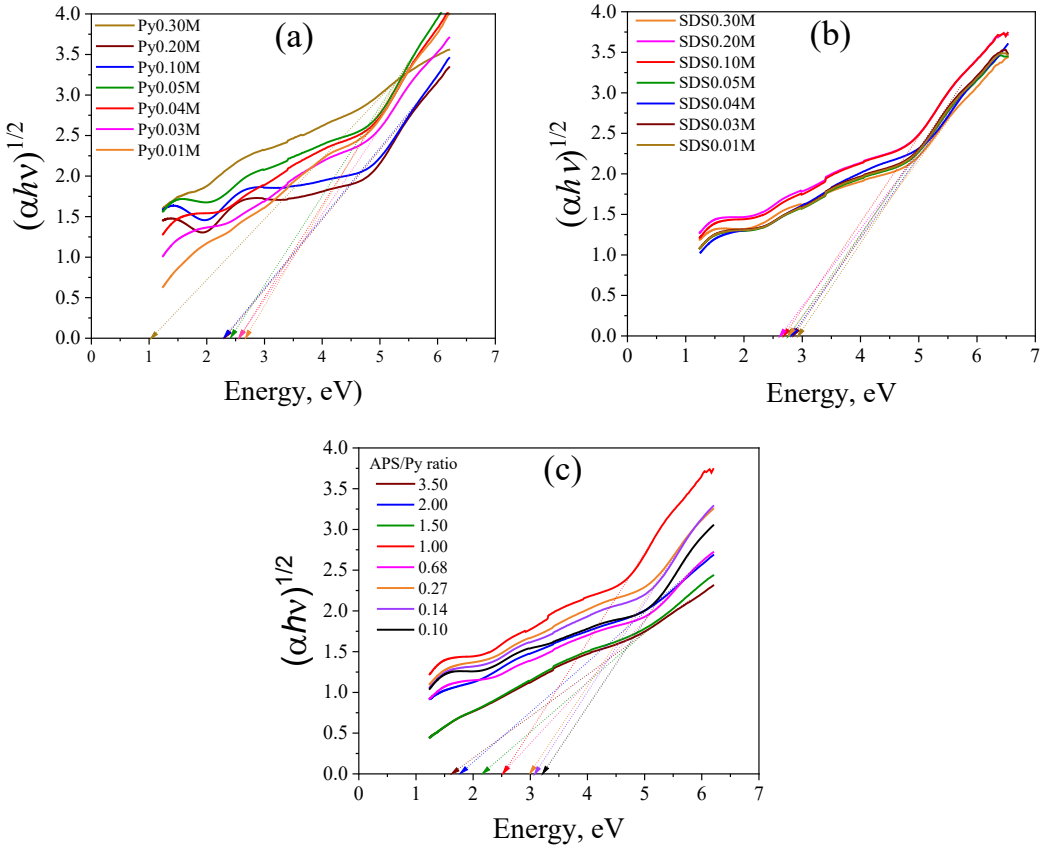

Figure 2-5. Tauc plots of the PPy samples. Variation of (a) Py monomer concentration, (b) SDS concentration, and (c) APS/Py ratio.

3.3. Electrical conductivity of PPy films

PPy and PPy* samples were fabricated to a chemiresistive device (**Scheme 2-2**), in which the polymer film was sandwiched by the ITO electrodes and the electrical conductivity was monitored. The device was analysed in a LSV mode at a scan range of ±1.80 V and a scan rate of 50 mV/s to obtain the resistance and conductivity, respectively. The resistance of PPy sample device decreased from 0.73 GΩ to 43.58 Ω for the PPy from Py concentration of 0.03 M and 0.30 M (**Figure 2-6a**). The resistance of the PPy* device reduced from 28.04 kΩ to 397.70 Ω for the PPy* synthesized from 0.03 M and 0.30 M Py with no SDS. These results support my finding that utilization of SDS, with proper amounts of Py and APS, in the chemical polymerization of PPy can effectively enhance PPy conductivity (Paúrová et al., 2020; Scott et al., 1984). The resistance of PPy decreased from 1.50 GΩ to 5.29 MΩ when the SDS concentration increased from 0.01 M

to 0.20 M (**Figure 2-6b**). In this study, the author observed a substantial alteration in the PPy resistance when SDS concentration was at or below 0.04 M, which is close to the CMC value (0.008 M to 0.0083 M) (Qin & Qiu, 2019; Roohi et al., 2022). When the SDS content was low, PPy acquired irregular shapes (correlating to high PdI, 0.39), yielding poor adhesion and electrical contacts between each PPy particle. The phenomenon led to a high resistance for the PPy chemiresistive device (Zhang et al., 2006). When the APS/Py ratio increased from 0.14 to 2.00 (constant SDS and Py concentration), device resistance decreased from 50.19 MΩ to 80.32 kΩ (**Figure 2-6c**). The association between the resistance of PPy and its band gap is depicted in **Figures 2-3d–f**, stating that a decline in the band gap leads to a reduction in resistance. As the APS/Py ratio increased from 0.68 to 2.00, the resistance of PPy decreased from 15.00 MΩ to 80.32 kΩ and the band gap decreased from 2.52 eV to 1.80 eV, and the morphology was presented in sheet-like form.

The reduction in resistance and band gap partly corresponds to the morphology change from a random to a sheet-like form. The results are summarized in **Figure 2-7a**, showing that the band gap of PPy is in the range of 3.16 eV to 1.46 eV and that PPy changed from an undoped state to an oxidized and fully doped state (Brédas et al., 1984; Iurchenkova et al., 2021; Scott et al., 1984). **Figure 2-7a** displays this as the size of the PPy particles increased from 50 nm to 600 nm and the band gap decreased. This observation is consistent with the behaviour observed in silicon or gallium phosphide or indium arsenide. The author observed that the band gap of PPy tended to cluster at approximately 2.5 eV, which agrees well with the results obtained in a previous study. The PPy band gap obtained using UV-Vis-NIR revealed that the polymerization oxidized PPy but could not fully transform it into a doped state except at a Py concentration of 0.30 M. This limitation resulted in a band gap of 1.10 eV, and an average particle size of 604.50 nm.

The electrical resistances of PPy samples are summarized in **Figure 2-7b**, showing the resistances in the reference range of 2.46×10^{-3} Ω to 2.46×10^{7} Ω (Singh, 2017). The resistance was calculated from resistivity using equations (2) and (3). **Figure 2-7b** shows that the resistance of PPy decreases as its particle size increases, which is consistent with **Figure 2-7a**. At low Py concentrations of 0.01 M and 0.03 M, SDS concentrations of 0.01 M, 0.03 M, 0.04 M, and 0.30 M, and low APS/Py ratios of 0.10, 0.14, and 0.27, the resistance was higher than that of the reference range. This can be addressed since PPy provided smaller size particles, sheets or flake structures in those

synthesis conditions and the electrical resistance was monitored from the chemiresistive device. The resistance obtained from the device was a combination of intrinsic and extrinsic resistances (Nah et al., 2022), where the former and the latter were correlated to PPy conductivity and contacts between PPy samples, respectively. In the case of smaller PPy particles, a high number of contacts occurred, leading to domination of contact resistance instead of material resistance. This assumption also explained high electrical resistance in the case of an irregular-shape PPy, which followed the extrinsic resistance-dominating model. At a high SDS concentration of 0.30 M, PPy has a sheet-like structure with a high resistance of 67.00 MΩ, indicating that a too high SDS concentration can disturb the conductivity of PPy.

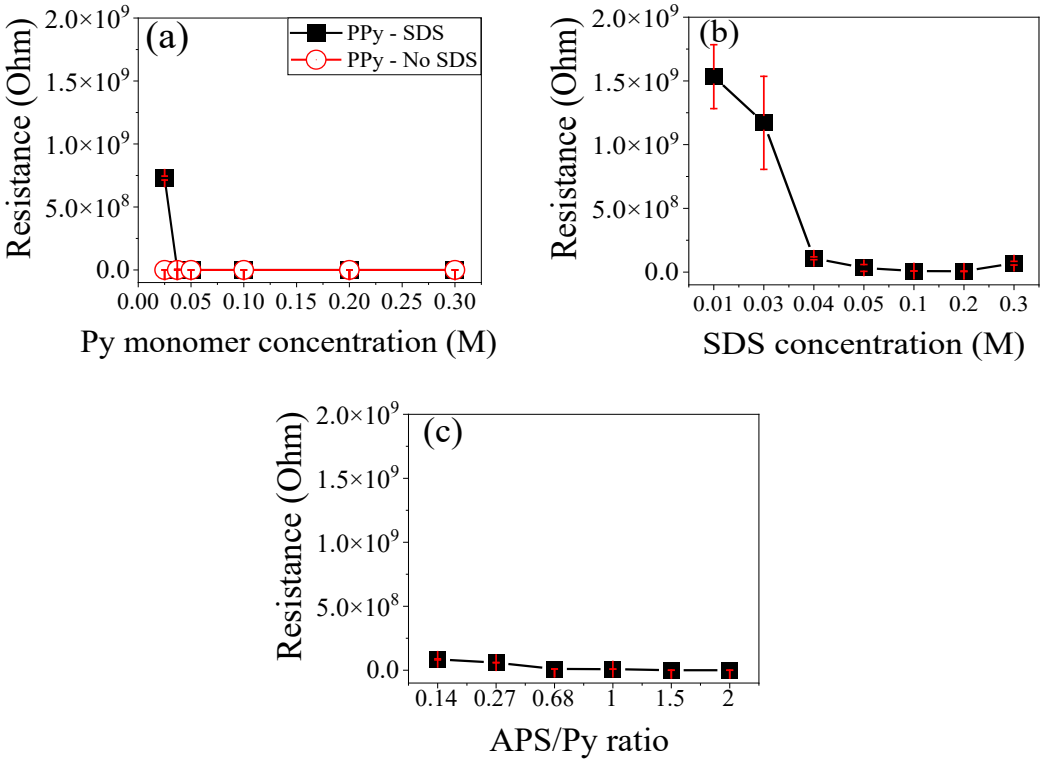

Figure 2-6. Resistance of PPy polymerized by varying (a) Py concentration (0.10 M SDS and APS/Py = 1.00), (b) SDS concentration (0.04 M Py and APS/Py = 1.00), and (c) APS/Py ratio (0.10 M SDS and 0.04 M Py).

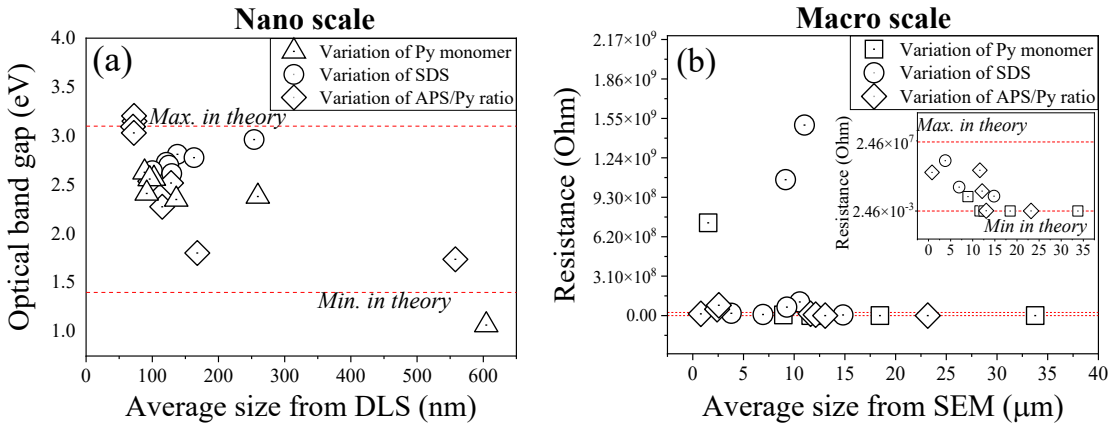

Figure 2-7. Relationship between the (a) optical band gap and average particle size of PPy and (b) resistance and average particle size of PPy as observed from SEM images.

3.4. Bipolarons and polarons structures and electronic properties

Raman spectroscopy was used to analyse the chemical functionalities of PPy. The PPy sample was excited at 532 nm, yielding signals for polarons and bipolarons (**Table 2-1**). The Raman spectra shown in **Figure 2-8a-c** indicated similarities in peaks, including C–C ring deformation for bipolarons (926 – 927 cm^{-1}) and polarons (963 – 985 cm^{-1}), C–H deformation for polarons (1050 – 1056 cm^{-1}) and bipolarons (1079 – 1084 cm^{-1}), and C–C ring stretching for the polarons (1330 – 1344 cm^{-1}) and bipolarons (1377 – 1382 cm^{-1}). The C=C stretching peak appeared at 1562 – 1593 cm^{-1} for the polarons but was not detected at 1600 cm^{-1} and 1618 cm^{-1} for the bipolarons.

In **Figure 2-8a**, when the concentration of Py rose from 0.01 M to 0.30 M while the SDS concentration and APS/Py ratio remained unchanged, the polarons peak corresponding to C–C ring deformation shifted from 986 cm^{-1} to 976 cm^{-1}. The C–C ring deformation of the bipolarons (926 – 927 cm^{-1}) remained almost unchanged. The polarons peak that shifted to the left supported a highly oxidized chain of PPy.(Ishpal & Kaur, 2013) As the Py concentration increased, the C–H deformation peak associated with the polarons shifted from 1050 cm^{-1} to 1060 cm^{-1}. This shift indicated an increase in the oxidative degree of PPy (Ishpal & Kaur, 2013). Additionally, with increased Py concentration, a C–H deformation peak of the bipolarons emerged and was enhanced at 1083 cm^{-1}. The C–C ring stretching remained constant for the polarons (1340 – 1342 cm^{-1})

and moved to the left (from 1387 cm^{-1} to 1379 cm^{-1}) in the case of the bipolarons. The peak shift from 1415 cm^{-1} to 1410 cm^{-1} can be attributed to the C–C and C–N stretching of oxidized PPy in the ring structure. This shift was observed as the Py concentration increased from 0.01 M to 0.05 M and was difficult to follow at Py concentrations exceeding 0.05 M. The shift toward a lower frequency range indicates the transition of PPy to a neutral state during its C–N stretching (Trchová & Stejskal, 2018). The C=C stretching peak of the polarons shifted from 1599 cm^{-1} to 1579 cm^{-1} as the Py concentration increased from 0.01 M to 0.30 M. The shift toward a smaller wavenumber indicated switching from an oxidative to a neutral state, while a narrow and sharp C–C peak corresponded to a high degree of crystallinity (Jeeju et al., 2012).

As the SDS concentration varied from 0.01 M to 0.30 M during PPy synthesis (constant Py concentration and APS/Py ratio), the C–C peak did not shift (**Figure 2-8b**). The C–C ring deformation of bipolarons (939 cm^{-1}) and polarons (979 cm^{-1}) moved to the left and right, respectively. The C–H deformation showed a similar trend, in which the C–H deformation of bipolarons shifted left (1052 cm^{-1}) and polarons shifted right (1086 cm^{-1}). The C–C ring stretching peak for polarons was at 1338 cm^{-1}, while the C–C and C–N stretching peaks for bipolarons were at 1377 cm^{-1} and 1417 cm^{-1}, respectively. The SDS concentration did not significantly affect the degree of PPy oxidation, but the presence of SDS promoted PPy oxidation.

An increase in the APS/Py ratio from 0.10 to 3.50 did not shift the C–C ring deformation peak for polarons but provided a slight shift in the C–C ring deformation for bipolarons (946 – 943 cm^{-1}) (**Figure 2-8c**). The C–H deformation peaks remained unchanged while the APS/Py ratio varied, revealing peaks of polarons and bipolarons at 1055 cm^{-1} and 1081 cm^{-1}, respectively. The C–C ring stretching peaks of the polarons and bipolarons remained insensitive to changes in the APS/Py ratio and were present at 1338 cm^{-1} and 1377 cm^{-1}. The C–C and C–N stretching peaks of the ring structure appeared at 1411 cm^{-1} unchanged as the ratio changed. The C=C stretching peaks of the polarons appeared at 1596 cm^{-1} when the APS/Py ratio was 3.50 and shifted to the left when the ratio increased from 0.10 to 2.00.

3.5. Relationship of its properties

The bipolarons/polarons ratio, indicative of the oxidative state of PPy, was calculated by dividing the peak intensity of bipolarons by that of polarons. The analysis focused on the C–C ring deformation, C–H deformation, and C–C ring stretching vibration. The resulting bipolaron/polaron ratios are presented in **Figure 2-8d-f**. Additionally, the author analysed PPy samples synthesized with SDS compared to SDS solution (0.01 M) as shown in **Figure 2-9a**. SDS solution analysis revealed a small peak at 1061 cm^{-1}, representing C–C stretching of SDS, which the intensity was too low compared to the peak intensity found in the PPy samples. Furthermore, the prominent peak found in SDS solutions was the peak intensity at approximately 2850 cm^{-1} and 2890 cm^{-1}, which consistent with the asymmetric and symmetric vibrations of the ($–CH_2–$) group, respectively. Therefore, the authors assumed that the C–H structure of SDS did not impact the peak intensity of C–H deformation in PPy samples within the range of polarons (1050 – 1056 cm^{-1}) or bipolarons (1079 – 1084 cm^{-1}).

For analysis in C–C ring deformation region (**Figure 2-8d**), the bipolarons/polarons ratio increased from 1.08 to 0.96 as the Py concentration increased from 0.03 M to 0.30 M. The corresponding ratio for PPy* remained almost unchanged (1.01 to 1.05) as the Py concentration increased (the original Raman spectra is shown in **Figure 2-9b**). The bipolarons/polarons ratio with respect to the C–H deformation of PPy increased from 0.76 to 0.94 as the Py concentration increased. The corresponding ratio of PPy* fluctuated between 0.55 and 0.70 irrespective of the Py concentration (0.03 M to 0.30 M). SDS promoted the C–H deformation in PPy and affected its physical morphology (**Figures 2-2a–c**). The bipolarons/polarons ratio of PPy correlated with its C–C ring stretching, which grew from 0.93 to 1.03 as the Py concentration increased from 0.03 M to 0.30 M. The corresponding ratio of PPy* remained almost constant within the range of 0.88 – 0.93. The increased bipolaron/polaron ratio related to the C–C ring stretch ing of PPy resulted in the reduction of its band gap from 2.63 eV to 1.07 eV. As the Py concentration increased from 0.10 M to 0.30 M, the bipolarons/polarons ratio of the C–C ring stretching in PPy increased and triggered a decrease in the resistance of PPy (**Figure 2-6**) and its band gap (**Figure 2-3**). These results suggest that the increased bipolarons/polarons ratio of C–C

ring stretching in PPy enhanced its conductivity. These results showed that using SDS can modify the oxidative state of PPy.

Additionally, the comparison between morphology and bipolarons/polarons ratio showed an alignment with the transformation of the PPy structure. The morphology of PPy transformed from a random form to a sheet-like structure (**Figure 2-2a**) when the Py concentration rose from 0.10 M to 0.30 M while using 0.10 M SDS, but the shape of PPy* has a sphere-like form (**Figure 2-2d**). From the bipolarons/polarons ratio of PPy and PPy*, the author found that the value in the bipolarons/polarons ratio of C–H deformation of PPy is larger than that of PPy* as the Py concentration increased, as mentioned above. It is possible that SDS functions as a dopant and interferes with the formation of the PPy structure during Py polymerization (Appel et al., 1999; Bayat et al., 2021), as represented in the C–H deformation of the Raman spectra. The change in C–H deformation affects the gap energy, as shown in the relational tendency with the band gap. That is, the bipolarons/polarons ratio in the C–H deformation of PPy increased from 0.80 to 0.94, resulting in a reduction of its band gap from 2.63 eV to 1.00 eV (**Figure 2-3d**) and its resistance from 0.73 GΩ to 43.60 Ω (**Figure 2-6a**) when the concentration of Py increased from 0.10 M to 0.30 M while using 0.10 M SDS.

In the varied SDS concentration experiment at a constant Py of 0.04 M and APS/Py ratio of 1.00, no significant change in the bipolarons/polarons ratio (**Figure 2-8e**), was observed since the C–C deformation varied from 1.08 to 0.89, the C–H deformation from 0.72 to 0.81 and the C–C ring stretching from 0.94 to 0.97. When considering these results together with the analysis from size (ranging from 100.10 nm to 253.90 nm), band gap (2.62 eV to 2.96 eV), and shape (a sheet-like), these findings indicated that not much of the electrical and chemical properties of the PPy altered at various SDS concentrations and that the extrinsic property, contact resistance, was the key to resistance change.

As **Figure 2-8f** shows, the bipolarons/polarons ratio of C–C ring deformation first increased from 0.90 to 1.15 and decreased to 0.98 when the APS/Py ratio increased while the Py and SDS concentrations remained constant. The C–H deformation first increased from 0.69 to 0.86 and then decreased to 0.71 as the APS/Py ratio increased. During C–C ring stretching, the bipolarons/polarons ratio first changed slightly from 0.93 to 0.98 and

then decreased to 0.92 when the APS/Py increased. These trends correspond to the change in the bipolarons state observed using UV-Vis-NIR spectroscopy and align with the transformation of the PPy structure from an irregular to a sheet-like structure (**Scheme 2-3c**), particularly the ratio in C–C ring deformation and in C–H deformation. The increase in the bipolarons/polarons ratio is associated with band gap reduction (drop from 3.21 eV to 1.74 eV), indicating an enhanced degree of oxidation for PPy as the APS/Py ratio increased. Although the bipolarons/polarons ratio dropped when the APS/Py ratio increased, those ratios showed a low energy gap and low resistance. It was assumed that the sheet-like structure, which occurred in cooperation with SDS, might be a factor that helps to maintain the band gap properties of PPy compared to no surfactant.

The results of varying the Py concentrations, SDS concentration and APS/Py during the synthesis of PPy demonstrate that different concentrations of the components lead to distinct oxidative states of PPy, as observed from the shift in the UV-Vis-NIR absorbance peaks and the appearance of bipolarons and polarons structures in the Raman spectra. Specifically, an increase in the Py concentration and APS/Py ratio resulted in high oxidative states in PPy. The increase in the average size of PPy correlated with a reduction in its optical band gap, possibly because of the enhancement of its conductivity resulting from its large surface area. This correlation was confirmed by the decrease in the resistance of PPy and transformation of its morphology from a combination of particles and sheet-like structures to purely sheet-like structures with increasing Py concentrations (**Scheme 2-3**). At Py concentrations in the range from 0.10 M to 0.30 M, the bipolaron/polaron ratio of C–C ring stretching and C–H deformation was observed to shift toward a bipolaron state in PPy, whereas the ratio remained unchanged in PPy*. These results suggest that combining SDS with an appropriate amount of Py would effectively promote the conductivity of PPy. Additionally, SDS promoted the bipolaron/polaron ratio of C–H deformation and affected the physical morphology of PPy. The observed variations in the morphology and size of PPy could be partly attributed to the different C–H bond structures formed when an SDS template was used during the polymerization process.

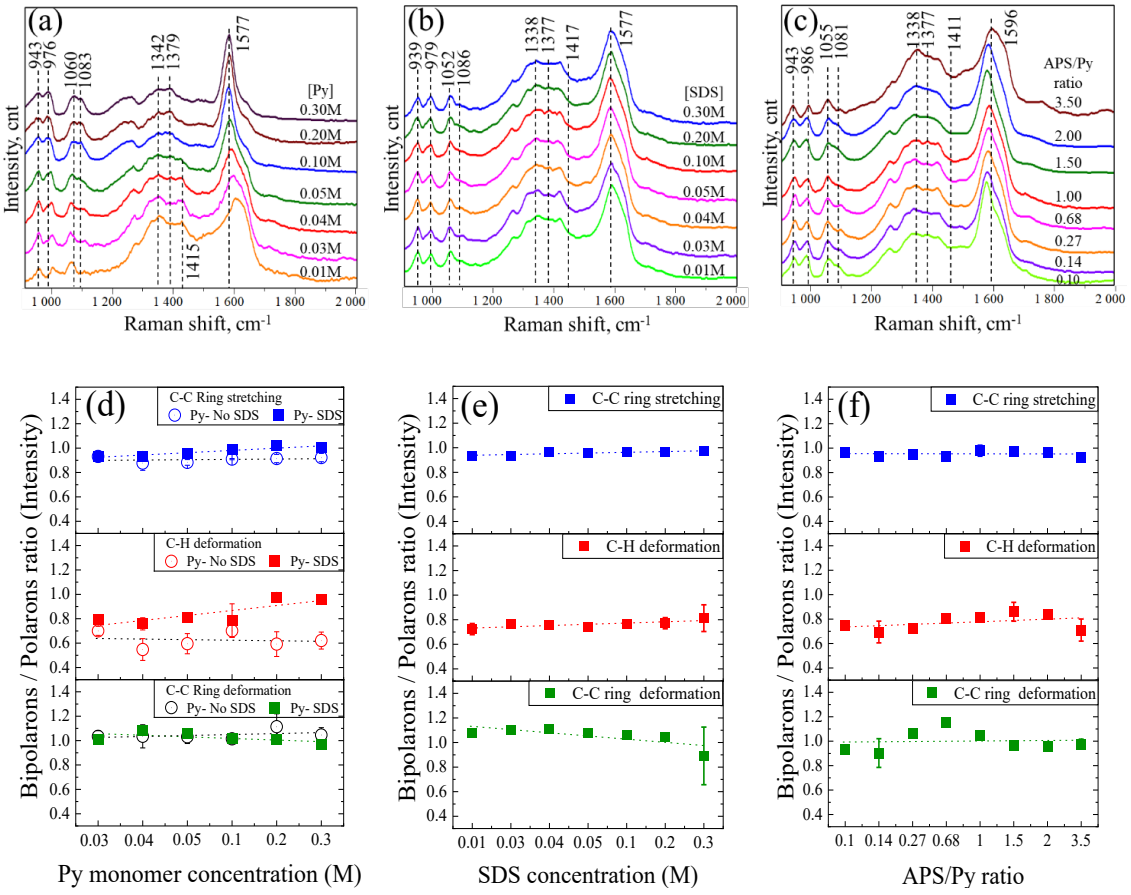

Figure 2-8. Raman spectra of the PPy synthesized by varying the (a) Py concentration, (b) SDS concentration, and (c) APS/Py ratio. The bipolaron to polaron ratio of the PPy synthesized by varying the (d) Py concentration (at 0.10 M SDS and an APS/Py = 1.00), (e) SDS concentration (at 0.04 M Py and an APS/Py = 1.00), and (f) APS/Py ratio (at 0.10 M SDS and 0.04 M Py).

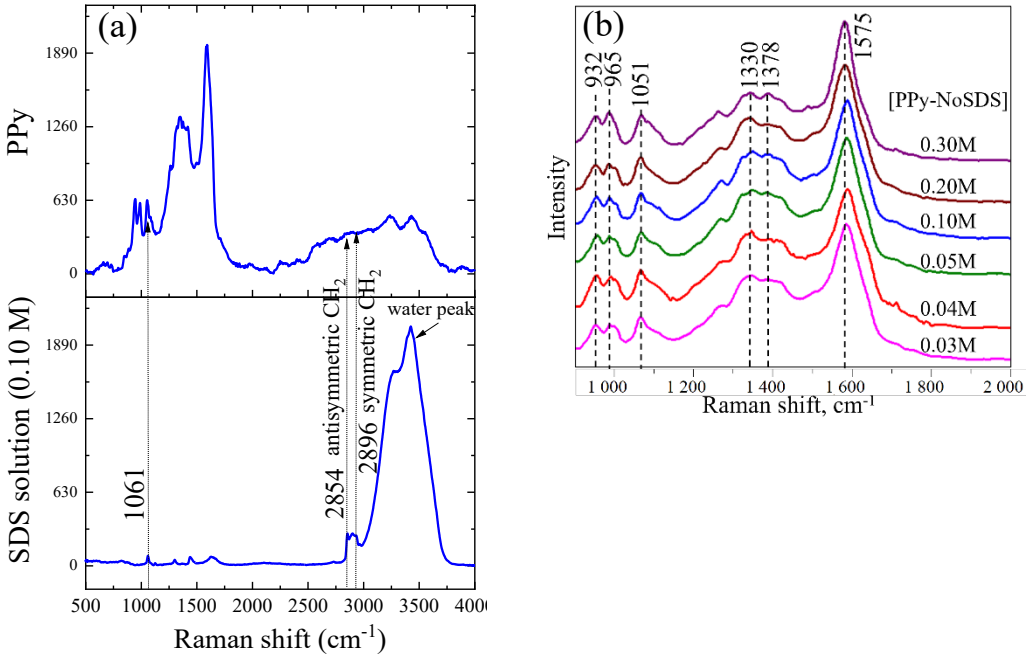

Figure 2-9. Raman spectra of PPy samples: (a) PPy prepared with 0.04 M Py and 0.01 M SDS and SDS solution with marks for CH_2 group and (b) PPy synthesized with no SDS.

4. Summary

This work aims to investigate the effects of SDS on the chemical polymerization of PPy and explore the relationship between its properties. It was found that SDS functioned as a template for Py polymerization and influenced the physical, electrical, and chemical properties of PPy. Py were polymerized within the micellar structure of an SDS template. Their morphologies transformed from random forms to sheet-like forms and enlarged the size structure when Py concentration and APS/Py ratio increased using 0.01 M SDS. On the contrary to PPy* (PPy synthesized in the absence of SDS), only a sphere-like form was found. SDS assists PPy in the enhancement of electrical properties. Optical band gap and conductivity increased when Py concentration and APS/Py ratio increased as compared to PPy*. The Raman spectra showed that SDS promoted a chemical change in PPy, as shown in the ratio between bipolarons and polarons, particularly in C–C ring stretching and C–H deformation. It was found that the ratio increased as the Py concentration and the APS/Py ratio increased, but the corresponding ratio for PPy* remained almost unchanged as the Py concentration increased. However, SDS concentrations ranging from 0.01 M to 0.30 M had no significant effect on the optical

band gap or average size of the PPy sheets while using 0.04 M Py and an APS/Py ratio of 1.00. This work revealed a relationship between average size, morphology, and electrical characteristics. The increase in average size was related to a decrease in band gap and resistance. The ratio of C–H deformation in PPy was larger than in PPy* indicating that SDS increased C–H deformation in PPy, which changed its physical shape and then influenced its electrical characteristics via the relationship between size and band gap, or resistance.

Consequently, SDS was crucial in changing the shape of PPy, enhancing conductivity, and changing the ratio of bipolarons to polarons in PPy. The proportion of each material (Py monomer, SDS, and APS) was also critical in defining its characteristics. This study highlights the relationship between the bipolarons/polarons ratio of PPy relating to its chemical, electronic, and morphology, providing a deeper understanding of their characteristics that can be utilized to design materials with specific properties.

Chapter 3

Exploring the Influence of Morphology on Bipolaron–Polaron Ratios and Conductivity in Polypyrrole in the Presence of Surfactants

1. Introduction

In recent times, conductive polymers, specifically polypyrrole (PPy), have garnered significant interest in academic and industry research communities globally due to their distinctive characteristics and promise for diverse commercial applications. The increased interest in PPy originates mostly from its remarkable thermal and environmental durability, impressive electrical conductivity, and simple synthesis procedure (Veisi et al., 2023; Wen et al., 2017; Xing & Zhao, 2007). These polymers are conductive because they have a conjugated electron system composed of alternating single and double bonds within their chemical structure (Kausaite-Minkstimiene et al., 2015). The unique chemical structure of conductive polymers not only allows them to conduct electricity but also piques the interest of researchers in other fields, leading to breakthroughs in conductive polymers and applications such as biomaterials (George et al., 2005; Lin et al., 2018), biosensors , and energy storage .

The electrical properties of PPy were also modified based on the polymerization process. The chemical polymerization technique is a standard method for producing PPy particles. This method required oxidizing agents, such as ammonium persulfate (APS) or ferric chloride ($FeCl_3$), to oxidize the pyrrole monomer (Py), which initiated the polymerization process. It is theorized that during the first phase of pyrrole oxidation, insoluble pyrrole oligomers form, and then PPy chains arise from clustered aggregates, culminating in globular forms. The morphology of PPy also was found to alter from globular structures to another form using templates, such as hard templates and soft templates. When utilizing a hard template, the final product's morphology is significantly influenced by the pre-prepared material, such as anodic alumina membrane producing nanowire morphology of PPy (Deljoo Kojabad & Shojaosadati, 2016), silicon wafer (Shen et al., 2023), or polymer (Parayangattil Jyothibasu & Lee, 2020). Following the reaction, the template is then carefully removed. The utilization of soft templates in

polymerization has several notable benefits, particularly regarding the flexibility and ease it provides to the polymer structure. Soft templates, typically composed of organic compounds or biological entities, allow for a more controlled and flexible synthesis process (Rahman Poolakkandy & Mol Menamparambath, 2020). The inherent flexibility of soft templates accommodates a broader range of polymer sizes and shapes, catering to specific application needs, such as surfactants like fatty alcohol polyoxyethylene ether surfactants (Z. Zhou et al., 2019), sodium dodecyl benzene sulfonate (SDBS) (J. Wang et al., 2023), or sodium dodecyl sulfate (SDS) (Jamdegni & Kaur, 2020; Samwang et al., 2023). Additionally, these surfactants, when utilized as soft templates in polymer synthesis, provide a unique and efficient method for creating polymers with the appropriate structural and functional features. In solution, these amphiphilic compounds spontaneously form micelles or other self-assembled structures, producing nanoscale templates for monomers to polymerize polymers with various morphologies and sizes (Antony & Jayakannan, 2007; Dubey, 2023b; Molina et al., 2018; Zhang et al., 2006). Moreover, using an anionic surfactant, such as SDS or SDBS, can enhance the conductivity of PPy (Omastová et al., 2003; Xing & Zhao, 2007). Meanwhile, many studies reported that the non-spherical structure of PPy obtained using CTAB showed higher electrical properties than the spherical shape (Ren et al., 2023). Additionally, Khadem et al. reported that using CTAB to prepare PPy could give it a string-bead shape with better conductivity than a spherical shape made from SDS in the same conditions (Khadem et al., 2017). Yussuf et al. found PPy prepared in SDS with $FeCl_3$ as an oxidizing agent to have fibrillar morphology and show slightly higher conductivity than the other oxidizing agent, APS (Yussuf et al., 2018).

The surfactant enhances the electronic properties of PPy through a process called doping, which often involves oxidation occurring during polymerization. The oxidation level of PPy is intricately linked with the formation of polarons and bipolarons, which are localized defects causing lattice distortion within the polymer's structure (**Figure 3-1a**) (Gupta, 2008; M. Zhou et al., 2002). These defects are crucial for facilitating the mobility of charge carriers, where polarons and bipolarons correspond to low and high oxidative states, respectively (Appel et al., 1999; Brédas et al., 1984). The genesis of these polarons and bipolarons is highly dependent on the synthesis conditions and plays a significant role in the chemical and electrical properties of PPy. Research conducted by Santos et al.

(Santos et al., 2007) and Pang SK. (Pang, 2020) through Raman spectroscopy analysis on the chemical polymerization of PPy highlighted that the pyrrole rings predominantly attach at the alpha–alpha (*α*–*α*) positions, though they can also link at the beta–beta (*β*–*β*) and beta–alpha (*β*–*α*) positions (**Figure 3-1b**). This variation in binding sites influences the molecular configuration of dimers and trimers in PPy, as well as their respective oxidative states, manifested as bipolarons and polarons. Further research by Ishpal and Kaur (Ishpal & Kaur, 2013), Trchová and Stejskal (Trchová & Stejskal, 2018), Tumacder et al. (Tumacder et al., 2022), and Paúrová et al. (Paúrová et al., 2020) showed the different Raman spectral profiles of bipolarons and polarons of PPy having varying nanostructures. Building on previous research in Chapter 2, it was observed that PPy polymerized with SDS presented a sheet-like morphology and demonstrated an increased bipolaron/polaron ratio in line with Py concentration, which correlates with a decrease in the band gap. This result contrasted with PPy synthesized without SDS, which typically forms spherical structures as shown in **Figure 3-2**.

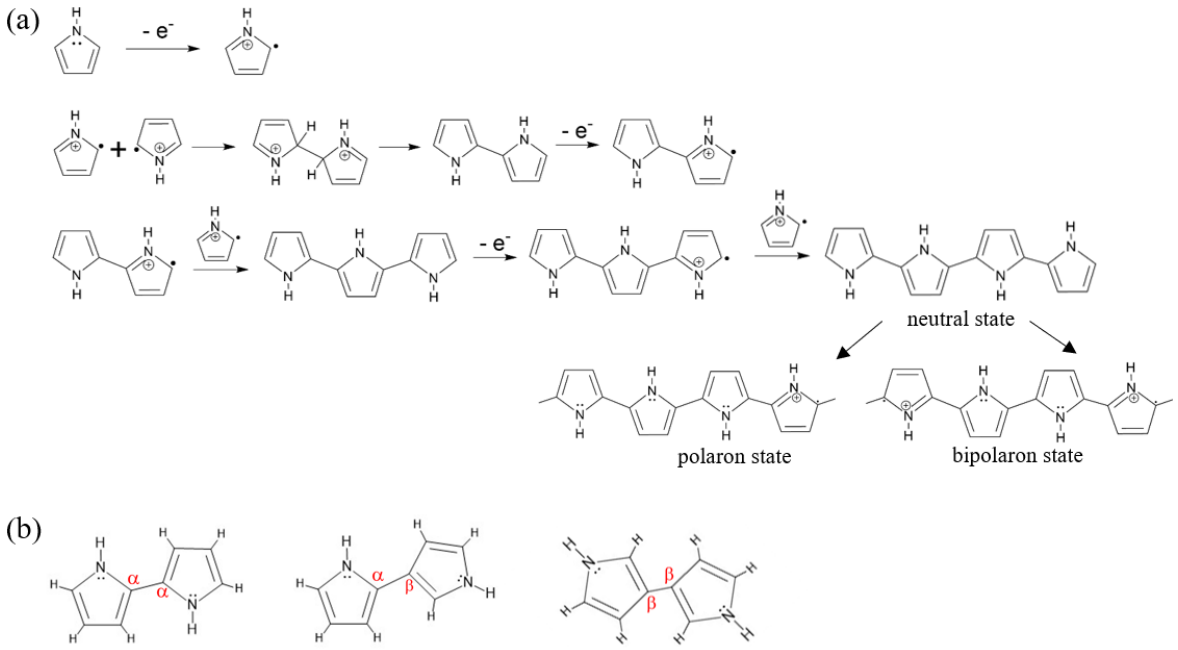

Figure 3-1. (a) Illustration of the pyrrole polymerization and (b) the molecular configuration of dimers with different interaction sites.

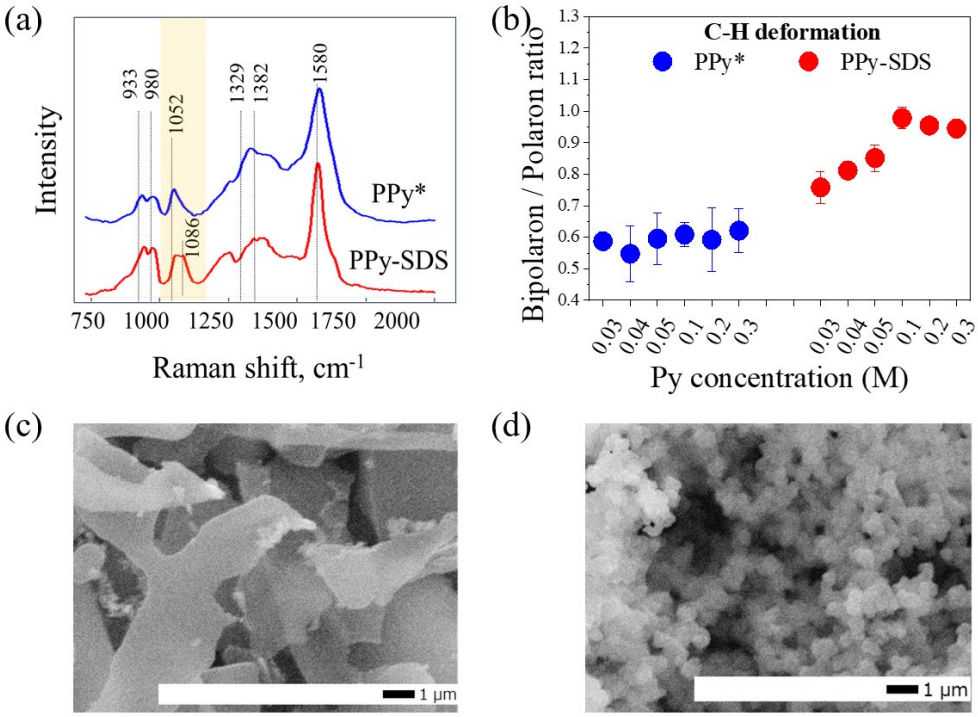

Figure 3-2. (a) Raman spectra highlight at C-H deformation region, (b) Bipolarons/Polarons ratio, comparing PPy prepared with and without using SDS, varying the Py monomer concentration, (c) SEM of PPy was prepared with SDS, and (d) PPy was prepared without SDS (reported in Chapter 2).

Therefore, this study delves into the interplay between conductivity and morphology in PPy by examining the bipolaron and polaron ratios, particularly in the C–H deformation region of the PPy structure from the Raman spectra. The author analysed the bipolaron and polaron ratio in PPy polymerized with different surfactants, including SDS, CTAB, and Tween 80 (TW). The author's hypothesis is that PPy made with CTAB and TW will have a spherical shape and a lower bipolaron/polaron ratio, especially in the C–H deformation region, compared to PPy that was treated with SDS. According to the underlying idea, a low bipolaron/polaron ratio in the C–H deformation region of spherical PPy structures might mean that they conduct electricity less well. Through this investigation, the author aims to clarify the gap reason in the relationship between the morphology and electrical properties of PPy through bipolaron and polaron ratios (**Scheme 3-1**).

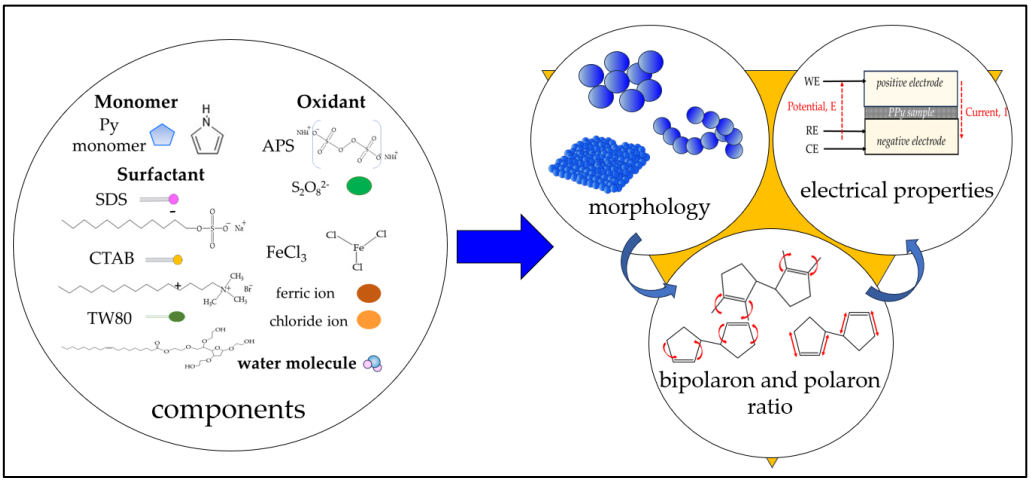

Scheme 3-1. Illustration of the relationship between PPy properties.

2. Materials and Methods

2.1. Materials

Py was used without further purification (98% reagent grade, Sigma-Aldrich Co. LLC, St. Louis, MO, USA). SDS, CTAB, TW, APS, and $FeCl_3$ were purchased from Wako Pure Chemical Industries Ltd. (Osaka, Japan). All aqueous solutions required ultrapure water with a resistance of 18.20 Mohm (MΩ) (Direct-Q 3 UV system, Merck Millipore, Osaka, Japan). Indium tin oxide (ITO) glass electrodes were purchased from BAS Inc., Tokyo, Japan. Silver paint with a resistance less than or equal to 1.00 Ω was purchased from Polycalm, a company based in Japan. A dialysis tube with a molecular weight cutoff of 14 kDa was purchased from NaRiKa Corporation, Tokyo, Japan.

2.2. Polypyrrole synthesis

PPy samples were synthesized via chemical polymerization. Py was initially introduced into a surfactant solution at a concentration of 0.10 M, which may be either SDS, CTAB, or TW. Subsequently, an oxidizing agent solution (APS or $FeCl_3$) was slowly added to the mixture during agitation to achieve a concentration of 0.10 M (the oxidizer and monomer ratio was 1.00). The mixture was agitated for 24 hours at room temperature (25 °C), resulting in the formation of a PPy suspension with a dark color. The synthesized PPy was subjected to dialysis in ultrapure water to eliminate residual impurities. The PPy sample was freeze-dried and stored in a desiccator until use.

2.3. Polypyrrole characterization

2.3.1. Particle size distribution and zeta potential measurement

PPy was suspended in ultrapure water at a concentration of 0.10 – 0.20 mg/ml, and particle size (*z*-average) and polydispersity index (PdI) were measured using a Zetasizer Nano series (ZEN5600, Malvern Instruments Ltd., Worcestershire, United Kingdom). In line with dynamic light scattering (DLS) theory, each parameter was averaged from at least three measurements, with each measurement comprising the mean of a minimum of 10 readings per sample. Zeta potential measurements were also conducted with the Zetasizer Nano series by the electrophoretic light scattering (ELS) technique. The experiment was performed at 25 °C.

2.3.2. Morphology observation by Scanning Electron Microscopy (SEM)

The dried PPy powder was obtained from the freeze dryer and stored in a desiccator until analysis. The PPy powder was affixed to an electrically grounded sample holder with double face conducting tape. The morphology of the dried PPy powder was analysed and manipulated using scanning electron microscopy (JCM-7000, JEOL Ltd., Tokyo, Japan). The pictures from SEM were evaluated on the edges and shape of particles using Image J software (ImageJ Version 1.53 K, National Institutes of Health, Maryland, USA).

2.3.3. Electrical conductivity analysis

The resistance of the PPy powder was determined using a chemiresistive device, as shown in **Scheme 3-2**. Briefly, PPy powder (0.005 – 0.008 g/cm^2) was cast into pellets using a hand press and sandwiched between two ITO glass electrodes. The distance between the electrodes and the thickness of the pellet were maintained at their initial values using 0.80 mm thick silicone rubber. The resistance of PPy was monitored and recorded based on the two-point probe measurement principle operated by an Automatic polarization system (HZ-7000, Hokuto Denko Corporation, Tokyo, Japan). Each resistance (*R*) was obtained from the slope of the Current (*I)*/Voltage (*V)* graph based on Ohm's law ($V = IR$). From the *I*/*V* plot, *R* is the reverse of slope (R = 1/slope), which is determined by Origin software (OriginPro 2023, Student version 10.0.0.154, OriginLab Corporation, Northampton, MA, USA). The conductivity of PPy was determined by the correlations shown in Equations (1) and (2) as follows:

$$\rho = \frac{RA}{L} \quad (1)$$

$$\sigma = \frac{1}{\rho} \quad (2)$$

where R is the resistance of PPy (Ω), ρ is the resistivity of PPy (Ω·m), L is the thickness of the PPy pellet (8.00×10^{-4} m), A is the area of the sample (1.96×10^{-5} m^2), and σ is the electrical conductivity (S/m).

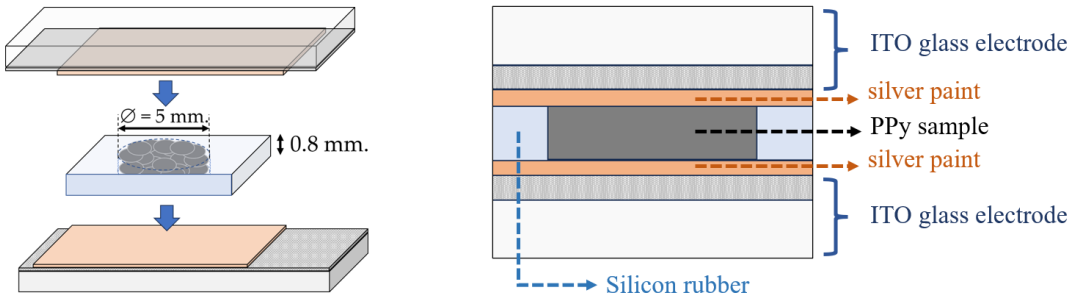

(a) (b)

Scheme 3-2. (a) Two-electrode cell construction for resistance measurement and (b) cross-sectional side view of the cell set up, illustrating the internal structure and positioning of components within the cell.

2.3.4. Raman spectra analysis

Raman spectra analysis of PPy was conducted with Raman spectroscopy (HR-800, Horiba Ltd., Kyoto, Japan) at 532 nm of laser excitation wavelength. The peak intensities of the bipolarons and polarons in PPy were evaluated using Origin software (Version 2023, OriginLab Corporation, Northampton, MA, USA). Subsequently, the ratio between the highest intensity of the bipolarons and polarons was analysed.

2.3.5. UV-Vis-NIR absorbance and band gap calculation

PPy was diluted and suspended in ultrapure water (0.10 – 0.20 mg/mL) in a quartz cuvette with a path length of 10 mm, and its optical characteristics were investigated using UV-Vis-NIR spectroscopy (UV1800, SHIMADZU, Kyoto, Japan). The optical band gap was calculated using Tauc's correlation, as indicated in Equation (3).

$$(\alpha h\nu)^{1/n} = \alpha_0(h\nu - E_g) \quad (3)$$

where α is the absorption coefficient, $h\nu$ is the photon energy (eV), h is Planck's constant (6.6261×10^{-34} J·s), and ν is the photon frequency with $\nu = C/\lambda$, where C = the speed of light (2.998×10^8 m/s), λ is the wavelength (nm), and the photon energy (eV) is $1240/\lambda$. E_g is the optical band gap (eV), α_o is the constant band-tailing parameter, and n is the power factor (n = 2 for an indirect transition band gap). The plot of $(\alpha h\nu)^{1/n}$ versus photon energy ($h\nu$) will show a straight line inside a given region. The optical band gap was calculated by extending the straight-line intercept along the ($h\nu$)-axis.

3. Results

This section presents the findings of the experiment, encompassing the physical, chemical, and electrical characteristics of the PPy samples synthesized by the chemical polymerization method. The PPy samples consisted of Py polymerized with different surfactants: SDS, CTAB, or TW. Additionally, two types of oxidizing agents, APS and $FeCl_3$, were used. The samples were labelled Py-SDS-APS, Py-CTAB-APS, Py-TW-APS, Py-SDS-Fe, and Py-CTAB-Fe compared with Py polymerization without the surfactant (PPy*), as shown in **Table 3-1**. The concentrations of each component—Py monomer, surfactants, and oxidizing agents—utilized in this experiment were constant (0.10 M), where the concentration of surfactants exceeded the critical micelle concentration (CMC), allowing them to create a micelle template in the water system.

Table 3-1. Sample abbreviations and compositions.

Sample ID	Py Concentration (M)	Surfactant	Surfactant Concentration (M)	Oxidizing Agent*
PPy*	0.10	–	–	APS
Py-SDS-APS	0.10	SDS	0.10	APS
Py-CTAB-APS	0.10	CTAB	0.10	APS
Py-TW-APS	0.10	TW	5 wt%	APS
Py-SDS-Fe	0.10	SDS	0.10	$FeCl_3$
Py-CTAB-Fe	0.10	CTAB	0.10	$FeCl_3$

* The ratio of oxidizing agent to pyrrole monomer was 1.00.

3.1. Average size and zeta potential

The average size of six PPy samples, each generated with different surfactants and oxidizing agents, is shown in **Figure 3-3a**. The results highlight the significant impact of the polymerization process on the hydrodynamic diameter (particle size), as determined by DLS technique using the zetasizer apparatus. Notably, PPy synthesized with APS as the oxidizing agent and surfactant exhibited a smaller size of approximately 100 – 400 nm compared to PPy synthesized with $FeCl_3$ as the oxidizing agent (800 – 1200 nm) or without the surfactant (approximately 2500 nm). Py-SDS-APS had the smallest size around 100 nm, followed by Py-TW-APS, Py-CTAB-APS, Py-SDS-Fe, and Py-CTAB-Fe. PPy* exhibited the largest size as measured by DLS. Additionally, the polydispersity index (PdI) was used to indicate the uniformity or heterogeneity of particle size distributions, as shown in the same figure (**Figure 3-3a**). Py-TW-APS and Py-SDS-APS showed PdI values of 0.12 and 0.19, respectively. Py-CTAB-APS, Py-SDS-Fe, and PPy* had a greater polydispersity than 0.30 (0.40, 0.42, and 0.63, respectively), with Py-CTAB-Fe having the highest PdI of 0.86. A low PdI indicates a narrower size distribution, suggesting a relatively uniform particle size, whereas a higher PdI indicates a broader size distribution with more variability (Danaei et al., 2018).

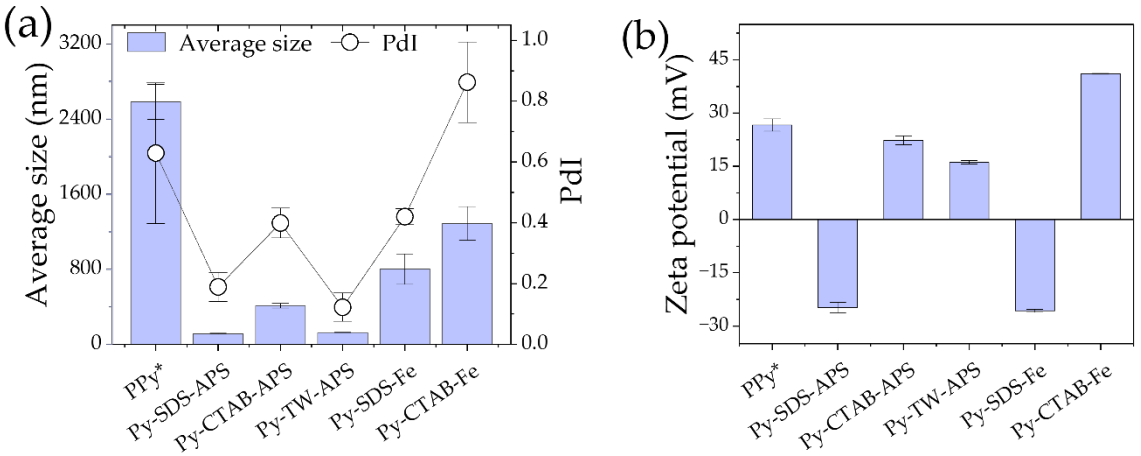

Figure 3-3. Average size, PdI, and zeta potential determined from the zetasizer: (a) average size and PdI and (b) zeta potential.

Figure 3-3b shows the zeta potential. The zeta potential is a measure of the stability of particles in a water-based solution. Ultrapure water was used as the base solution for all preparatory studies. The zeta potentials of PPy varied based on the type of surfactant used. PPy polymerized with an anionic surfactant (SDS) had a negatively charged surface; Py-SDS-APS is −24.80 mV and Py-SDS-Fe is −25.70 mV. For CTAB, the cationic surfactants Py-CTAB-APS and Py-CTAB-Fe had positively charged surfaces of 22.30 mV and 41.10 mV, respectively. Even though TW is a non-ionic surfactant, Py-TW-APS has a positive charge of 16.10 mV since PPy* is a natural positive charge polymer (26.60 mV). As the concentration of TW increased from 2 wt% to 5 wt% to 10 wt%, the zeta potential of PPy decreased slightly from 17.20 mV to 16.10 mV to 15.50 mV, respectively, suggesting that it approached zero.

3.2. Morphology and structure characteristics

The morphology of the PPy samples was examined by SEM, as shown in **Figures 3-4a–f**, which show the SEM images at a magnification of 10,000. The original pictures from SEM were compared to the analysed pictures using Image J software (Version 1.53 K) to evaluate the edges and shape of particles (evaluated using the function Find Edges), as shown on the right of each sample.

PPy polymerized without a surfactant (PPy*) had a sphere-like shape, whereas Py-SDS-Fe and Py-CTAB-Fe exhibited particle clusters. A string of sphere-like forms was observed in the Py-CTAB-APS sample, and a sheet-like structure was created using SDS as the surfactant in Py-SDS-APS. The images of the Py-TW-APS sample (**Figure 3-4d**) were not clear because they could not be completely dried using a freeze-drying process. This may be because Tween 80 has a low melting point (−25 °C) (referred to in the Safety Data Sheet of Tween 80, CAS number 9005-65-6, from TCI America, revision number 2), so it maintains the structure of PPy in a semi-liquid state at room temperature and is difficult to observe by SEM. However, after using Image J software to analyse it, it was determined to be a particle-like form because the author found the edge in a round shape. The various morphologies of PPy examined by SEM proved that the surfactants and oxidizing agents used influenced the PPy shape.

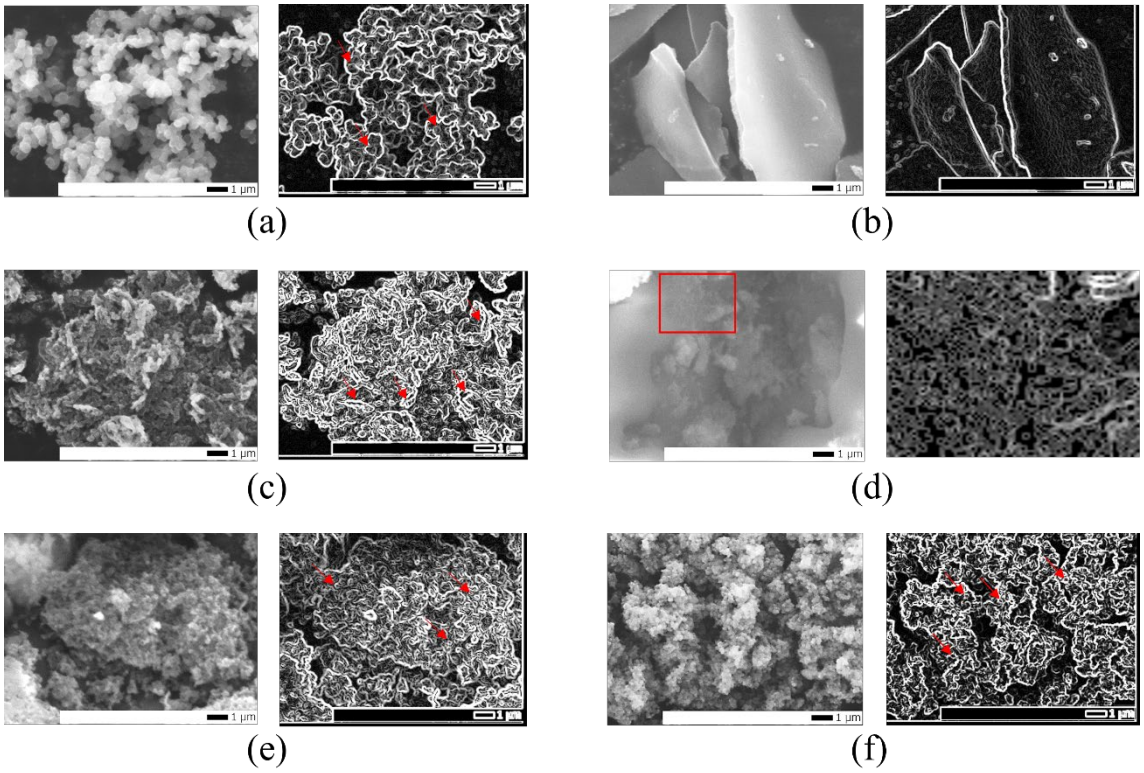

Figure 3-4. SEM image at x10,000 magnifications comparing the original picture (left) and the analysed picture (right): (a) PPy*, (b) Py-SDS-APS, (c) Py-CTAB-APS, (d) Py-TW-APS (the analysed picture received from the red triangle area), (e) Py-SDS-Fe, and (f) Py-CTAB-Fe. The red arrows show where the boundaries were found from the analysis, representing the shape correlated to the SEM picture.

3.3. Electrical conductivity

The resistance of the dry samples was determined using a chemiresistive apparatus, as described in the Materials and Techniques section, to define the electrical properties of the PPy samples. The resistance (R) is derived from the reverse value of the slope from the graph correlation between the voltage (V) and current (I) using Ohm's law ($V = IR$ and $R = 1/\text{slope}$), as shown in **Figure 3-5a**. Subsequently, the conductivity of the samples was calculated from the resistance using the equation described in the Materials and Methods section, as shown in **Figure 3-5b.** The results showed that PPy samples prepared with SDS had higher conductivity, arranged in the following order: Py-SDS-Fe, Py-SDS-APS, Py-CTAB-APS, Py-CTAB-Fe, and PPy*. However, the conductivity of PPy* was not significantly different from that of Py-CTAB–Fe ($p > 0.05$). For the Py-TW-APS

sample, the electrical conductivity was not measurable because it could not be dried using a freeze-drying process, as mentioned in Section 2.2.

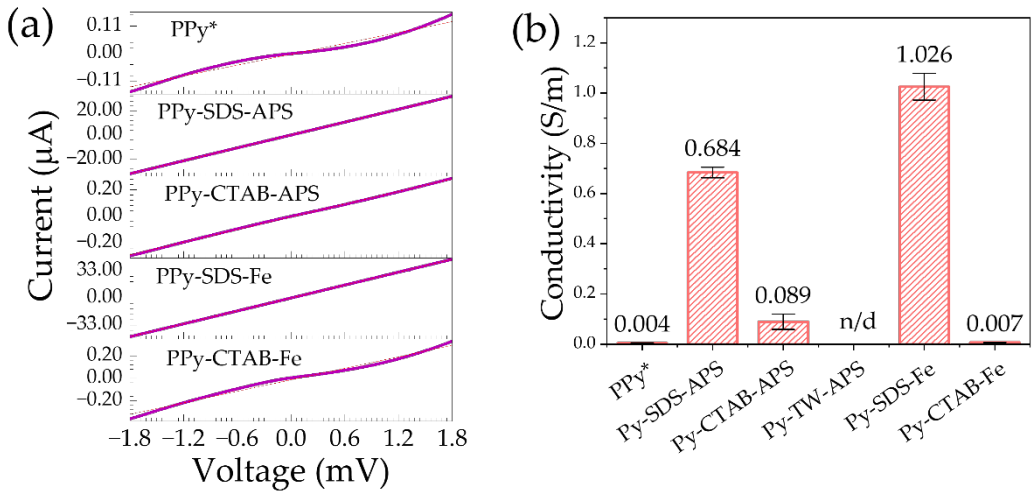

Figure 3-5. (a) I/V graph data determined from the using the LSV mode; the dashed line refers to the slope fitted from Origin software (OriginPro 2023, Student version 10.0.0.154) and (b) conductivity calculated from resistance based on each sample.

3.4. Raman spectra and bipolarons/polarons ratio

After dialysis, the Raman spectra of PPy suspensions were analysed using Raman spectroscopy with a 532 nm excitation laser to determine the chemical information of PPy, with a focus on peak characterization, and to calculate the bipolaron and polaron ratio. This study focused on three regions: C–C ring deformation, C–H deformation, and C–C ring stretching. In each region, both the bipolaron and polaron structures can be found in different Raman shift wavenumbers depending on the PPy production. For C–C ring deformation, bipolarons were observed at 926 – 939 cm^{-1}, and polarons were observed at 963 – 985 cm^{-1}. The C–H deformation region exhibited polarons at 1050 – 1056 cm−1 and bipolarons at 1079 – 1084 cm^{-1}. C–C ring stretching was observed for polarons at 1330 – 1344 cm^{-1} and for bipolarons at 1377 – 1382 cm^{-1}. The polarons associated with the C=C stretching peak were observed within the range of 1562 – 1593 cm^{-1}, and the presence of the bipolaron structure was observed within the range of 1600 – 1618 cm^{-1}.

Figure 3-6a shows the Raman spectra of the PPy samples. In the C–C ring deformation region, the peak bipolaron of PPy* is at 931 cm^{-1}, and it is obvious that the bipolaron of Py-SDS-APS shifted to the right (from 931 cm^{-1} to 945 cm^{-1}) and that of Py-CTAB-APS and Py-CTAB-Fe shifted to the left (to 922 cm^{-1}). While the polaron of the C–C ring deformation of PPy* is at 967 cm^{-1}, from this point, Py-SDS-APS shows a slight shift from 967 cm^{-1} to 973 cm^{-1}. In addition, those of Py-CTAB-APS and Py-CTAB-Fe shifted to the right to 987 cm^{-1}. Notably, the spectral positions of the bipolaron and polaron in the Py-CTAB-APS and Py-CTAB-Fe samples clearly shifted out from each other compared to the other samples. The shifted peaks of polarons far from bipolarons indicated that Py-CTAB-Fe has a lower oxidative chain of PPy (Ishpal & Kaur, 2013). For the C–H deformation area, the author found that in Py-TW-APS and Py-CTAB-Fe, there was no peak in the bipolaron structure compared to the other samples.

For Py-SDS-APS and Py-SDS-Fe, the polaron shifted from reference line 1048 to the right, indicating an increase in oxidized PPy (Y.-C. Liu & Hwang, 2000). For C–C ring stretching, all samples exhibited a polaron structure at 1333 – 1342 cm^{-1} and a bipolaron at 1376 – 1379 cm^{-1}, whereas Py-CTAB-Fe had no bipolaron peak but showed a peak shift at 1411 cm^{-1}, which was attributed to the antisymmetrical inter-ring C–N stretching of oxidized PPy. The polarons associated with the C=C stretching peak were observed in every sample in the range of 1563 – 1583 cm^{-1}, but the bipolaron structure connected to the C=C stretching cannot be determined. However, the C=C stretching area exhibited the most prominent peak feature observed when comparing each sample. A broader morphology of the peak can be discerned in the Py-CTAB-Fe and Py-CTAB-APS samples, whereas it appeared narrower in the Py-TW-APS, Py-SDS-Fe, and Py-SDS-APS samples.

Figure 3-6b illustrates the ratios of bipolaron and polaron peak intensities in relation to other locations, namely C–C ring deformation, C–H deformation, and C–C ring stretching, except in the C=C stretching region because the sample produced for this study could not be discovered; as a result, the ratio in this particular area remains undetermined. The apparent variation in the ratio appears in the C–H deformation region; the bipolaron and polaron ratios of PPy produced using SDS were greater than those of the other samples, even when either APS or $FeCl_3$ was used as an oxidizing agent. These

ratios were used to further investigate the bipolaron and polaron structures in the PPy samples, which may provide information on the electronic properties of PPy.

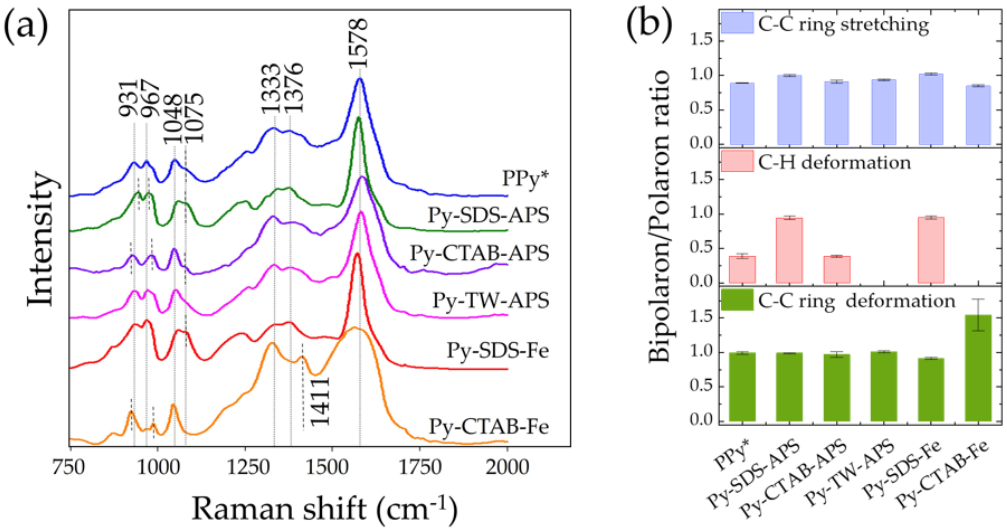

Figure 3-6. (a) Raman spectra and (b) bipolaron/polaron ratios of the samples. Samples composed of PPy were synthesized with SDS, CTAB, and TW as surfactants and APS and $FeCl_3$ as oxidizing agents.

3.5. UV-Vis-NIR absorption

Figure 3-7a shows the UV-Vis-NIR absorption spectra. The spectral characteristics were slightly influenced by the presence of the surfactant and oxidizing agent and supported the oxidative structure of the samples found in the Raman spectra. All PPy samples presented their maximum absorption around 460 nm in ultrapure water, which corresponds to π-π* transition and refers to the neutral and polarons in PPy (Bayat et al., 2021; Kausaite-Minkstimiene et al., 2015; Trchová & Stejskal, 2018). In addition, the samples represented a peak over the wavelength of 800 nm and up to 970 nm, and the peak around 800 – 900 nm referred to the oxidized bipolarons of PPy (Kausaite-Minkstimiene et al., 2015; Scott et al., 1984). **Figure 3-7b** shows the band gap calculated from Tauc plot as described in the Materials and Methods section. These data were used to support the conductivity of PPy samples. The low band gap referred to high conductivity properties due to the reduction in the gap between the valence band and the conduction band (Hazarika & Kumar, 2013; Iurchenkova et al., 2021).

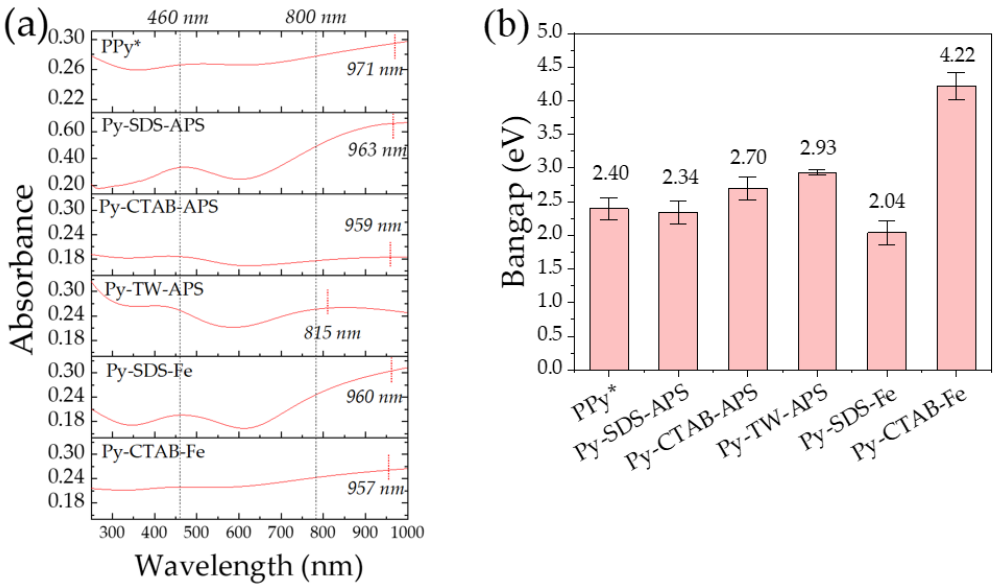

Figure 3-7. (a) UV-Vis-NIR absorption ranged between 250 nm and 1000 nm and (b) band gap calculated from UV-Vis-NIR absorbance by Tauc equation.

4. Discussion

The DLS experiment showed that Py-SDS-APS presented the smallest diameter, followed by Py-TW-APS, Py-CTAB-APS, Py-SDS-Fe, Py-CTAB-Fe, and PPy*. Notably, using a surfactant can reduce the PPy size compared to not using a surfactant. In addition, polymers with anionic surfactants, such as SDS, tended to have a smaller average size than those made with cationic surfactants, such as CTAB, or nonionic surfactants, such as TW, which was similarly found in Hoshina Y. et al. (Hoshina et al., 2012) and Zoromba M. et al. (Zoromba et al., 2021), for example. This could be because the negatively charged SDS (OSO^{3-} groups) can stabilize the growing PPy particles, thereby preventing excessive growth and aggregation (Hazarika & Kumar, 2013). When using constant SDS or CTAB, the size differed depending on the type of oxidizing agent used. When APS was utilized, the PPy size was lower than that of $FeCl_3$, as shown in **Figure 3-3a**, which is similar to the hydrogel created by Bo et al., even though the unreacted molecules did not wash away (Bo et al., 2018). In addition, $FeCl_3$ may substantially increase the ionic strength of the solution compared to APS, and higher ionic strengths can diminish electrostatic repulsion among the developing polymer chains, resulting in larger aggregates (Dai et al., 2006; Talens-Alesson et al., 2002). The average size obtained was

evaluated using PdI. The Malvern Panalytical Co. Ltd. (Malvern, United Kingdom) defines PdI as having dispersibility ranging from 0.05, indicating a high monodispersed, to 0.70, indicating a broad size distribution. Therefore, according to the PdI results in **Figure 3-3a**, Py-TW-APS and Py-SDS-APS demonstrated a fair monodispersed (0.12 and 0.19, respectively). An increase in PdI may suggest a greater tendency for particles or molecules to agglomerate (Wen et al., 2017). Therefore, the size distribution was significantly larger, presumably due to sample aggregation, such as in the case of Py-CTAB-Fe, PPy*, Py-SDS-Fe, and Py-CTAB-APS.

The difference in the zeta potential (**Figure 3-3b**) between PPy samples polymerized with surfactants and PPy* indicated that Py was polymerized within the micelles of the surfactants because Py monomers were predicted to be located in the hydrophobic core of the surfactant micelles because of the hydrophobic structure of the pyrrole monomer (Log P = 0.75). Consequently, the zeta potential of PPy is determined by the type of hydrophilic head of the surfactant facing the exterior (Liu et al., 2002; Ravichandran et al., 2012). Additionally, the high negative charge in Py-SDS-APS and Py-SDS-Fe tended to increase the stability of the sample more than the positive charge due to hydrodynamic interactions and electrostatic repulsion between particles (Hazarika & Kumar, 2013). However, if the size of the sample is large, the zeta potential is affected by gravitation more than hydrodynamic forces (Paúrová et al., 2020), such as in the case of Py-SDS-Fe, which shows a negative charge and large size. For Py-CTAB-Fe, PPy* and Py-CTAB-APS contain a positive charge, which makes them simpler to aggregate, corresponding to a high PdI and large average size. However, in the case of Py-TW-APS, this sample also showed a positive charge, as confirmed by the intrinsic properties of the PPy structure. However, TW can stabilize PPy in water because it absorbs onto the surface of particles and provides steric stabilization, where the physical barrier of the absorbed surfactant layer protects particles from coming close enough to aggregate (Izza et al., 2021).

The results from the average size and zeta potential refer to the interaction between the Py monomer, surfactant, and oxidant during polymerization based on the hydrophobic/hydrophilic properties and electrostatic forces among them. These reactions can lead to different morphologies. As shown in **Figure 3-4a**, SEM showed a cluster of particles in PPy*, Py-CTAB-APS, Py-SDS-Fe, and Py-CTAB-Fe, corresponding to the

average size and PdI detected by DLS, except in the case of Py-SDS-APS, which found a sheet-like form with a large morphology.

In the absence of a surfactant, PPy* has a particle form, which has been normally observed in many studies (Brusamarello et al., 2021; Dubey, 2023b; Omastová et al., 2003). The morphology of Py-SDS-APS is a sheet-like, which might be because of electrostatic interactions between the natural positively charged PPy* and the head group of the surfactants (SO^{3-}). This finding was different from that reported by Zhang et al. (Zhang et al., 2006), who reported that in the presence of APS and $FeCl_3$, no regular polypyrrole nanostructure was observed. Their findings differed from those of this study, possibly because PPy prepared with SDS remained at low concentrations close to the CMC of SDS and the proportion between each component was not the same. Therefore, it may affect micelle formation when mixed. However, they believed that the uneven shape differs from that without SDS, resulting from the residual SDS in the PPy structure after drying.

For polymerization with $FeCl_3$ (Py-SDS-Fe), the author found a cluster of particle-like forms, which is similar to a study using sodium dodecylbenzenesulfonate (DBSNa) as an anionic surfactant (Omastová et al., 2003). However, unlike in the case of Yussuf et al. (Yussuf et al., 2018), who found that using $FeCl_3$ as an oxidizing agent showed fibrillar morphology, they used a lower SDS concentration (around 0.02 M) and only performed 4 hours reaction time at room temperature. It is possible that the short polymerization time and the proportion of monomer and surfactant may have affected PPy morphology as discussed in Chapter 2. However, their work supported that fibrillar morphology showed better conductivity properties than the globular form when they were used as an oxidizing agent. In this work, the author also found that using $FeCl_3$ as an oxidant in the SDS system resulted in higher conductivity, as shown in **Figure 3-5b**, but it showed a globular shape compared to using APS, which represents a sheet-like structure. Additionally, the author found ferric element (Fe) in the PPy structure from electron dispersive X-ray spectroscopy (EDS) when $FeCl_3$ was used (as shown in **Table 3-2**), which might occur because it cannot be completely removed after dialysis. Therefore, the intrinsic properties may have affected the conductivity of PPy more than the shape morphology of these samples. Additionally, regarding the electrostatic force that might have occurred from Fe^{+} between particles, as mentioned above (Dai et al., 2006; Talens-

Alesson et al., 2002), this interaction force may disrupt sheet-like forming and increase porosity in the PPy structure (Yu et al., 2024). Some works reported that a specific higher porous PPy structure represented a higher surface area and an increase in its electronic properties (Tang et al., 2024; Y. Wang et al., 2023).

Table 3-2. Elemental concentrations (atom%) of PPy sample from EDS analysis.

Sample	C	O	S	N	Fe	Cl
PPy*	77.31	21.23	1.46	-	-	-
Py-SDS-APS	80.18	16.52	3.30	-	-	-
Py-CTAB-APS	70.26	18.09	1.64	10.01	-	-
Py-TW-APS	76.09	22.31	1.60	-	-	-
Py-SDS-Fe	74.51	20.90	3.40	-	1.05	0.14
Py-CTAB-Fe	72.10	12.20	-	14.20	0.77	0.73

However, in the case of Py-CTAB-Fe, even though Fe was found in the structure, Py-CTAB-APS had better conductivity. This might be because the morphology of Py-CTAB-APS tended to resemble a string-bead structure, which is like the results obtained by Khadem et al., even though they used a lower CTAB concentration and a polymerization period of 4 hours at room temperature and under N_2 atmosphere (Khadem et al., 2017). Moreover, Zhang X. et al. prepared polymerization at 0 – 5 °C for 24 hours and obtained a ribbon-like form when CTAB was used with APS and obtained sphere-like PPy using a CTAB surfactant and $FeCl_3$ (Zhang et al., 2006), similar to Py-CTAB-Fe in the work by Zoromba and members (Zoromba et al., 2021). Therefore, by employing CTAB, it is possible to alter its morphology into a ribbon or wire form by the process of self-assembly between the positively charged cations from the cationic surfactants and the negatively charged anions from the oxidizing agent APS ($S_2O_8^{2-}$) (Khadem et al., 2017; Zhang et al., 2006), but the oxidizing agent has the effect to form a PPy structure. However, the conductivity of PPy polymerized with CTAB was less than that of PPy polymerized with SDS in either APS or $FeCl_3$. Therefore, SDS is a dopant that is useful to dope a conductive structure of PPy better than CTAB. In addition, by predicting the average size, zeta potential from the zetasizer, and morphological structure from SEM,

the author can estimate the interactions between the Py monomer and surfactant, as shown in **Scheme 3-3**.

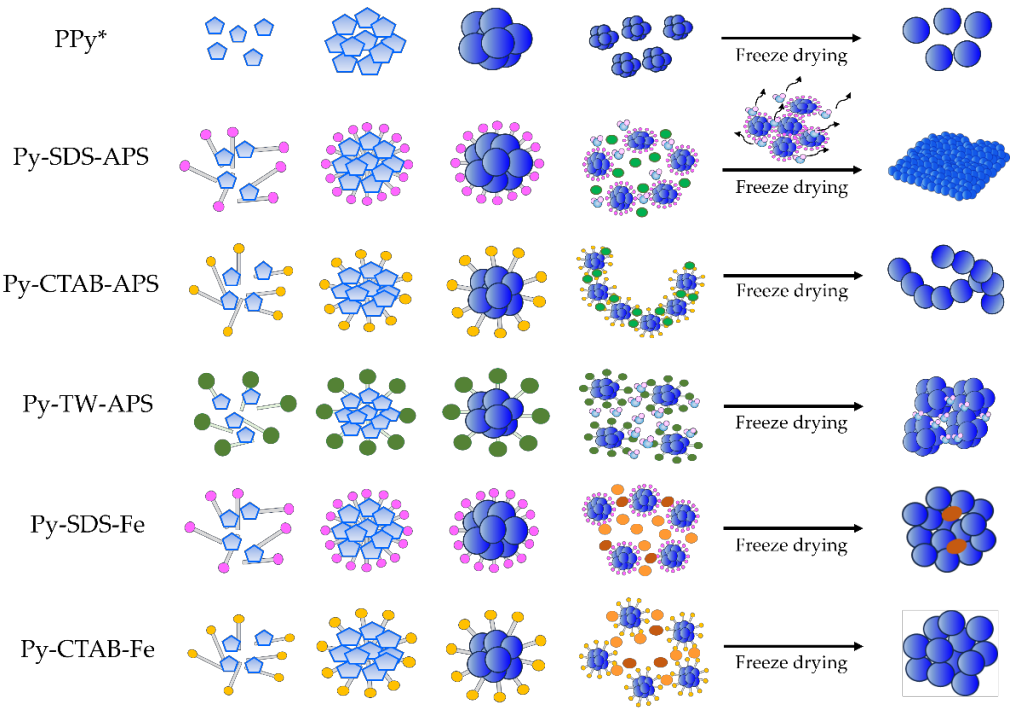

Scheme 3-3. Illustration of the formation of PPy within a surfactant structure. This image depicts the micelles formed by the surfactants in an aqueous solution. The hydrophilic heads of the surfactants are oriented outward (circle with pink, yellow, and green), whereas the hydrophobic tails face inward (gray stick), forming the core of the micelle. The polymerization of Py occurs inside these micelle structures, with Py monomers linked together to form polymer chains. PPy chains were confined within the hydrophobic core of the surfactant micelles.

As shown in **Scheme 3-3**, the Py monomer aggregation during polymerization is affected by the interaction between surfactants and oxidants, resulting in various morphologies. In addition, their interactions led to distinct chemical structures in their PPy, as determined the chemical structure of PPy samples from Raman spectroscopy, which found varying peak characteristics, as shown in **Figure 3-6a**. By studying the chemical structure observed via Raman spectroscopy, the author could define whether the morphology is related to the intrinsic chemical structure of PPy. As mentioned in the

results section, the author found that in Py-TW-APS and Py-CTAB-Fe, there was no peak in the bipolaron structure, which is similar to the peak characteristic of PPy deprotonated by ammonium hydroxide from Trchová et al., which represents a low-oxidative structure (Trchová & Stejskal, 2018). In addition, PPy polymerized with $FeCl_3$ showed a sphere-like structure, and Raman spectra characteristics similar to those work (PPy*), even though they used 633 nm or 785 nm laser excitation. In addition, they used dye acids (methyl orange and Acid Blue 25) to dope a bipolaron structure and found that the peak at bipolaron increased as to form a nanotube structure with higher conductivity, which is also similar to other works (Bober et al., 2018; Y. Li et al., 2017).

Moreover, as in the previous work, the author observed that the ratio between the bipolaron and polaron of PPy polymerized with SDS (sheet-like form) differed from that of PPy without a surfactant (sphere-like form), particularly in the C–H deformation area. Additionally, the bipolaron and polaron structures refer to the oxidative structure of PPy (Appel et al., 1999; Brédas et al., 1984; Santos et al., 2007); a higher bipolaron and polaron ratio indicates higher conductivity properties. Therefore, the ratio between the bipolaron and polaron was calculated from the peak intensity, including the three main areas, as shown in **Figure 3-6b**. The graph shows that the C–H deformation area represented the bipolaron/polaron ratio of each sample and showed that PPy polymerized with SDS had a higher ratio of bipolaron and polaron than other conditions, corresponding to the high UV-Vis-NIR absorption at around 960 nm (**Figure 3-7a**) and low band gap value calculated from absorbance (**Figure 3-7b**). This phenomenon was consistent with the negatively charged surface and high-conductivity measurements from instruments of Py-SDS-APS and Py-SDS-Fe. Therefore, the consistency between them revealed that SDS incorporated into the PPy structure was the major dopant that enhances the conductivity properties of PPy by interfering with the PPy structure and raising the bipolaron structure in the C–H deformation area, which might be due to the electrostatic interaction between positively charged PPy and the anionic head group of SDS conducting the PPy structure.

Additionally, **Figure 3-8** represents the conclusion of the relationship between each PPy property in this work. The author can categorize them into two groups: low band gap and high band gap (red dot line), in which the low band gap corresponded to high bipolaron and polaron ratios (black dot line), which correlated to the theory and other

works (Hazarika & Kumar, 2013; Iurchenkova et al., 2021). In this category, it confirmed the relationship between using SDS in Py polymerization and electronic properties (conductivity and band gap) and bipolaron and polaron ratios in C–H deformation but did not link to the morphology.

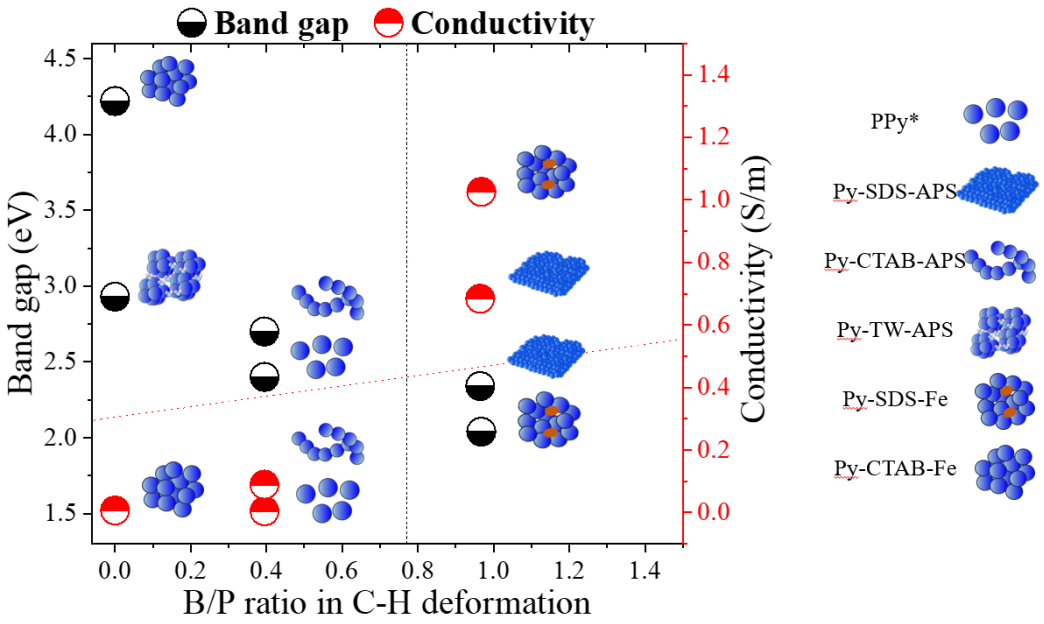

Figure 3-8. The relationship between the bipolaron and polaron ratio (B/P ratio) in the C–H deformation region, conductivity and band gap.

However, the bipolaron and polaron ratio results went against the first hypothesis, which said that the morphology should match the bipolaron and polaron ratio in C–H deformation. However, the fact that the rise in the bipolaron and polaron ratios in the C–H deformation region is linked to SDS provides us with insight into where SDS affects the intrinsic chemical structure of PPy, which might be a criterion leading to higher conductance. The data provide additional underpinnings for the future development of PPy properties.

5. Summary

Compared to Py-SDS-APS, Py-CTAB-APS, and Py-TW-APS, the morphology shifts towards a sheet-like configuration when using SDS as a surfactant and shows a higher bipolaron and polaron ratio in the C–H deformation and greater electronic properties. In contrast, Py-SDS-Fe showed a cluster of particle-like form, and the conductivity and the bipolaron and polaron ratio in the C–H deformation of Py-SDS-Fe surpassed that of Py-CTAB-Fe. The results showed that if different oxidants were used, the shape of PPy might not influence the bipolaron and polaron ratio in C–H deformation. However, the ratio of bipolaron to polaron has a strong relation with conductivity. This work highlights that SDS contributes to elevating the bipolaron content within the C–H deformation region of PPy, which may occur through the electrostatic interaction between PPy and the head group of SDS, resulting in the enhancement of its conductivity.

Chapter 4

Tailoring Polypyrrole Morphology and Electronic Properties through CTAB-SDS Self-Assembly

1. Introduction

Semiconductive polymers such as polythiophene, polyaniline, and polypyrrole (PPy) have garnered significant attention due to their remarkable properties, making them ideal candidates for a variety of fields of applications. These polymers conduct electricity through their conjugated electron systems, consisting of alternating single and double bonds (π-π* bonding), which facilitate electron flow across the molecular structure (Kausaite-Minkstimiene et al., 2015). This characteristic has driven innovation in conductive polymer technology, with PPy emerging as a particularly advantageous material for various uses. For instance, PPy has been instrumental in enhancing the sensitivity and functionality of biosensors (De Aguiar et al., 2021; Xiaoqiang et al., 2020). Its excellent conductivity and stability make it a valuable component in the development of efficient and durable energy storage devices (Shabeeba et al., 2022; Zang et al., 2017). Moreover, its biocompatibility and durability properties have led to its use in surface coatings, electronic circuits, and medical equipment (Ashery et al., 2018; Ramanaviciene et al., 2010).

The chemical polymerization method, a conventional approach for producing substantial quantities PPy, employs oxidizing agents to initiate the polymerization of the pyrrole monomer (Py) (Veisi et al., 2023; Wen et al., 2017). This straightforward and highly adaptable method allows for the modification of PPy characteristics under various conditions, thereby expanding its range of applications (Alekseeva et al., 2015; Sravanthi & Manjunatha, 2021; Vernitskaya & Efimov, 1997). Surfactants such as sodium dodecyl sulfate (SDS) and cetyltrimethylammonium bromide (CTAB) are crucial in the modification of PPy. SDS, an anionic surfactant, assists in forming micelles that serve as a framework for polymerization, resulting in nanostructured PPy with a large surface area and enhanced electrical properties (Hazarika & Kumar, 2013; Samwang et al., 2023). On the other hand, CTAB, a cationic surfactant, facilitates the formation of more organized

structures such as nanowires or nanofibers, which exhibit increased electrical capacitance and a larger surface area compared to nanoparticles (Ishpal & Kaur, 2013; Ren et al., 2023).

Catanionic surfactant systems, such as the combination of CTAB and SDS, exhibit unique self-assembly behaviours driven by electrostatic and hydrophobic interactions (Fernández-Peña et al., 2020). These systems arise from the electrostatic interactions between the ionic components of the hydrophilic head groups, leading to variations in surface charge characteristics, as illustrated in **Figure 4-1**. Additionally, hydrophobic interactions occur between the surfactant tails, which differ in acyl chain lengths (C12 for SDS and C16 for CTAB). The self-assembly behaviour of these surfactants leads to the formation of various nanostructures, including micelles, vesicles, and lamellar phases, depending on factors such as composition ratio, concentration (Israelachvili, 2011; Mal et al., 2018; Watanabe et al., 2022), and environmental conditions like temperature (Lone et al., 2021).

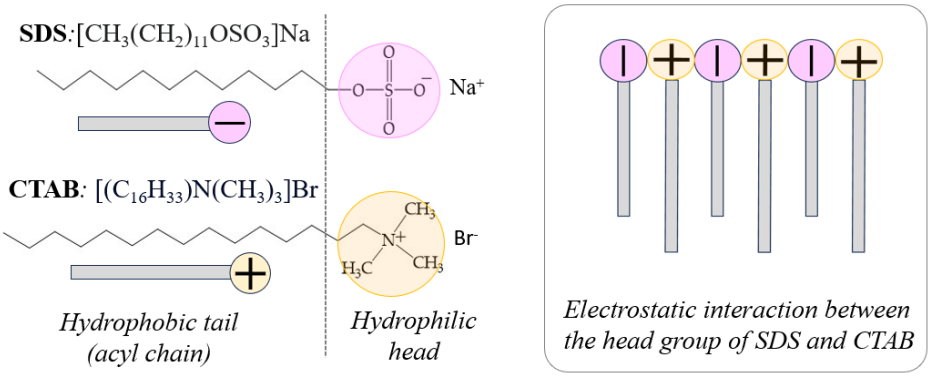

Figure 4-1. Illustrations of the chemical structures of SDS and CTAB.

This catanionic system has paved the way for developing new PPy structures with enhanced characteristics. For example, Xing and Zhao found that adding SDS at a 1:1 molar ratio (0.43 g CTAB and 0.35 g SDS in 100 ml, 40 mM total concentration) transformed the nanofiber structure of PPy into nanoparticles (Xing & Zhao, 2007). As the molar ratio of SDS exceeded that of CTAB, the particle size increased, resulting in agglomerates, as observed with SEM. Das et al. investigated PPy growth patterns using

the electrochemical polymerization of pyrrole in an SDS-CTAB surfactant mixture, finding that increasing the CTAB concentration from 0.0125 mM to 0.30 mM led to the formation of larger PPy aggregates (Das et al., 2010). Similarly, Dubey et al. prepared PPy in various SDS-CTAB mixtures and found that a mixture of 10 mM SDS and 5 mM CTAB produced smaller, globular PPy particles (Dubey, 2023a), corroborating the finding of Das, Xing and Zhao. These studies highlight the significant impact of mixed surfactant systems on the morphology and electrical properties of PPy. Increasing the molar proportion of SDS in a low-concentration SDS-CTAB mixture (2 – 10 mM) resulted in larger aggregates due to stronger electrostatic interactions between the positively charged PPy and SDS compared to CTAB (Xing & Zhao, 2007). This interaction may alter the acyl chain packing in the hydrophobic structure of surfactants, thereby affecting the hydrophilic/hydrophobic environment similar to liposomes (Suga et al., 2018).

Despite these advancements, challenges remain in optimizing the electronic properties and morphology of PPy synthesized in catanionic systems. Our study aimed to achieve two primary objectives: (1) to evaluate the electronic properties of PPy synthesized in a self-assembled catanionic system of CTAB and SDS at higher surfactant concentrations (0.10 M of total concentration), and (2) to investigate the packing density of the acyl chains in the surfactant's hydrophobic tails. By determining these packing density values, we sought to assess the relationship between surfactant interactions and the resultant electronic and morphological properties of PPy. The insights gained from this study could enhance our understanding of the polymerization process in catanionic systems and inform the design of conductive polymers with tailored properties for specific applications.

2. Materials and Methods

2.1. Materials

Py was purchased from Sigma-Aldrich (98 % reagent grade, Sigma-Aldrich Co. LLC, St. Louis, MO, USA) and used without further purification. SDS, CTAB and ammonium persulfate (APS) were purchased from Wako Pure Chemical Industries Ltd. (Osaka, Japan). All preparation solutions required ultrapure water with a resistance of

18.20 MΩ (Direct-Q 3 UV system, Merck Millipore, Osaka, Japan). Indium tin oxide (ITO) glass electrodes were purchased from BAS Inc., Tokyo, Japan. Silver paint with a resistance less than or equal to 1 Ω was purchased from Polycalm, a company based in Japan. Dialysis tube with a molecular weight cutoff (MWCO) of 14 kDa was purchased from NaRiKa Corporation, Tokyo, Japan.

2.2. Surfactants preparation

CTAB and SDS were dissolved in ultrapure water to prepare a stock solution. The solution was then mixed at different CTAB and SDS molar ratios by keeping the total concentration to 0.10 M. The mole fraction of CTAB and SDS was represented as X_{CTAB} and X_{SDS}, respectively, in the following relationship: $X_{CTAB} + X_{SDS} = 1.00$. The surfactant solution prepared at a mole fraction of CTAB as $X_{CTAB} = 0.20, 0.40, 0.50, 0.60$, and 0.80 were labelled as CS20, CS40, CS50, CS60, and CS80, respectively, as shown in **Figure 4-2.**

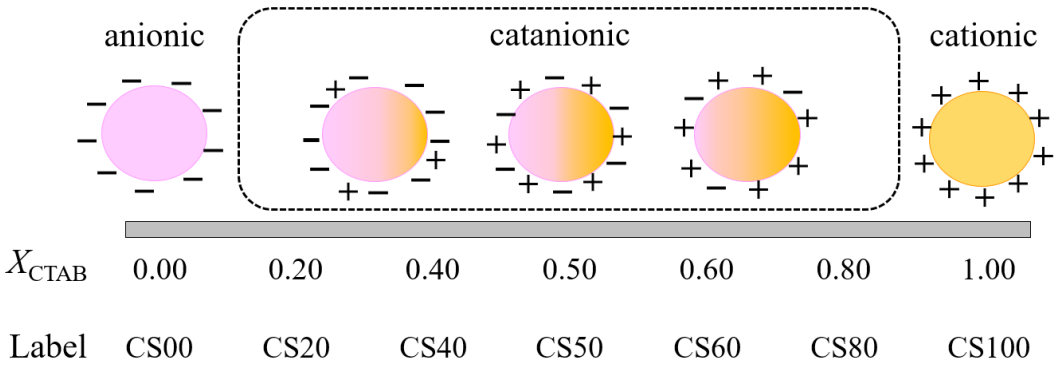

Figure 4-2. Illustrations of the surface charge characteristics in the CTAB-SDS system, depending on the composition of anionic surfactant (SDS) and cationic surfactant (CTAB) in the system.

2.3. Pyrrole polymerization

In the polymerization process, Py monomer was added to the surfactant solution to achieve a concentration of 0.10 M. The surfactant used could be SDS, CTAB, or a combination of both Subsequently, a solution of an oxidizing agent (APS) was gradually added to the mixture while stirring, also reaching a concentration of 0.10 M. The ratio between the oxidizer and the monomer was maintained at 1:1. The solution was stirred

for 24 hours at ambient temperature (25 °C), resulting in the formation of a PPy suspension. The synthesized PPy was dialyzed using a dialysis tube in ultrapure water to remove any unreacted molecules. The PPy sample was freeze-dried and stored in a desiccator until ready for use. The prepared PPy samples were labelled according to the surfactant composition as CS20PPy, CS40PPy, CS50PPy, CS60PPy, and CS80PPy. Samples were denoted as CS00PPy and CS100PPy when Py was polymerized in pure SDS solution (X_{CTAB} = 0.00) and in pure CTAB solution (X_{CTAB} = 1.00), respectively. The experiment procedures are illustrated in **Scheme 4-1**.

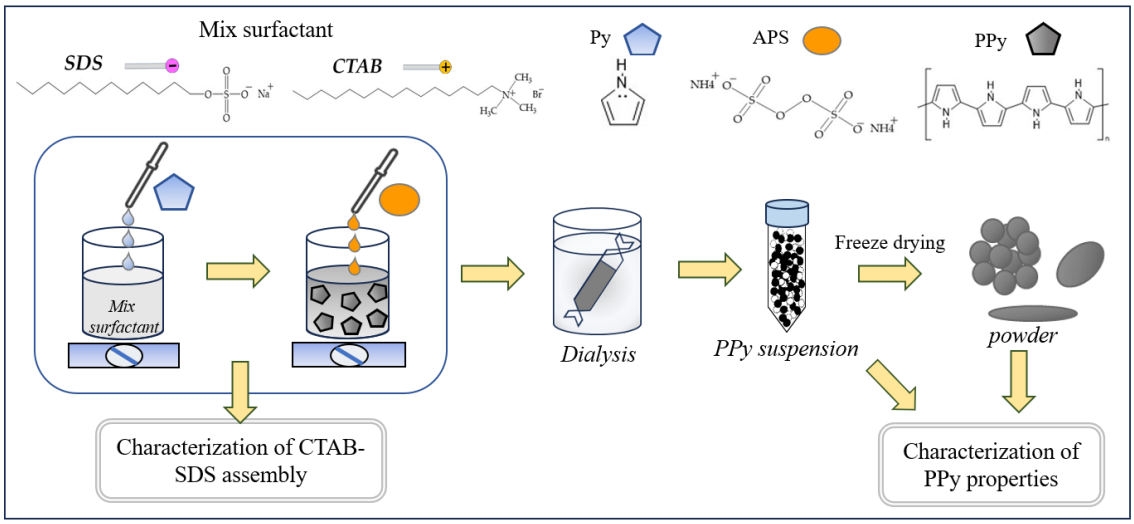

Scheme 4-1. Illustration of experiment.

2.4. Properties Characterization of PPy sample

2.4.1. Size and zeta potential measurement

The average size and zeta potential of the sample were analysed with dynamic light scattering (DLS) and electrophoretic light scattering (ELS) technique, respectively by zetasizer instrument (ZEN5600, Malvern Instruments Ltd., Worcestershire, United Kingdom). All measurements were performed at 25 °C.

2.4.2. Optical density (OD) measurement

The OD was proportional to the size of the self-assembled structures, and turbidity was measured using a Microplate Spectrophotometer (xMark, Bio-Rad, CA, USA). The

experiment was carried out at 500 nm for each sample suspension (100 ml) in a 96-well plate three times at 25 °C.

2.4.3. Packing density (*R*)

Raman spectra of PPy suspensions were investigated using a Raman spectroscopy (HR-800, Horiba, Ltd., Kyoto, Japan) at an exciting laser wavelength of 532 nm. The packing density (*R*) was assessed to quantify the arrangement of acyl chains inside the hydrophobic area of samples. *R*-value was determined by evaluating the relative intensities (*I*) of Raman spectra (after removing background signals) at 2880 cm^{-1} and 2850 cm^{-1} ($R = I_{2880}/I_{2850}$), which consistent to the asymmetric and symmetric vibrations of the ($-CH_2-$) group, respectively.

2.4.4. Bipolarons and polarons structure of PPy

The Raman spectra of PPy were examined using a Raman spectroscopy. The software Origin (Version 2023, OriginLab Corporation, Northampton, MA, USA) was utilized to analyze the highest peak of bipolarons and polarons in the sample, specifically in the areas of C–C deformation, C–H deformation, and C–C stretching. Additionally, the Origin software was used to determine the ratio between the peak intensities of bipolarons and polarons (B/P ratio) in each area.

2.4.5. UV-Vis-NIR absorbance and band gap calculation

UV-Vis-NIR spectroscopy (UV1800, SHIMADZU, Japan) was employed to monitor the oxidative structure of PPy and determined its optical band gap characteristics using Tauc equation, as represented by Equation (1).

$$(\alpha hv)^{1/n} = \alpha_0(hv - E_g) \quad (1)$$

The absorption coefficient (α) is calculated using the formula $2.302 \times A/d$, where d represents the cell thickness (1 cm), and A represents the light absorbance. The photon energy (hv) is measured in electron volts (eV) and is derived from the equation $1240/\lambda$, where λ is the wavelength in nanometers. The Planck's constant (h) is equal to 6.6261×10^{-34} J·s. The photon frequency (v) is determined by dividing the speed of light (C), which is 2.998×10^8 m/s, by the λ. The optical band gap (E_g) is measured in electron volts (eV). The constant band-tailing parameter is denoted as α_o, and the power factor (n) is equal to

2 for an indirect transition band gap (Lertthanaphol et al., 2022; Lin et al., 2018). A linear relationship may be observed between the plot of $(\alpha h\nu)^{1/n}$ and the photon energy ($h\nu$) in a certain range. The optical band gap was determined by extrapolating the point where the straight line intersects the ($h\nu$)-axis.

2.4.6. Electrical conductivity analysis

The resistance of the PPy powder was measured using a modified chemiresistive apparatus, as shown in **Figure 4-3**. To summarize, PPy powder (0.005 – 0.008 g/cm^2) was compressed into pellets using a manual press and placed between two ITO glass electrodes. The initial parameters of the distance between the electrodes and the thickness of the pellet were preserved by utilizing silicone rubber that was 0.80 mm thick. The resistance of PPy was measured and recorded using a two-point probe measuring approach implemented by an Automatic polarization system (HZ-7000, Hokuto Denko Corporation, Tokyo, Japan). The resistance value for each data point was determined by calculating the slope of the current-voltage plot using Ohm's law ($V = IR$). The resistance (R) was obtained by calculating the reciprocal of the slope ($R = 1/slope$) from the I/V plot. The conductivity (σ) of PPy was calculated using the correlations presented in Equations (2) and (3):

$$\rho = \frac{RA}{L} \tag{2}$$

$$\sigma = \frac{1}{\rho} \tag{3}$$

where R indicates the resistance of PPy in ohms (Ω), ρ represents the resistivity of Ppy in ohm-meters (Ω·m), L represents the thickness of the PPy pellet (8.00×10^{-4} m), A represents the area of the sample (1.96×10^{-5} m^2), and σ represent the electrical conductivity in siemens per meter (S/m).

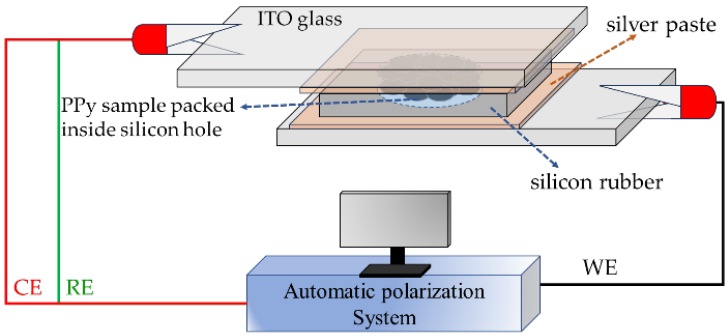

Figure 4-3. A chemiresistive apparatus composing two-electrode cells (ITO) construction connecing to an Automatic polarization system for resistance measurement (CE is counter electrode, RE is reference electrode (Ag/AgCl), and WE is working electrode).

2.4.7. Morphology observation

The shape of the dried PPy powder was examined using scanning electron microscopy (SEM) (JCM-7000, JEOL Ltd., Japan) with the loading voltage of 15.0 kV. Crystalline behavior of PPy waw examined by Multipurpose X-ray diffraction (XRD) instrument and manipulated using an X-ray system (Rigaku SmartLab (D/teX Ultra, SC), Rigaku Holdings Corporation, Tokyo, Japan) with Cu-Ka radiation (1.5418 Å) operating at 45 kV and 200 mA in the range 10 – 80° with step width 0.02°.

2.4.8. Cryogenic transmission electron microscopy (cryo-TEM)

The morphology of catanionic surfactant were characterized using cryo-TEM. Sample preparation was performed using Vitrobot mark IV from Thermo/FEI, USA. Upon freshly glow discharged Mo QUANTIFOIL grids (R2/2, 200 mesh), 2.40 µL of the sample was applied. The carbon-coated grids were subjected to a 20-second glow discharge at 10 mA and then blotted for 4 seconds at a blotting force of 10 at 25 °C and 100% relative humidity. They were then immersed in liquid ethane. Using a Titan KRIOS microscope from Thermo Fisher Scientific, USA. The microscope operated at an accelerating voltage of 300 kV. The magnification was 59000, with a pixel size of 0.14 nm. Data processing and analysis were conducted using ImageJ software (Version 1.53 K, National Institutes of Health, USA).

3. Results and discussion

3.1. Characterization of CTAB-SDS assembly

The characteristics of the CTAB-SDS assembly were analysed before and after the addition of pyrrole monomer by Dynamic Light Scattering (DLS), Optical Density (OD) measurements, and Raman spectroscopy. This investigation aimed to observe the morphological characteristics of the assembly prior to the initiation of the polymerization process. Catanionic solutions were prepared and allowed to equilibrate at room temperature (25 °C) overnight. These solutions were thoroughly mixed before being analysed, referred to as the state before Py addition. The Py monomer was then added to the surfactant solution while stirring slowly (200 rpm). The mixture was left to settle for 2 hours at room temperature before being analysed, referred to as the state after Py addition.

3.1.1. Average size from DLS

DLS measurements were conducted to determine the size distribution of micelles in the catanionic surfactant both before and after the addition of pyrrole monomer. Before adding Py, the average size of the CTAB-SDS assemblies increased with a higher CTAB composition: from 2.20 nm, 3.70 nm, 165.50 nm, to around 13,500 nm for CS00, CS20, CS40, and CS50, respectively. In particular, the large size found in CS50 could indicate the aggregation of catanionic surfactant (Nakanishi et al., 2005). The average size was accompanied by higher Polydispersity Index (PdI) values ranging from 0.15 to 0.67, indicating a broader size distribution (**Figure 4-4a**) (Danaei et al., 2018). PdI values were used to indicate the degree of non-homogeneity in the particle size distribution. PdI values below 0.05 indicates a high level of homogeneity, whereas a PdI above 0.70 suggests a broader range of particle sizes or particle aggregation (Danaei et al., 2018). Following this trend, the average sizes were around 3300 nm and 3500 nm for CS60 and CS80, with PdI values exceeding 0.70, suggesting significant aggregation and polydispersity. In pure CTAB, the average size was around 1.95 nm with a PdI of 0.14, indicating a low polydispersity.

Upon adding the Py monomer (**Figure 4-4b**), the average sizes of CS00Py, CS20Py, and CS100Py were increased to 241.00 nm, 27.50 nm, and 9.80 nm, respectively. CS00Py and CS100Py showed significant aggregation with high PdI values at 0.36 and

0.46, respectively, while CS20Py exhibited a lower PdI (0.09), indicating a more monodispersed state. For CS40Py, CS50Py, and CS60Py, average sizes were decreased to 94.50 nm, 237.90 nm, and 275.30 nm, with PdI values of 0.11, 0.30, 0.42, respectively, suggesting a more uniform particle distribution and reduced aggregation after Py addition. CS80Py formed a gel-like structure, rendering size detection impossible.

Compared to previous reports, the observed changes in average size and PdI suggested a transformation of simple micellar structures into larger structures such as rod-like micelles, vesicles, or lamellar structures—or vice versa when the size decreases. Lone et al. reported that increasing the temperature in a mixture of CTAB and bmimDS (1-butyl-3-methylimidazolium dodecyl sulfate) from 20 °C to 40 °C at an X_{CTAB} of 0.50 led to a structural transition from vesicles to micelles, with the size decreasing from around 150 – 200 nm to around 25 – 35 nm (Lone et al., 2021). They suggested that these smaller structures could be rod-shaped micelles, as determined by small-angle X-ray scattering (SAXS) and small-angle neutron scattering (SANS). Oliveira et al. synthesized cationic and anionic surfactants from serine-derived compounds and studied vesicle formation in their mixture (Oliveira et al., 2023). They found that vesicles formed at molar fractions of cationic surfactants ranging from 0.40 to 0.90, with diameters ranging from 20 nm to 400 nm, as confirmed by DLS, Video-Enhanced Light Microscopy (VELM), and Cryo-SEM. Therefore, the changes in average size found in this work suggest the transition of surfactant structure when Py was present, which might imply a transition of micelles or vesicles.

Furthermore, Kuperkar et al. observed micelle structures in CTAB at concentrations of 0.01 M and 0.15 M using cryogenic transmission electron microscopy (cryo-TEM) (Kuperkar et al., 2008). Their images revealed similarities to the micelle structures observed in CS00Py and CS100Py in our study (**Figure 4-5**), where we could not distinguish distinct structural differences before and after the addition of the monomer. In the case of CS00Py, the size determined by cryo-TEM did not correspond to the average size obtained from DLS (241.00 nm). This discrepancy may be attributed to the heterogeneous structure indicated by the high size variation (131.60 nm) and high PdI value (0.36), which indicate a heterogeneous structure. These factors made it challenging to observe larger structures using cryo-TEM. The supporting information provides details on sample preparation and measurement for cryo-TEM.

Large or complex structures are often challenging achieving the necessary contrast and resolution in cryo-TEM due to limitations in ice layer thickness and particle orientation during vitrification (Weis et al., 2022). Consequently, we were unable to observe the structure for all samples. However, observable features were identified in CS00Py and CS100Py, as well as in some structures of CS20, CS40, CS20Py, and CS40Py (**Figure 4-5)**. For the CS20 and CS20Py samples, micelle-like structures were observed, but no significant changes occurred after the addition of the monomer. For CS40, a micelle-like structure was also observed. However, the size found by cryo-TEM differed from that obtained by DLS, possibly due to the reduced frequency of larger particles observed, which may be attributed to the variation in particle size, as indicated by the relatively high PDI of CS40 (0.38). After adding the Py monomer, CS40Py exhibited a transition to a disc-like and vesicle-like structure corresponding to a size around 94.50 nm. The disc-like form was similar as found by the literature (Johansson et al., 2008). However, since we did not perform tilting the sample grid and taking images, we cannot conclusively confirm it is disc. Therefore, we name it disc-like.

3.1.2. The optical density (OD)

OD measurements were conducted at 25 °C to quantify the turbidity of the assemblies before and after the addition of the Py monomer, as shown in **Figure 4-4c**. The OD values increased as the CTAB composition rose from CS00 to CS40, remained stable until CS60, and then dropped to CS80 and CS100. The inclusion of the Py monomer had a slight impact on the turbidity of the CTAB-SDS system, with similar OD values before and after Py addition, except for CS20Py. Notably, CS20Py exhibited a lower OD after the addition of Py, corresponding to a reduction in PdI (0.09). This PdI suggested that CS20Py formed highly monodisperse micelles after the addition of Py. The increase in size from 3.73 nm to 27.45 nm indicated aggregation of the catanionic structure with Py. However, the OD data suggested that the CTAB and SDS assemblies were disrupted after Py addition. Visual observations also revealed aggregation, suggesting that the particles may have aggregated during the size measurement, resulting in a lower average size than is visually apparent (**Figure 4-4e**). The observation indicated that aggregation occurred in CS20, affecting the size measurement. After Py was added to CS20 (CS20Py), the catanionic assembly progressed to form micelles with a size of

27.45 nm, consistent with low OD (Lone et al., 2021), marking a significant discrepancy of OD in this composition.

For CS00Py, a higher average size and PdI from DLS were observed despite a low OD value, assuming to the rupture of the SDS structure after Py addition. A similar trend was observed for CS100Py, which exhibited a larger size and high PdI after Py addition without a change in OD. However, the size of 9.78 nm refers to micelle assembly, correlated with low OD. In contrast, CS40Py, CS50Py, and CS60Py exhibited lower PdI values and smaller average sizes after Py addition, indicating lower particle polydispersity. However, the OD remained high, corresponding to turbidity, as observed visually, suggesting the presence of micro-aggregation of the catanionic structure (Lone et al., 2021). For CS80Py, the average size could not be detected after Py addition due to its gel-like structure; however, before Py addition, CS80 exhibited micro-aggregation correlated with visual observation.

3.1.3. Raman spectra and packing density

Raman spectroscopy is a powerful technique that used to explore the vibrational modes of molecules, providing information about molecular structure and interactions. When applied to lipid assemblies, Raman spectroscopy can reveal details about the acyl chain packing (Jurašin et al., 2017; Watanabe et al., 2022). The peak intensity of Raman spectra at 2850 and 2880 cm^{-1} represents the symmetric ($-CH_2-$) and asymmetric ($-CH_2-$) stretching, respectively. By measuring the intensity of these peaks, we can calculate the packing density, denoted as R, where $R = I_{2880}/I_{2850}$. High R-values (>1.00) indicate a high degree of acyl chain packing, often found in ordered states of lipid membranes (J. Han et al., 2017), meaning the hydrocarbon chains are closely packed, resulting in a more rigid structure. Low R-values (<1.00) indicate a lower degree of packing, corresponding to disordered states. In this work, the peak intensity at I_{2880} and I_{2850} of acyl chain of CTAB and SDS was determined (**Figure 4-6)** and used to examine the packing density value as shown in **Figure 4-4d**.

The Raman spectra indicated that the R-value before adding Py was lower than 1 for CS00, CS20, CS40, and CS100, referring disorder state. In contrast, R-value was higher than 1.00 for CS50, CS60, and CS80, indicating an order structure of the catanionic system. This trend corresponded with the average size, and PdI observed in DLS. After

adding Py, the *R*-value for CS20Py remained essentially unchanged, which differed significantly from the OD measurement. This difference might be affected by the variation in surfactant aggregation during the phase change from micelles to vesicles, similar to findings in a ternary phase diagram for sodium octyl sulfate (SOS)/CTAB/H_2O at 25 °C (O'Connor et al., 1997). In contrast, the *R*-values for CS40Py increased significantly to above 1.00 ($p < 0.05$, determined by a two-sample t-test with n = 6), indicating a more ordered state in the presence of the Py monomer, which corresponding to a disc-like and vesicle-like form observed from cryo-TEM. This finding showed that investigating the *R*-value might assist in classifying structures of CTAB-SDS assembly if OD measurement represented a similar value. When the composition ratio of CTAB and SDS was close to 1:1 for CS50Py and CS60Py, a slight increase in *R*-value was observed but was not significant compared to before and after Py addition. The *R*-value decreased for CS00Py, CS80Py, and CS100Py, suggesting a more disordered state when the Py monomer was added.

According to the size, OD, and *R*-value results, introducing Py monomers into CS00Py and CS100Py disrupted the surfactant assembly, slightly intensifying the disorder and resulting in larger sizes. Despite these changes, the micelle structure was still maintained, as observed from cryo-TEM. In the cases of CS20Py, CS40Py, and CS80Py, the lack of correlation between size, OD, and *R*-value might be influenced by the transition between ordered and disordered states after Py addition. The cryo-TEM image of CS40Py displayed a disc-like and vesicle-like form, which supports the presence of an ordered structure or an increase in the *R*-value after the addition of the Py monomer. We also found that CS50 and CS60 likely developed lamellar or vesicular structures after the addition of the Py monomer, as suggested by the average size (Lone et al., 2021) and the consistency between size, high OD, and *R*-values.

This study demonstrated that the *R*-value, OD values, and average size results indicate that the CTAB/SDS ratio influences the degree of structural order in the system, both in the presence and absence of Py. Although only some samples were observed by cryo-TEM, the morphologies identified were consistent with the *R*-value measurements. As the CTAB-SDS composition changes, **Figure 4-4f** presents a possible assembly characterization of the catanionic system, depicting how it forms before and after the addition of Py.

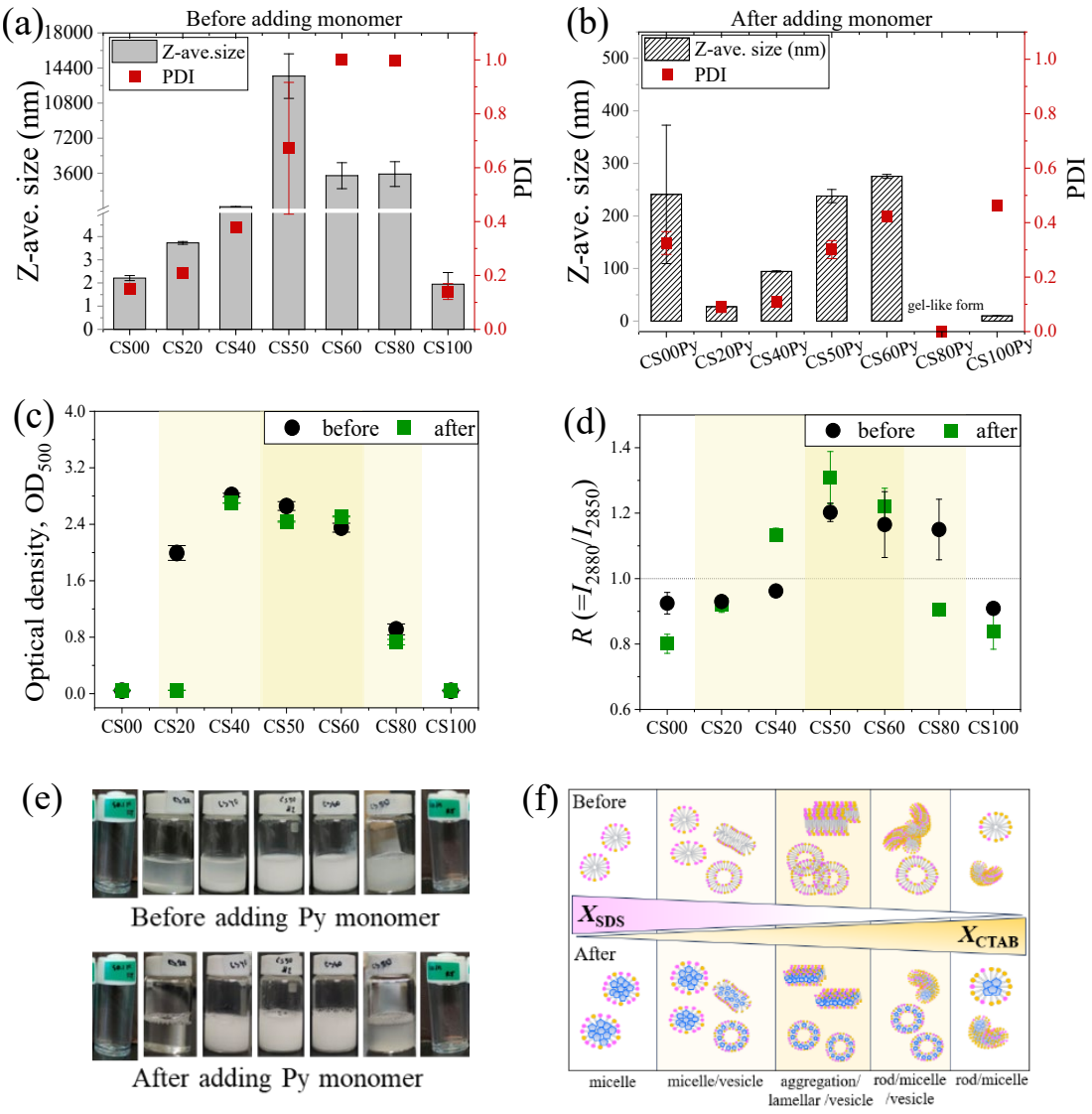

Figure 4-4. Results of (a) average size and PdI of CTAB-SDS assembly before Py adding and (b) after Py addition, (c) optical density measurement, (d) packing density (*R*-value), (e) visual comparison of the CTAB-SDS solution from CS00 (left) to CS100 (right) before and after Py addition, and (f) a proposed assembly model of the CTAB-SDS system showing structural changes with varying CTAB-SDS compositions, comparing configurations before (above the line) and after (below the line) Py addition.

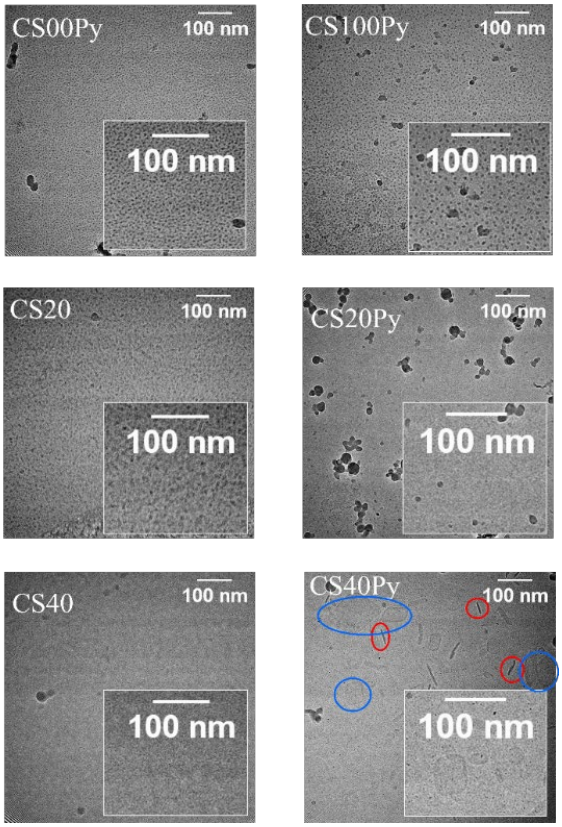

Figure 4-5. Cryo-TEM image at 59,000x magnification with a pixel size of 0.14 nm. Red circles indicate disc-like shapes, while blue circles highlight vesicle-like structures.

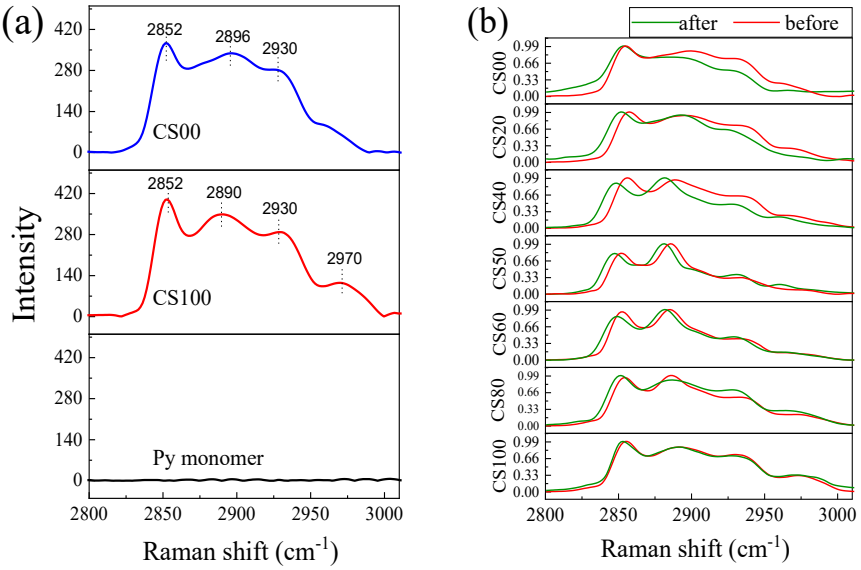

Figure 4-6. (a) Raman spectra of SDS, CTAB and Py monomer after processed by OriginPro software and (b) peak at the wavelength from 2800 cm^{-1} to 3000 cm^{-1}, in zone of acyl chain of surfactants comparing between before and after adding Py monomer.

3.2. PPy Synthesis and properties characterization

PPy was synthesized by chemical polymerization by gradually adding APS to a catanionic surfactant and Py monomer under continuous stirring for 24 hours at 25 °C. Afterward, unreacted molecules were removed through dialysis. The average size and surface charge properties were analysed using a zetasizer instrument to examine its characteristics after preparation. The chemical information was analysed through Raman spectroscopy, while the electronic properties were determined from optical band gap and electrical conductivity measurements.

3.2.1. Average size and surface properties of PPy

The average size and zeta potential of diluted PPy suspensions in ultrapure water (0.10 – 0.20 mg/ml) were analysed to understand the impact of varying proportions of CTAB and SDS surfactants. The average size of PPy particles, as shown in **Figure 4-7a**, varied significantly with the addition of CTAB. Initially, the particle size increased from 118 nm (CS00PPy) to 611 nm (CS20PPy) and further to 1700 nm (CS40PPy). However, as the CTAB content increased further, the particle size progressively decreased to 746 nm (CS50PPy), 613 nm (CS60PPy), 444 nm (CS80PPy), and 413 nm (CS100PPy). The PdI values corresponded to the average sizes obtained from DLS, which ranged from 0.39 to 0.80, suggesting a broader size distribution. Meanwhile, the CS00 sample exhibited a PdI value of 0.20, indicating more monodisperses state than the other samples. These results suggested that adding CTAB in the polymerization process can significantly influence the average size of PPy, depending on its ratio to SDS. SDS and CTAB served as a soft templates facilitating the formation of PPy structures (Qin & Qiu, 2019). SDS or CTAB formed micelles above their critical micelle concentrations (CMC) of 8.2 mM and 0.92 mM, respectively (Dubey, 2023). When combined, the catanionic surfactants exhibited increased packing density, forming larger micelles or vesicles. Consequently, the DLS approach detected the diverse sizes of PPy particles.

Figure 4b illustrates the zeta potential of the samples. The data showed that varying the proportions of CTAB and SDS significantly impacted the surface charge characteristics of the PPy particles. As the CTAB composition increased from CS00PPy to CS100PPy, the zeta potential shifted from −22.3 mV to +22.5 mV. This variation was attributed to the ionic nature of the hydrophilic heads of SDS (SO_3^-) and CTAB (N^+),

which tend to charge positively as the composition of CTAB in catanionic surfactant increases. The change in zeta potential confirmed the chemical polymerization and the formation of PPy in collaboration with the catanionic surfactant.

The study of size and zeta potential of PPy revealed that the addition of CTAB in varying proportions significantly influences the particle size and zeta potential. The results highlighted the role of SDS and CTAB as soft templates, affecting the micellar structure and, consequently, the PPy particle characteristics.

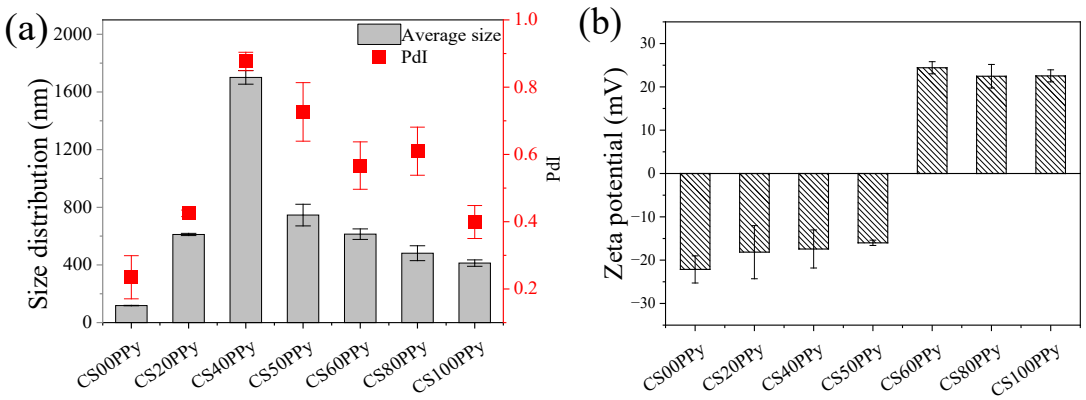

Figure 4-7. (a) Average size and PdI and (b) zeta potential of Py polymerized with CTAB-SDS system at variation of composition.

3.2.2. Raman spectra and bipolaron/polaron ratio (B/P ratio)

Raman spectroscopy was employed to examine the chemical information of PPy suspensions after dialysis, using a 532 nm excitation laser. This technique was utilized to determine the packing density in the area of the acyl chain and to provide detailed chemical information, focusing on the bipolarons to polarons ratios.

The Raman spectra, depicted in **Figure 4-8a**, reveal insights into the chemical composition of PPy. The specific study targeted three spectral regions: C–C ring deformation, C–H deformation, and C–C ring stretching. In the C–C ring deformation region, bipolarons were identified by peaks at 926 – 939 cm^{-1}, while polarons appeared between 963 cm^{-1} and 985 cm^{-1}. Polarons were observed at 1050 – 1056 cm^{-1} for the C–H deformation region and bipolarons were detected between 1079 cm^{-1} and 1084 cm^{-1}. In the C–C ring stretching region, polaron peaks were seen from 1330 cm^{-1} to 1344 cm^{-1},

and bipolaron peaks were noted from 1377 cm^{-1} to 1382 cm^{-1}. Additionally, polaron-related C=C stretching peaks were found in the 1562 – 1593 cm^{-1} range, whereas bipolaron structures were identified between 1600 cm^{-1} and 1618 cm^{-1} (Morávková et al., 2021; Santos et al., 2007; Trchová & Stejskal, 2018).

Figure 4-8b presents the ratio of bipolaron to polaron (B/P ratio) peak intensities across these regions. Raman spectra measurements showed that PPy prepared with SDS (CS00PPy) exhibited a bipolaron structure in the C–H deformation region, resulting in a higher B/P ratio compared to PPy polymerized with CTAB (CS100PPy). Additionally, as the composition of CTAB in the CTAB-SDS system increased from X_{CTAB} = 0.20 to 0.80, the B/P ratio in the C–H deformation region decreased. In contrast, other areas, such as C–H stretching and C–C stretching, remained constant in the range of 0.90 to 1.00 and 1.00 to 1.20, respectively. This indicates that the SDS composition specifically influenced the bipolaron structure in the C-H deformation region.

In addition, the author analysed samples of PPy that were synthesized with and without SDS, as well as a 0.10 M CTAB solution and a 0.10 M SDS solution (**Figure 4-8b**), to explore a potential interference peak caused by surfactants. The results showed that the CTAB solution had no peak at around C–H deformation, whereas SDS solution analysis revealed a small peak at 1061 cm^{-1}, representing C–C stretching for SDS (Lee et al., 2021). Although the SDS solution found the peak near the C–H deformation region, the intensity was too low compared to the peak in PPy samples. Furthermore, the prominent peak found in both SDS and CTAB solutions was the peak intensity at around 2850 cm^{-1}, 2890 cm^{-1}, and 2930 cm^{-1}, which corresponds to the symmetric and asymmetric vibrations of the ($–CH_2–$) group and $–CH_3$, respectively. Therefore, the authors assumed that the C–H structure of SDS or CTAB did not impact the peak intensity of C–H deformation in PPy samples within the range of polarons (1050 – 1056 cm^{-1}) or bipolarons (1079 – 1084 cm^{-1}). On the other hand, Py monomer or PPy also did not show any peaks at the specific wavelength for packing density evaluation.

These data revealed a clear trend: as the SDS composition decreases, the C–H deformation also decreases. This relationship supported the hypothesis that the bipolaron structure of PPy correlated with the SDS composition. The presence of bipolarons and polarons was linked to the oxidation degree of PPy, impacting its conductivity properties,

as corroborated by previous Chapter. The preferential binding of the pyrrole ring played a significant role in this context, as noted by Santos et al. (Santos et al., 2007). They observed that pyrrole rings were primarily linked at the alpha-alpha (α–α) positions as well as at other positions, such as the beta-beta (β–β) and beta-alpha (β–α) positions; this linkage was supported by NMR information (Scott et al., 1984). These linkage positions seemed to influence the molecular structures of dimers and trimers and their oxidative states due to their effect on π–π^* bonding within the PPy structure (Mahun et al., 2020), resulting in deformation or stretching, as observed in Raman spectra (Morávková et al., 2021).

The author hypothesized that since SDS functioned as a soft template for pyrrole polymerization, its negatively charged head group ($–SO_3^-$) facilitated electrostatic interactions with the positively charged PPy. This interaction might affect the linkage of pyrrole chain polymerization during polymerization and induce oxidative sites, particularly in the bipolaron structure in the C–H deformation region, as the Py monomer polymerizes to form a polymer of PPy at this bonding (Samwang et al., 2024; Santos et al., 2007). Hence, PPy prepared with a higher SDS concentration showed a higher B/P ratio. This phenomenon could differ from using CTAB as a template because it showed a low B/P ratio for PPy prepared with CTAB. These findings significantly contribute to our understanding of pyrrole polymerization and guide potential future research.

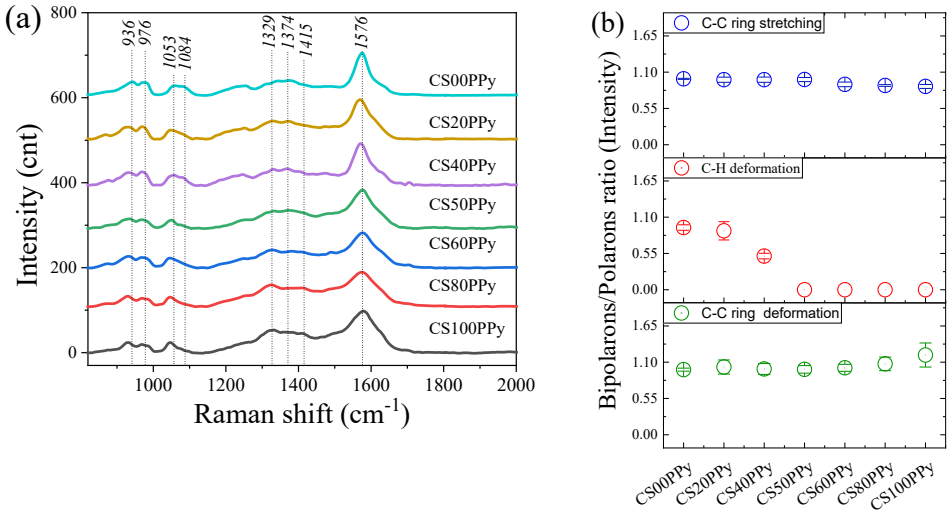

Figure 4-8. (a) Raman spectra and (b) bipolaron to polaron ratio at C–H deformation area, evaluated from the peak intensity by OriginLab software.

The Raman spectroscopy analysis revealed the connection between the CTAB-SDS composition and the bipolarons structure of PPy. It was clear that the SDS composition had influenced the B/P ratio, especially in the C–H deformation region. The author supposed that the SDS composition influences the B/P ratio in the C–H deformation region because of the electrostatic interaction between the negatively charged head group of SDS and the positively charged PPy, affecting the polymerization process and the resulting bipolarons structure.

3.2.3. Electronic properties analysis

The study aimed to analyse the oxidative structure of PPy samples and explore the relationship between the composition of CTAB and SDS surfactants and the resulting electronic properties. Key findings include the influence of surfactant composition on the optical band gap and electrical conductivity of the samples.

Figure 4-9a displays the UV-Vis-NIR absorbance spectra of the samples measured at wavelengths ranging from 200 nm to 1000 nm. The results show a decrease in the oxidative sites of the samples as the SDS composition decreased. This is evidenced by the maximum absorption observed around 460 nm and 900 nm, corresponding to the π–π^* transition of neutral and polaron structures (Bayat et al., 2021; Kausaite-Minkstimiene et al., 2015; Trchová & Stejskal, 2018) and bipolaron structures (Dubey, 2023a; Kausaite-Minkstimiene et al., 2015), respectively. As shown in **Figure 4-9b**, the optical band gap, calculated from UV-Vis-NIR absorbance using the Tauc equation, exhibited a slight decrease when CTAB was initially introduced into the SDS system, dropping from 2.33 eV for CS00PPy to 2.14 eV for CS20PPy. However, with further increases in CTAB composition, the band gap displayed slight variations, shifting from 2.14 eV to 2.18 eV, 2.13 eV, 2.22 eV, and finally to 2.47 eV for CS40PPy, CS50PPy, CS60PPy, CS80PPy, and CS100PPy, respectively. For PPy, the band gap typically ranges around 1.00 eV to 3.10 eV (Atta et al., 2023; Bayat et al., 2021), depending on synthesis parameters such as the type of counter ions, degree of doping, and oxidation state during polymerization. A reduction in the band gap indicates that less energy was required for an electron to transition from the valence band to the conduction band (Iurchenkova et al., 2021; Salzner et al., 1998).

Figure 4-9c presents the electrical conductivity, calculated from resistance measured by chemiresistive device, which gradually decreased from 0.687 S/m for CS00PPy to 0.530 S/m, 0.340 S/m, 0.282 S/m, 0.054 S/m, 0.003 S/m, and 0.011 S/m for CS20PPy, CS40PPy, CS50PPy, CS60PPy, CS80PPy and CS100PPy, respectively. This trend in conductivity corresponds to the results reported by Xing S. and Zhao G. (Xing & Zhao, 2007). PPy was produced utilizing catanionic surfactants at two distinct concentration ratios of CTAB to SDS: 10:4 and 4:10. Their findings demonstrated that an increased concentration of SDS resulted in a considerably elevated conductivity (8.51 S/cm) in comparison to samples with a lower SDS concentration (10:4 mM), which had a conductivity of just 0.50 S/cm. Dubey N. (Dubey, 2023a) prepared PPy with 10 mM SDS, 5 mM CTAB, and catanionic surfactants of 5 mM CTAB and 10 mM SDS. The specific capacitance, one semiconductor property, established values of 158 Fg^{-1}, 129 Fg^{-1}, and 107 Fg^{-1}, interpreting that using SDS mono surfactant provided better electronic properties. Their findings supplemented the conductivity results in this study, which demonstrated that CS00PPy exhibited favourable electronic characteristics compared to other situations.

The author observed that the optical band gap values did not correlate with the decreasing trend in conductivity and the B/P ratio as the mole fraction of CTAB in catanionic surfactant increased. The author hypothesized that the complex interactions between CTAB and SDS may interfere with the UV-Vis-NIR absorbance, thereby affecting the optical band gap calculated from Tauc equation. This interference could stem from turbidity caused by the assembly of CTAB and SDS within the PPy structure. Although the author attempted to mitigate this effect by diluting the PPy suspensions and observed no significant absorbance at relevant wavelengths, the complexity of the system suggests that optimized parameter may be necessary to obtain accurate band gap values (Jubu et al., 2022; Makuła et al., 2018). Furthermore, the relationship between band gap and electrical conductivity is not always straightforward due to several influencing factors. Conductivity is determined by the band gap and the density and mobility of charge carriers (Benramache et al., 2013), which can be affected by doping, impurities or structural defects. As a result, materials with similar band gaps might exhibit different conductivities based on these factors.

In this work, the sizeable sheet-like structure of CS00PPy may play a crucial role in enhancing electrical conductivity properties by increasing charge mobility via reducing contact resistance. The observed decrease in electrical conductivity corresponded to a reduction in the B/P ratio in the C–H deformation region of the PPy samples. These findings suggested that the electrical properties of PPy could be tailored by adjusting the CTAB and SDS compositions, particularly the SDS composition. The results highlight the significance of SDS composition in enhancing the electrical conductivity of PPy, which is consistent with previous works (Omastová et al., 2003; Xing & Zhao, 2007).

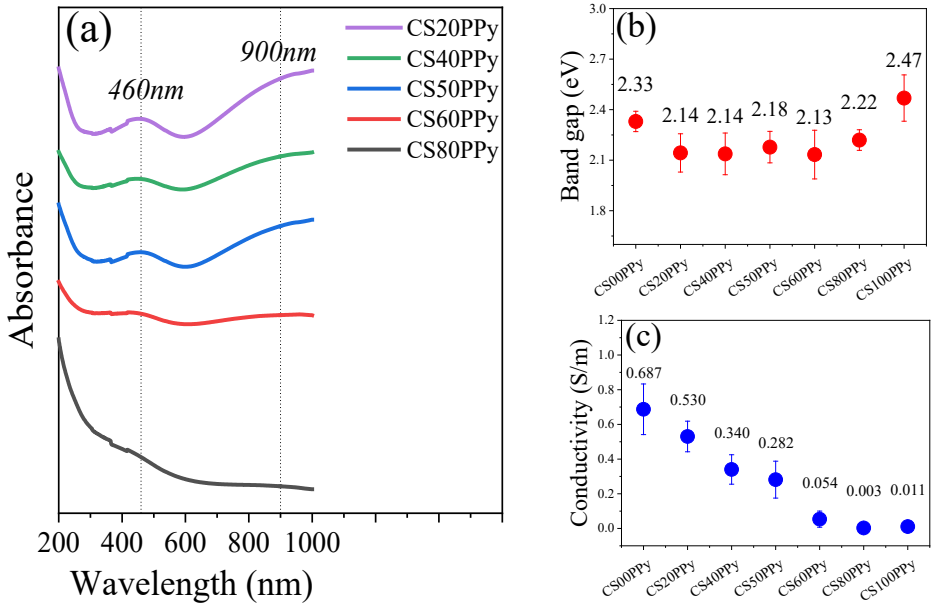

Figure 4-9. (a) UV-Vis-NIR absorbance, (b) band gap, and (c) conductivity determined from resistance.

3.2.4. Morphology observation from Scanning Electron Microscopy (SEM)

The PPy suspensions produced after dialysis were dried using a freeze-drying apparatus. The shape and crystallinity of dried PPy powder were examined using SEM and XRD techniques. SEM was used to obtain high-resolution images of the PPy samples, allowing for a detailed view of their morphology. XRD was used to analyse the crystal structure of the PPy powder, providing insights into its physical properties.

Figure 4-10 shows SEM images of the PPy samples, illustrating the subtle influence of different CTAB and SDS compositions on their morphology. The CS00PPy sample, produced with SDS as the only surfactant, presented a sheet-like shape. The electrostatic interactions between the PPy polycations and SDS head molecules might cause these sheet-like structures or agglomeration (Dubey, 2023a). For CS20PPy and CS40PPy, the morphology changed from the sheet-like structure observed in CS00PPy to a disc-like shape after drying, which is consistent with the disc-like structure observed in the cryo-TEM images of CS40Py. The disc-like shape was first developed and found for CS40PPy, CS50PPy, and CS60PPy, in which the molar ratio between CTAB and SDS closed to 1:1. The alteration might be related to the increasing presence of CTAB in the catanionic system and reduce the importance of electrostatic interactions between SDS and PPy in SDS-only systems (Dubey, 2023a; Xing & Zhao, 2007). The combination of SDS and CTAB surfactant caused more complex micelle production, resulting in these transition morphologies between micelle, vesicle, and lamellar or reversed to micelle (Mal et al., 2018).

However, the morphology of CS40PPy, CS50PPy, and CS60PPy observed from SEM revealed that PPy didn't become spherical vesicles as a hypothesis but formed a disc-like shape resulting from bilayer formation, which corresponded in the self-assembly of amphiphilic molecules or non-ionic surfactants researches (Kawabata et al., 2012, 2014; Weiss et al., 2008) and a disc-like structure as found from cryo-TEM image. Their densification was caused by the surfactant's ability to make spherical micelles into disc-like particles under varying concentrations (Weiss et al., 2008). To clarify the surfactant transformation at this state, the author illustrated the formation pathway as shown in **Figure 4-11**. The transition from spherical micelles (**Figure 4-11a**) to non-spherical micelles (**Figure 4-11b**) and then to disc-like structures (**Figure 4-11c**) occurs due to electrostatic interactions between SDS and CTAB. At near 1:1 composition, the discs aggregate and bend into vehicles (**Figure 4-11d**) and a lamellar phase emerges at an exact 1:1 ratio (**Figure 4-11e**). The intermediate states (**Figure 4-11b-d**) correspond to the observed structures in CS40Py, consistent with a higher *R*-value compared to the state before adding pyrrole. These morphological transformations were a testament to the dynamic nature of catanionic surfactant and its influence on PPy morphology.

At the highest CTAB composition in the catanionic system (CS80PPy), the PPy samples exhibited a particle agglomeration that seemed like a string-like form, characteristic of CTAB's influence. These morphologies were consistent with those reported by Xing S. and Zhao G. (Xing & Zhao, 2007) despite this study's higher total surfactant concentration. PPy polymerized with CTAB formed spherical micelles or string-bead structures depending on the oxidizing agent (Ishpal & Kaur, 2013; Khadem et al., 2017; Ren et al., 2023). The oxidizing agent, in this case, was ammonium persulfate (APS), which dissociated in water to form sulfate anion ($S_2O_8^{2-}$). The self-assembly between the positively charged cations of CTAB and the negatively charged anions of the oxidizing agent APS led to a string-bead or wire structure (Khadem et al., 2017; Zhang et al., 2006). The reduction in SDS content reduced the sheet-like structure formations.

Reiterating the key findings, it became clear that the surfactant ratio played a pivotal role in shaping the morphology of PPy. With higher SDS content (CS00PPy), the structures tended to be more planar and sheet-like, whereas increasing the CTAB content (CS80PPy) shifted the morphology towards spherical particles. The intermediate compositions (from CS20PPy to CS60PPy) demonstrated a transition phase, where the morphology shifted from sheets to agglomerated discs to densely packed spheres. This transformation underscored the significant role of CTAB and SDS in determining the structural characteristics of PPy through their micellar formations as interpreted from the acyl chain packing and electrostatic interactions between ionic groups.

Furthermore, in relationship to the electrical property, this work calculated conductivity from resistance, which was measured by a chemiresistive device. The device measured both intrinsic and extrinsic resistance of samples (Nah et al., 2022). The intrinsic resistance was connected to the conductivity of PPy based on its properties, such as the crystalline structure, while the extrinsic resistance was associated with the contacts between the PPy samples. The discussion in previous work, Chapter 2 and Chapter 3, established that a small size particle induced the contact resistance, resulting in a decrease in overall conductivity. Consistent with Xing S., Zhao G. and Dubey N., as mentioned above, they found good electronic properties in surfactants with high SDS composition, which also correlated to an agglomeration and large globule structure of PPy as compared to low SDS composition, which found nanoparticles or globular structures (Dubey, 2023a; Xing & Zhao, 2007). Therefore, as observed from SEM, at a high composition of

SDS, a compacted structure of PPy was associated with better conductivity. When the composition of SDS in the CTAB-SDS system was deducted, the PPy size tended to be smaller and became a sphere-like form, as found in CS100PPy. Therefore, the transformation to sphere-like form showed a reasonable relationship between conductivity calculated from resistance and composition ratio between CTAB and SDS.

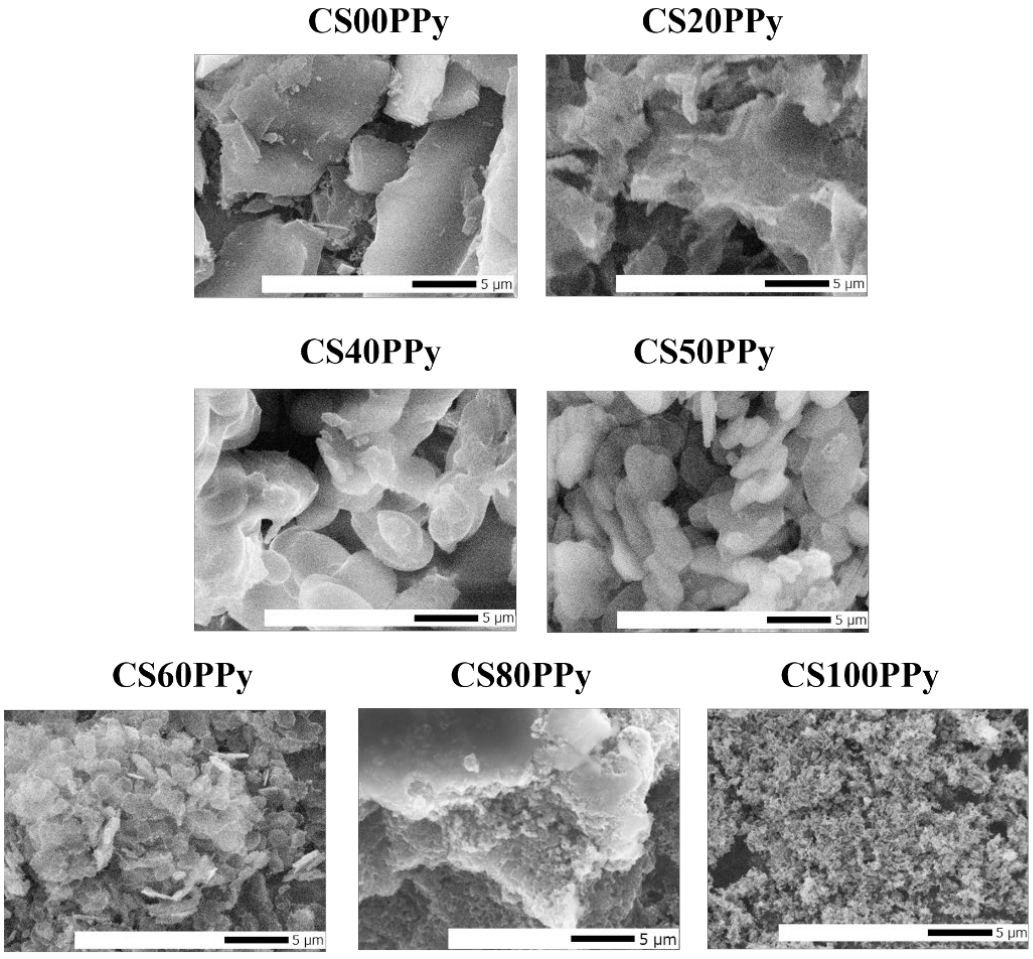

Figure 4-10. SEM of PPy synthesized in variation of CTAB-SDS composition at x5000 of magnification.

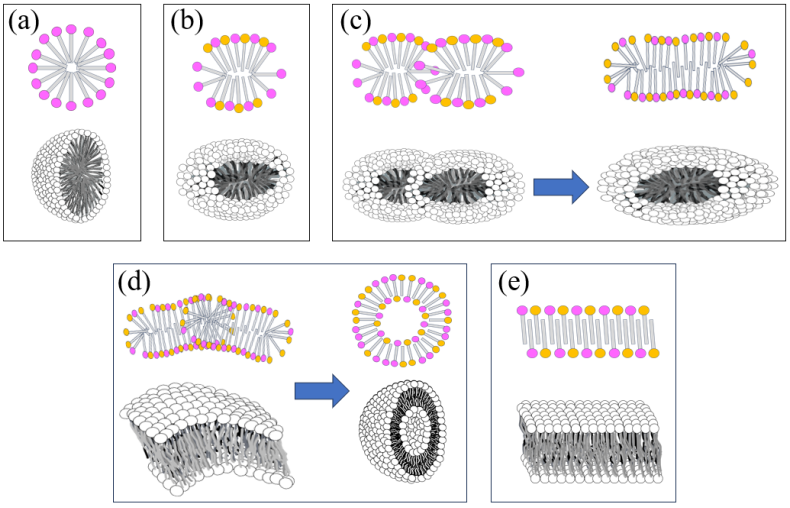

Figure 4-11. Illustration depicting the possible formation stages of CTAB-SDS assemblies: (a) spherical micelle, (b) non-spherical micelle, (c) disc-like structure, (d) vesicle from agglomerating and bending structure of disc-shape particles, and (e) lamellar structure. The coloured images represent 2D cross-sections of the corresponding grayscale 3D structures.

3.2.5. X-ray Diffraction (XRD)

Figure 4-12a represents the results from the XRD analysis. XRD examination of PPy produced without surfactants (PPyn) revealed an amorphous structure with a peak intensity at 28.48°, characterized by a broad scattering peak between $2\theta = 15 - 30°$. Based on Bragg's law (Gopi et al., 2016), the distance between adjacent lattice planes or interplanar spacing (called *d*-spacing) was interpreted from the angle of diffraction (θ), referring to the crystal plane in the sample structure. For PPyn, the *d*-spacing was 0.31 nm. Similarly, PPy synthesized using SDS (CS00PPy) also displayed a broad scattering peak with a peak at 20.50°, indicative of an amorphous structure with *d*-spacing of 0.43 nm. In contrast, PPy polymerized with CTAB (CS100PPy) exhibited distinct peaks at 19.90°, 20.84°, and 22.75°, indicating 0.45 nm, 0.43 nm, and 0.39 nm of *d*-spacing. Our research consistently showed similar broad scattering peaks across all samples, regardless of the varying composition ratios of CTAB and SDS (**Figure 4-12b**), which presented the *d*-spacing between 0.39 nm and 0.47 nm. The same peak position suggested the distance between adjacent lattice planes was the same. These results suggested that the crystallinity of PPy was not significantly affected by the surfactant composition in this

work. This conclusion aligned with the findings of Chang et al. (He et al., 2003) and further confirms the non-crystalline characteristics of PPy produced using SDS or CTAB, as noted by Gupta et al. (Dutta Gupta et al., 2011) and Dubey (Dubey, 2023).

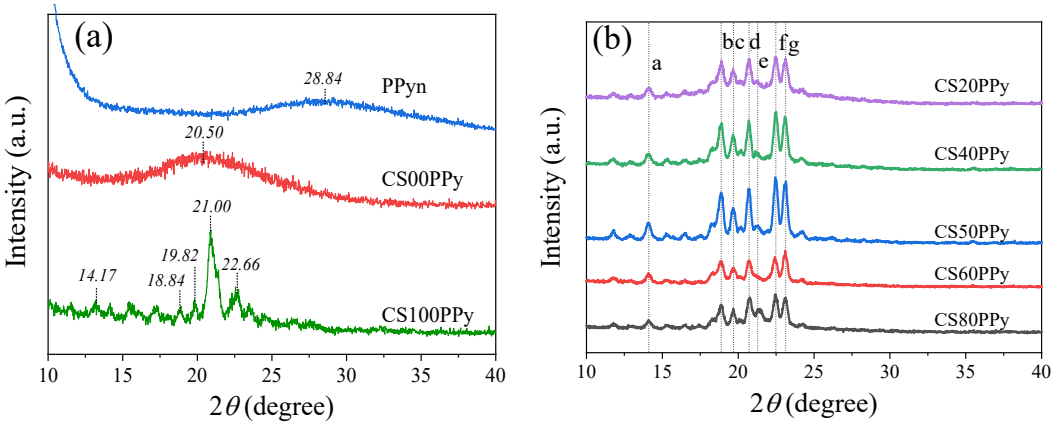

Figure 4-12. (a) XRD of PPyn, CS00PPy and CS100PPy and (b) XRD of PPy synthesis with different ratios of CTAB and SDS with peak location at a) 14.09, b) 18.85, c) 19.70, d) 20.70, e) 21.21, f) 22.48, and g) 23.10.

The results indicated that utilizing the CTAB-SDS system does not enhance the crystallinity of PPy samples. However, as the CTAB composition in the catanionic system increased, the electrical conductivity decreased from 0.530 S/m to 0.003 S/m (**Figure 4-9c**). A smaller average sample size was present along with this change, which was visible in SEM (**Figure 4-10**), consistent with the work in Chapter 2. That work showed that the resistance of PPy made with 0.10 M SDS decreased as the average size increased. Its resistance decreased from 0.73 GΩ to 43.58 Ω for PPy when the concentration of Py was between 0.03 M and 0.30 M, and the particle size increased from 102.50 nm to 604.50 nm.

Moreover, a higher concentration of SDS improved the electronic characteristics, as evidenced by a higher proportion of bipolaron to polaron structures in the Raman spectra. This finding indicated that the presence of CTAB and SDS in various molar ratios during Py polymerization leads to significant changes in the shape and properties of PPy, providing valuable insights into the material's structural and functional characteristics. The data evaluated in this work, including literature references, is shown in **Table 4-1**.

Table 4-1. Summary data from this work and previous works.

Sample ID	[CTAB]	[SDS]	Morphology from SEM	Size from DLS (nm)	Size from SEM	Conductivity (S/cm)	Ref.
-	10 mM	-	fiber	-	1 μm	1.11	Xing & Zhao, 2007*
	-	10 mM	agglomeration		-	-	
	10 mM	2 mM	nanofiber		500 nm	0.89	
	10 mM	4 mM	nanoparticles		∅=80 nm	0.50	
	10 mM	10 mM	agglomeration		∅=180 nm	1.49	
	4 mM	10 mM	agglomeration		-	8.51	
-	-	10 mM	large globules	-	-	-	Dubey et al., 2023*
	5 M	-	agglomeration			-	
	5 M	10 mM	globular			-	
CS00PPy	-	100 mM	sheet-like form/ flake-like shape	118.37	-	6.87E-03	This work **
CS20PPy	20 mM	80 mM	agglomeration	611.60	-	5.30E-03	
CS40PPy	40 mM	60 mM	disc-like shape	1701.25	-	3.40E-03	
CS50PPy	50 mM	50 mM	disc-like shape	746.04	-	2.82E-03	
CS60PPy	60 mM	40 mM	disc-like shape	613.63	-	5.36E-04	
CS80PPy	80 mM	20 mM	particles agglomeration	481.52	-	2.53E-05	
CS100PPy	100 mM	-	string-like shape	413.14	-	1.11E-04	

* [Py] = 0.05 M, [APS] = 0.05 M, conductivity received by four-probe method.

**[Py] = 0.10 M, [APS] = 0.10 M, conductivity received by two-probe method.

3.3. Possible role of molecule assembly by packing density during polymerization

As mentioned before, the agglomerated structure of PPy observed with SEM was more frequently encountered in polymerization with an additional SDS component due to electrostatic interactions between negatively charged SDS and positively charged PPy (Dubey, 2023a; Xing & Zhao, 2007). These electrostatic interactions at the head group may disrupt the packing of the acyl chain of SDS. This behaviour could significantly impact the acyl chain assembly of the catanionic surfactant. Our research suggests that investigating acyl chain packing density could provide deeper insights and validate these interactions.

During Py polymerization, the Raman spectra of the acyl chain region in the CTAB-SDS system were detected, as shown in **Figure 4-13**. The packing density was

then calculated. **Figure 4-14** compares the packing density of the CTAB-SDS system, dividing the results into three stages: (A) before adding the pyrrole monomer (Py), (B) after adding Py, and (C) after adding APS to initiate polymerization. Although the packing density decreased following the commencement of polymerization, there were slight differences in the packing density during polymerization across all assemblies. The packing density was monitored for 6 hours throughout the polymerization process. The results indicated that the arrangement of acyl chains in CS50PPy exhibited a similar pattern. Additionally, CS50PPy and CS60PPy exhibited higher packing density values than other conditions. For CS40PPy, the *R*-value fluctuated tendentiously during the 6 hours of polymerization and represented around 1.00 after the 23 hours of polymerization. This fluctuation phenomenon was like that of CS60PPy, which implied the variability of catanionic structure at these intermediate ratios. However, CS00PPy and CS20PPy did not find a peak at 2880 cm^{-1} during polymerization. Therefore, their packing density could not be determined. This finding suggests that the surfactant assembled in a disordered formation during Py polymerization in these systems.

In contrast, the samples with a greater concentration of cations, such as CS80PPy and CS100PPy, had a lower density of packed acyl chains than the others but still higher than that of CS00PPy. This finding suggests that the structures of CS80PPy and CS100PPy appeared more ordered than those of CS00PPy. This high-ordered structure was linked to a hydrophobic environment arising from the larger acyl chain present in CTAB, as opposed to SDS (Watanabe et al., 2022).

Our findings revealed that the packing density of the CTAB-SDS system during Py polymerization was related to the self-assembly behaviour of the CTAB-SDS system in the aqueous phase (Watanabe et al., 2022). Depending on the CTAB and SDS composition variations, the catanionic assembly can transform from a sphere micelle to a disc-like, vesicle or lamellar, which is associated with OD measurement and *R*-values. Notably, the cryo-TEM image of CS40Py (**Figure 4-5**) exhibited both disc-like and vesicle-like structures, along with a higher *R*-value compared to the state prior to pyrrole addition. Although the *R*-value of CS40PPy decreased slightly during polymerization, the cryo-TEM images indicated that solutions CS40, CS50, and CS60 might undergo a transition to disc-like configurations during this process. This suggests that upon polymerization occurring, these solutions could experience a shift towards disc-like

morphologies during polymerization. While the exact impact of the lyophilization process on the self-assembly structure remains uncertain, such a transition could ultimately lead to the formation of disc-shaped PPy structures, as observed in **Figure 4-10**.

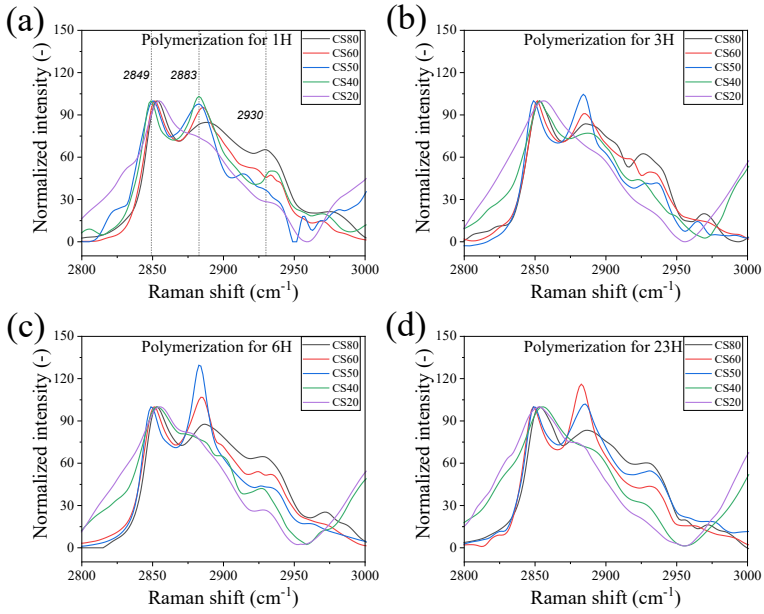

Figure 4-13. Raman spectra at the acyl chain area of Py polymerization in CTAB-SDS system at (a) 1 hour, (b) 3 hours, (c) 6 hours, and (d) 23 hours. All spectra were normalized by NGSLabSpec software of Raman spectroscopy with the peak at 2850 cm^{-1}.

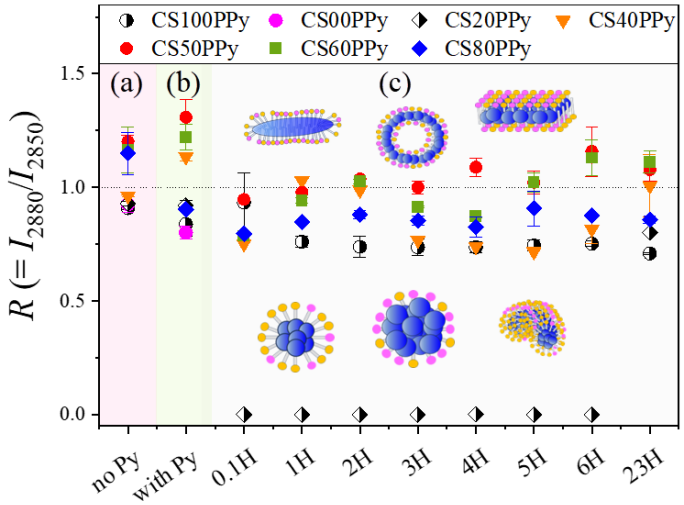

Figure 4-14. Packing density calculated from Raman spectra, comparing (a) before and (b) after adding Py monomer, and (c) during Py polymerization at various time intervals (0, 1, 2, 3, 4, 5, 6 and 23 hours).

Additionally, high packing density or highly ordered structures suggested a hydrophobic environment. In contrast, low packing density or disordered structures were found in micelle forms, indicating a hydrophilic environment (Suga et al., 2018). The association between packing density and the hydrophilic/hydrophobic environment was established by the combination results of Raman packing density analysis and fluorescence analysis in prior research (Watanabe et al., 2022; Xing & Zhao, 2007). The shape of PPy can be inferred from this association. For example, in the case of CS00PPy, the average size and PdI from DLS demonstrated good particle distribution. However, SEM images revealed a sheet-like morphology of PPy after freeze-drying. The disturbed arrangement in a disordered structure likely caused the form of this structure. This disruption created an environment that attracted water, which could result in a sheet-like or agglomerated structure after water removal by a freeze-dryer (Dubey, 2023a; Xing & Zhao, 2007). In contrast, CS100PPy likely had a more hydrophobic structure due to its higher R-value. According to DLS observations, this hydrophobicity lessened the effects of water loss during freeze-drying, allowing the PPy structure to remain at a nanoscale level as found in **Figure 4-7a** for DLS data and **Figure 4-10** for SEM.

The packing density results did not correspond with the electrical properties of PPy. However, understanding the arrangement of acyl chains may provide valuable knowledge about the hydrophobic/hydrophilic structure. We can use its information to evaluate the morphological characteristics of PPy or other materials.

4. Summary

This study demonstrated that the CTAB-SDS catanionic system significantly influenced the morphology and electronic properties of PPy synthesized during pyrrole polymerization. The size analysis from DLS and shape observation from SEM analyses revealed that the varying composition of CTAB and SDS resulted in varied particle sizes and morphologies; at the composition ratio close to 1:1, suddenly, a disc-like shape appeared. Raman spectroscopy showed that the bipolaron structure, indicative of enhanced conductivity, was prevalent in samples with higher SDS content. UV-Vis-NIR spectroscopy confirmed that the oxidative structure of PPy varied with the surfactant composition. When the composition of CTAB in catanionic surfactant increases,

absorbance at around 800 – 900 nm tends to be absent, indicating low conductivity. Moreover, this work established that the large size observed via SEM corresponded to higher electrical conductivity and decreased as size decreased with the mole fraction of CTAB in catanionic surfactant. The study found that the packing density of the CTAB-SDS system correlated with the resultant micelle formation. Furthermore, understanding the organization of acyl chains might yield valuable insights into the hydrophobic/hydrophilic architecture. The information may be utilized to assess the morphological properties of PPy following the drying process. By investigating the structural and electronic characteristics of PPy, this study has provided valuable information for designing conductive polymers using the catanionic system to tailor properties for various applications.

Chapter 5

Strategies and Case Studies for PPy Particles and Film Preparation

1. A strategy for Preparation of PPy Particles using Surfactant Self-Assembly

The preparation of PPy particles involves tailoring their morphology and conductivity by utilizing surfactant self-assembly templates. This strategy focuses on optimizing the synthesis conditions, such as the choice of surfactants (e.g., SDS, CTAB) and polymerization parameters (e.g., APS concentration). By controlling these factors, the author aims to achieve specific morphologies—such as sheet-like structures—known to enhance the electrical performance of PPy. The approach leverages the formation of bipolarons and polarons to improve conductivity, providing a pathway to advanced conductive materials as shown in **Scheme 5-1**.

A key aspect of this strategy is manipulating the surfactant composition and concentration to achieve desired PPy morphologies. For instance, SDS as a surfactant promoted the formation of sheet-like PPy structures, especially when polymerization was carried out with APS as the oxidant. The [Py]/[SDS] ratio played a crucial role; a higher ratio typically led to larger, more conductive sheet-like structures, while a lower ratio resulted in smaller, random forms with less conductivity. In contrast, using CTAB or a CTAB-SDS catanionic system allowed for further tuning of PPy morphology. CTAB micelles combined with APS often result in string-like or rod-shaped structures, especially at higher CTAB compositions. A near 1:1 ratio of CTAB to SDS can induce a disc-like morphology, which corresponded with specific electronic properties.

The choice of oxidant also significantly influences the final PPy structure. While APS is commonly used to enhance conductivity by forming bipolarons and polarons within the PPy matrix, other oxidants like $FeCl_3$ can yield different morphologies and electronic properties, depending on their interaction with the surfactant and monomer system. In summary, this strategy relies on the careful selection and manipulation of surfactant type, concentration, and polymerization conditions. By controlling these factors, researchers can tailor PPy's morphology and conductivity to meet the specific requirements of various applications.

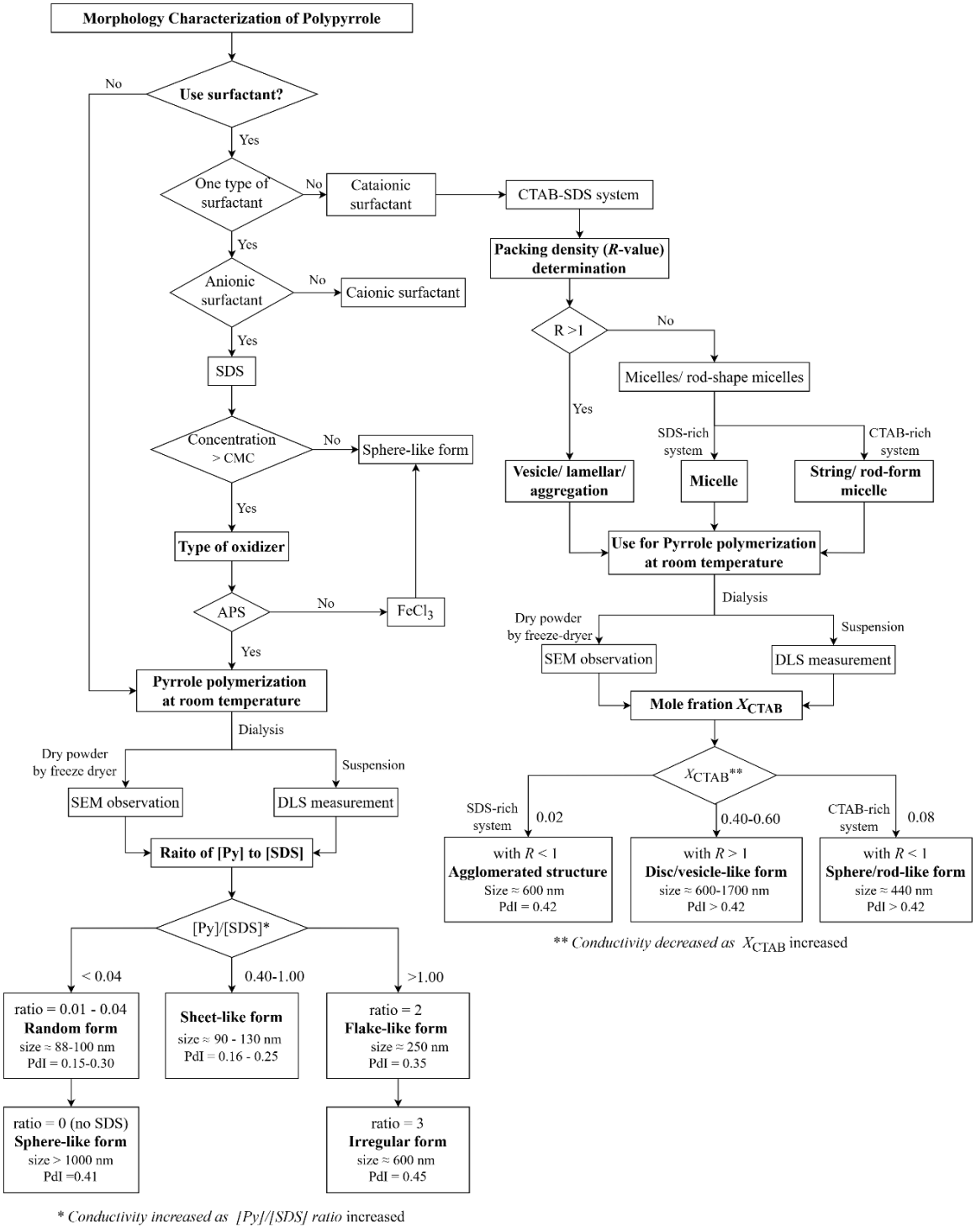

Scheme 5-1. Morphological development and characterization pathways of polypyrrole synthesized within a surfactant template.

2. Research Survey on PPy film Preparation

The preparation of PPy films from particles or powder is a crucial step in developing materials with tailored electrical properties for various applications, including sensors, batteries, and electronic devices. The method chosen for film preparation significantly influences the morphology and uniformity of the resulting PPy films. This overview compares several common techniques—each with its advantages and challenges. The following methods are briefly described: drop casting, Langmuir-Blodgett (LB) technique, spin coating, and dip coating.

2.1. Drop casting on electrode

Drop casting is a straightforward and widely used method for preparing PPy films from particles or powder. In this technique, a suspension of PPy particles in a suitable solvent, such as dimethylformamide (Kumar et al., 2022), chloroform (Arnaud et al., 2013) or m-cresol (Li et al., 2012), is prepared and then directly dropped onto an electrode surface. The solvent is allowed to evaporate, leaving behind a thin, uniform film of PPy. This method is particularly useful for fabricating sensors (Nagare et al., 2022; Šetka et al., 2019), where the PPy film serves as the active layer. Drop casting is simple and cost-effective, but it can result in non-uniform film thickness and poor adhesion if not carefully controlled. Several approaches have been explored to ameliorate the coffee ring effect, including using super-hydrophobic surfaces, electrowetting, anisotropic particles, in order to obtain a more uniform distribution of the drop casted nanoparticles across the electrode area (Kaliyaraj Selva Kumar et al., 2020).

2.2. Langmuir-Blodgett (LB) technique

The LB technique is a sophisticated method for preparing ultra-thin PPy films with controlled particle alignment. In this method, PPy particles or powder are dispersed in a solvent and spread onto a water surface in a Langmuir trough. The film formed at the air-water interface is then compressed to achieve a desired surface pressure and transferred onto a solid substrate, such as glass or an electrode, by vertical dipping as shown in **Figure 5-1** (Arai et al., 2019; Dhanabalan et al., 1998; Pandey et al., 2013). The LB technique is ideal for fabricating films with well-organized molecular structures and can be used to create multilayered films with precise control over thickness and alignment.

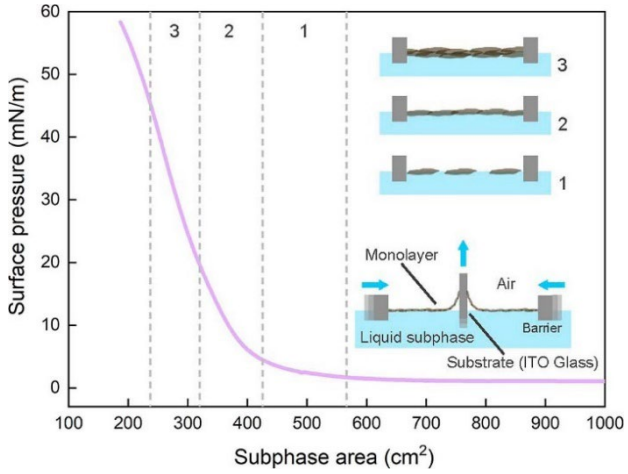

Figure 5-1. Example of surface pressure and subphase area plot corresponding to the formation of the LB assembly of graphene oxide onto ITO-coated glass (Devida et al., 2023).

2.3. Dip coating

Dip coating is a straightforward and scalable method for creating PPy films. In this process, a substrate is dipped into a solution or suspension of PPy particles and then withdrawn at a controlled speed. As the substrate is removed from the solution, a thin film of PPy is deposited onto its surface (Shinde et al., 2014). The thickness of the film can be controlled by adjusting the withdrawal speed, concentration of the suspension, and the number of dipping cycles. Dip coating is particularly useful for coating large or irregularly shaped substrates.

2.4. Spin coating

Spin coating is a technique commonly used to create uniform thin films from a suspension of PPy particles. In this method, the PPy suspension is deposited onto a substrate, which is then rapidly spun at high speed. The centrifugal force spreads the suspension evenly across the substrate, and the solvent evaporates, leaving a thin, uniform PPy film (Jayamurugan et al., 2015; Kumar et al., 2022). This method is particularly advantageous for creating films with controlled thickness, and it is widely used in the semiconductor and microelectronics industries.

The related work and a comparative summary of the advantages and disadvantages of each method are presented in **Table 5-1** and **Table 5-2**, respectively.

Table 5-1. Methods for film fabrication.

Method	Polymer Material	Solvent	Substrate	Condition	Thickness or Size	Ref.
Drop casting	$CH_3NH_3PbI_3$	DMF, 40wt%, (180–200 µl)	glass slides 4.4 cm^2	70–80 °C for 15–20 s	1.25–1.64 µm	Kumar et al., 2022
	Poly(3-hexylthiophene) (PHT), poly-quarterthiophene (PQT)	50 µl of 0.5 wt% polymer powders in dried chloroform	A mixture of ethylene glycol and glycerol was used for casting liquid substrate	leave the film for 5 min before transferred on a hydrophilic substrate	-	Arnaud et al., 2013
	PDPP-3T-Ref, PDPP-3T-Si	m-Xylene, 0.5 mg/mL	silicon substrate	evaporated 1 hour	40–90 nm (AFM)	H. Li et al., 2012
	PPy-PVA-$FeCl_3$	Ethanol	Silicon tile	80 °C for 30 min	Nanoparticle size 30-50 nm	Šetka et al., 2019
	PPy-$FeCl_3$, PPy-APS, PPy-H_2SO_4	m-Cresol, stirred for 2 days at room temperature	Glass substrate	Application for gas sensor	granular structures, 200–500 nm	Nagare et al., 2022
Langmuir-Blodgett (LB) technique	Poly (indole-5-carboxylic acid) (5CPIn)	DMSO,10 mg/ml, (then chloroform was added to make the mixture a ratio of 1: 10)	ITO glass	transferred at a surface pressure of 20 mN/m, the dipping speed of 3 mm/min	-	Pandey et al., 2013
	PPy-DBSA-APS	m-Cresol (then chloroform was added to make the mixture a ratio of 1:10)	BK7 glass, subphase was cadmium chloride.	transferred at a surface pressure of 25 mN/m with a dipping speed of 3 mm/min	-	Dhanabalan et al., 1998; Mello et al., 1999
	Graphene oxide (GO)	5:1water/ methanol solution, 0.15 mg/mL solution	ITO- glass	transferred at 15mN/m, with a dipping speed of 0.1mm/min	-	Devida et al., 2023
Dip coating	PPy-H_2SO_4 +APS/$FeCl_3$/PDC and	Water	stainless steel (SS) strips	successive ionic layer adsorption and reaction (SILAR) method	APS: wrinkled and homogeneous mud-like. $FeCl_3$: 100–400 nm PDC: 30–50 nm	Shinde et al., 2014
Spin coating	$CH_3NH_3PbI_3$	DMF (40wt%), (180–200 µl)	glass slides 4.4 cm^2	at 5000 rpm for 35 s	1.25–1.64 µm	Kumar et al., 2022
	Poly(3-hexylthiophene) (PHT), poly-quarterthiophene (PQT)	chloroform (0.5 wt%), 50 ml		at 3000–5000 rpm for 120 s	-	Kumar et al., 2022
	DBSA/PSS/ PPy composite	Water	glass slides	at 1000 rpm, 2000 rpm and 3000 rpm	378, 333, 304 nm	Jayamurugan et al., 2015

Table 5-2. A comparative summary of the advantages and disadvantages of each method for preparing films.

Methods	Advantages	Disadvantages
Drop casting	- Simple and cost-effective - Easy to perform with basic equipment	- May result in non-uniform film thickness - Poor adhesion and continuity if not carefully controlled
Langmuir-Blodgett (LB) technique	- Ability to create well-organized molecular structures - Precise control over film thickness and alignment	- Complex and time-consuming - Challenges in achieving continuous films - Requires optimization to improve adhesion
Spin coating	- Produces highly uniform thin films - Good control over film thickness - Fast and reproducible	- Limited to flat substrates - May result in edge effects or thickness gradients
Dip coating	- Simple and scalable - Suitable for large or irregularly shaped substrates - Controlled film thickness by varying withdrawal speed	- May lead to uneven film thickness if withdrawal speed is not uniform - Thickness control may be less precise than other methods - They are not as uniform

3. Case Study of PPy Film Preparation

This case study compared various methodologies for preparing PPy films, composed of (1) electrochemical polymerization, (2) drop-coating on electrodes from PPy powder prepared from chemical polymerization, and (3) using the Langmuir-Blodgett (LB) technique. This research aims to explore the efficiency of using PPy prepared by chemical polymerization in film preparation and evaluate it for its potential applications in chemiresistive sensors and other future electronic applications, with particular attention paid to surface morphology and conductivity.

3.1. Method

3.1.1. Method 1: PPy film fabrication by electrochemical polymerization

PPy film was polymerized by electrochemical polymerization method. Pyrrole monomer solution was added into 0.10 M SDS dissolving in ultrapure water to obtain Py monomer concentration of 0.10 M. Ultrapure water was used as solvent for all experiments. PPy film was formulated under voltage from -1.20 V to 1.20 V using cyclic voltammetry mode with different cycles for 1, 2, and 5 cycles, denoted as EP-1C EP-2C and EP-5C. Platinum rod and ITO glass were used as counter electrode (CE) and working electrode (WE), respectively. Pyrrole monomers were oxidized and deposited on WE electrode, which is cathode electrode. Reference electrode (RE) was Ag/AgCl electrode. After polymerization, PPy film coated on ITO glass was washed with ultrapure water to remove unreacted molecules, then dried at room temperature overnight then kept in desiccator until use. Surface morphology of PPy film was observed from SEM as shown in **Figure 5-2**.

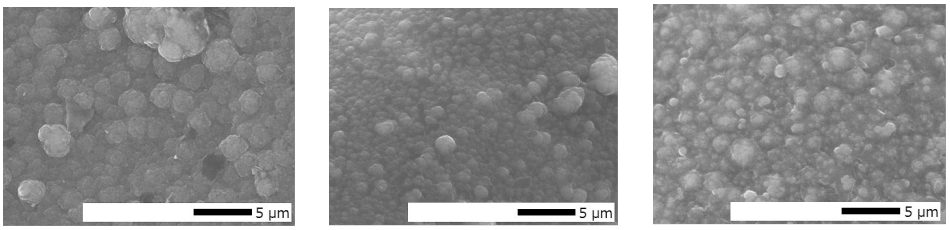

EP-1C EP-2C EP-5C

Figure 5-2. SEM image (at x5000 magnification) of PPy film prepared with SDS from electrochemical polymerization method.

3.1.2. Method 2: PPy film on glass using as chemiresistive electrode

PPy film was fabricated by drop-casting PPy suspensions onto glass sensor. PPy was synthesized via chemical polymerization method as described in previous. PSF and PCA were samples from Chapter 3, which were prepared with SDS as template and $FeCl_3$ as oxidizer, and CTAB as template and APS as oxidizer, respectively. The summary of sample used is represented in the **Table 5-3**. The procedure of film preparation is shown in **Scheme 5-2**.

Table 5-3. Sample abbreviations and compositions.

Sample	[Py], M	[SDS], M	[CTAB], M	[APS], M	[$FeCl_3$], M	Size (nm)±SD	PdI±SD	Zeta potential (mV) ±SD
PSA	0.1	0.1	-	0.1		118.4±1.40	0.23±0.06	-26.7
PSF	0.1	0.1	-	-	0.1	1369.0±126.6	0.54±0.07	-19
PCA	0.1	-	0.1	0.1		289.2±3.43	0.26±0.002	23.2
no surfactant	0.1	-	-	0.1	-	2506±604.00	0.63±0.23	25.60
EP-5C	0.1	0.1	-	-	-	-	-	-

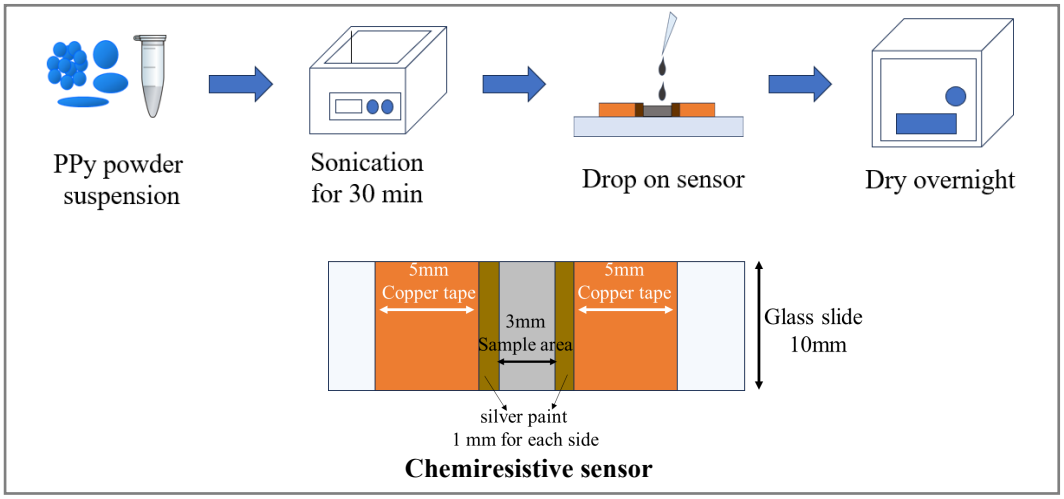

Scheme 5-2. Illustration of film preparation by drop casting on chemiresistive sensor.

3.1.3. Method 3: LB technique

For Langmuir films, the π-*A* isotherms or surface pressure-area isotherms of PPy powder were conducted using a Langmuir trough KSV 2000 equipped with a Wilhelmy plate, symmetrical compression barriers, and water subphase with the temperature at 25 ^{o}C. The barriers were set at a speed of 10 mm/min. The weight of the sample was varied and dispersed in chloroform before it was dropped on water subphase. The layer LB films were transferred onto a glass slide or ITO electrode with a constant surface pressure of 30 mN/m. The vertical dipping method was used with a dipping speed varying from 4 mm/min (Antunes et al., 2005).

Controlled particle alignment using the LB technique faced significant challenges. PPy particles dispersed in chloroform were transferred onto glass or ITO substrates, but they formed disconnected structures, leading to poor film adhesion and continuity. Although the surface pressure–molecular area (π–A) isotherm indicated particle condensation, as found in **Figure 5-3**, the films remained poorly aligned. This indicates that further optimization of the LB method is necessary to achieve continuous and well-aligned PPy films.

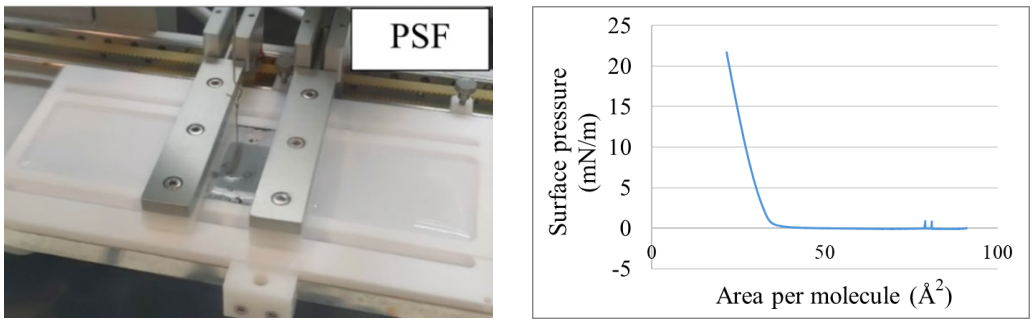

Figure 5-3. π-A isotherms of Langmuir films from PPy powder added to the ultrapure water subphase and PPy behaviour on subphase.

3.2. Electrical properties

3.2.1. Resistance by multimeter

The PPy film after prepared from method 1 and method 2 were analysed for resistance by multimeter, the analysis system is shown in **Figure 5-4a**. The results showed that chemically polymerized films exhibited improved conductivity as sample weight increased from 0.30 mg to 0.50 mg, with the PSF sample showing the lowest resistance at 0.50 mg (**Table 5-4**). In contrast, electrochemically polymerized films exhibited increasing resistance with more cycles and sample weight. The results suggested that structural variations or packing density of particles might affect conductivity in these films as observed from SEM, as shown in **Figure 5-5**.

3.2.2. Electrochemical performance by Automatic polarization system

Cyclic voltammetry (CV) was employed to investigate the redox behaviour of a PPy-based chemiresistive sensor, with phosphate buffer solution (PBS) (pH 6.8) applied

directly to the sensor. The sensor was connected to Automatic polarization system to perform CV measurements, as illustrated in **Figure 5-4b**. The CV results, shown in **Figure 5-6**, indicated that the EP-5C sample exhibited the highest sensitivity at 25 °C compared to other types of PPy, with the PSF film following closely. Notably, among PPy samples prepared by chemical polymerization, the PSF sample demonstrated superior sensitivity. This enhanced performance can be attributed to its particle characteristics, including optimized morphology, uniform surface coating, and improved conductivity. Additionally, the remaining ferric element in PPy might be a reason for improving its conductivity of PSF. These findings underscore the importance of refining PPy particle attributes to enhance sensor performance in pH-sensitive applications.

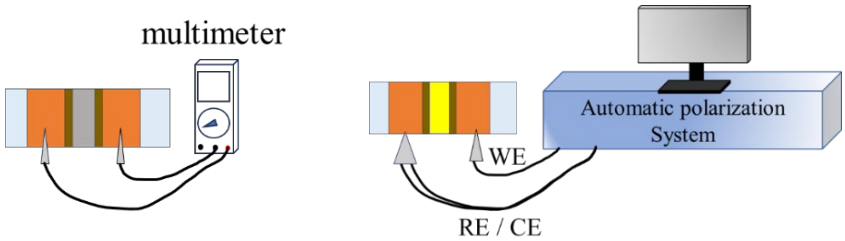

Figure 5-4. (a) Resistance measurement by multimeter and (b) electrochemical performance by Automatic polarization system.

Table 5-4. Resistance of PPy-sensor measured from multimeter.

Sample	Weight (mg)	Average resistance (Ohm) by multimeter (n=3)
PSA	0.3	x
PSF	0.3	1.50E+01
PCA	0.3	1.84E+07
EP-2C	0.3	8.60E+00
no surfactant	0.3	x
PSA	0.5	x
PSF	0.5	8.00E+00
PCA	0.5	1.21E+07
EP-5C	0.4	1.46E+01
no surfactant	0.5	6.43E+06

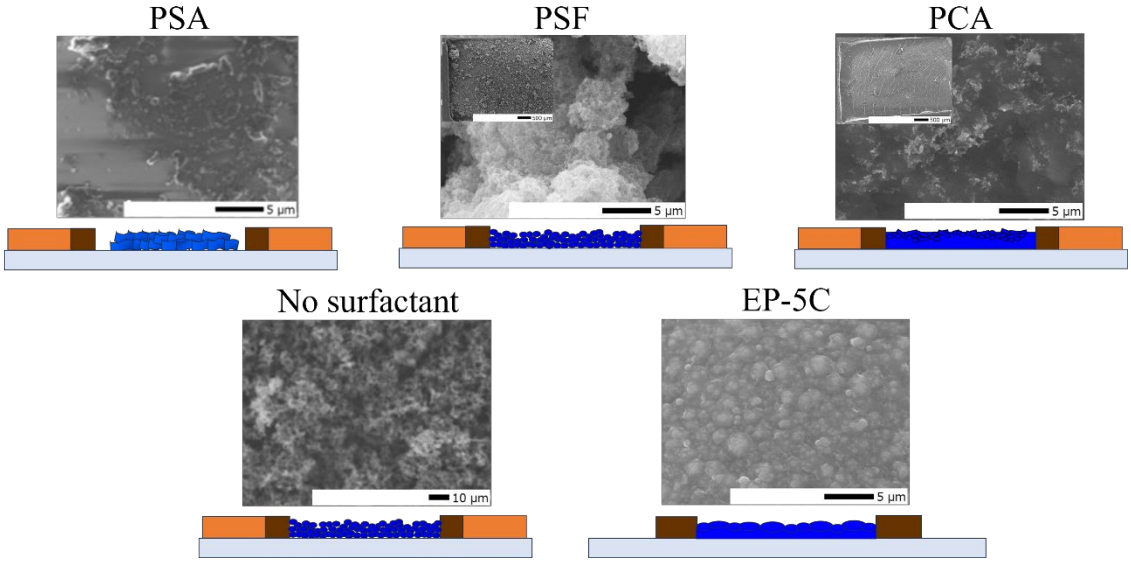

Figure 5-5. SEM image and graphic illustration of chemiresistive sensor.

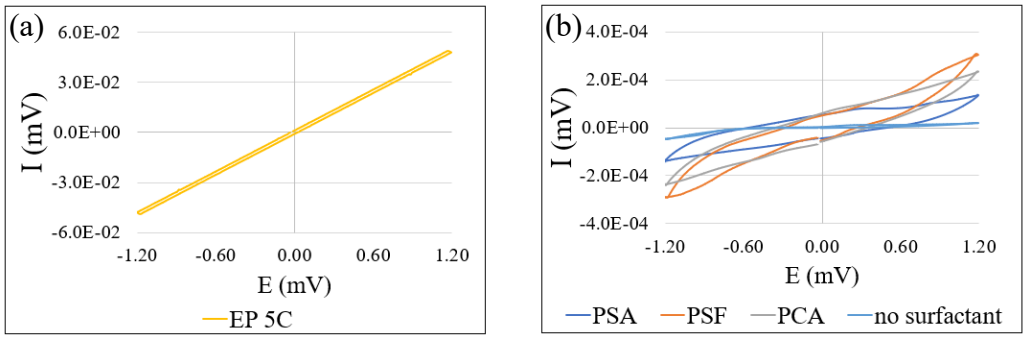

Figure 5-6. CV scans of PPy-coated electrodes in phosphate buffer solution (PBS, pH 6.8) at a scan rate of 100 mV/s: (a) EP-5C, and (b) comparing between PSA, PSF, PCA and no surfactant.

3.3. Conclusion

The case study highlighted substantial challenges in employing the LB approach to fabricate PPy films, notably regulated particle alignment, which resulted in poor film adhesion and continuity. The results showed that additional refining of the LB technique is required to generate continuous and aligned PPy films. Despite these challenges, the work demonstrated the potential of using PPy synthesized with SDS as a template and $FeCl_3$ as an oxidant to create a chemiresistive sensor by drop casting, with better

conductivity as sample weight increased. Furthermore, cyclic voltammetry demonstrated that the PSF sample was the most responsive in a pH-sensitive chemiresistive sensor when compared to other types of PPy prepared with the same chemical polymerization method. It stresses the significance of PPy produced with optimal surfactants and oxidants, which enables us to adjust sensor performance to the specific application.

4. Summary

This chapter outlined the synthesis pathway for PPy with diverse morphologies using surfactant template assistance. It provided guidelines for producing PPy nanostructures with specific properties tailored to various applications. The author also surveyed methods for film fabrication, including drop casting, LB technique, spin coating, and dip coating. Each method presented distinct advantages and challenges, significantly influencing the uniformity, thickness, and overall quality of the resulting PPy films, as demonstrated in the case study.

The case study focused on the challenges faced with the LB method, which resulted in poor film adhesion and continuity. Despite these obstacles, the LB technique has the potential to produce well-organized molecular structures; nonetheless, additional tuning is required. On the other hand, PPy films created by drop casting performed better and were more conductive, particularly in chemiresistive sensor applications. An experiment within the case study concluded that, while traditional methods such as electrochemical polymerization yield good electrical properties, PPy synthesized with surfactant templates—especially when optimized with precise polymerization parameters—provides enhanced control over the final morphology and electrical properties of PPy particles effecting on film properties. These approaches are particularly advantageous for advanced applications requiring high conductivity and specific structural characteristics.

Chapter 6

General Conclusion

Chapter 1 introduced Py, an organic compound serving as the monomer for PPy, a conductive polymer known for its exceptional electrical properties. Py is a five-membered aromatic heterocycle (C_4H_5N), and its polymerization into PPy results in a conjugated backbone that enables π-electron delocalization, crucial for conductivity. The chapter reviewed the synthesis of PPy through electrochemical or chemical polymerization, where oxidative coupling of Py unit's forms conjugated chains. The resulting PPy's electrical conductivity, influenced by its optical band gap and synthesis conditions, makes it valuable in applications like biomaterials, biosensors, and energy storage, due to its stability, biocompatibility, and efficient charge transfer capabilities.

Chapter 2 investigated the role of SDS in the chemical polymerization of PPy and its impact on PPy's physical, electrical, and chemical properties. SDS acted as a template, guiding the polymerization within its micellar structure, transforming PPy morphologies from random to sheet-like forms as Py concentration and APS/Py ratio increase. In contrast, PPy synthesized without SDS (PPy*) formed only sphere-like structures. SDS significantly enhanced PPy's conductivity and altered its optical band gap, particularly increasing the ratio of bipolarons to polarons. The study revealed a strong relationship between SDS concentration, PPy's average size, morphology, and electrical properties, emphasizing SDS's crucial role in tailoring PPy's characteristics for specific applications.

Chapter 3 examined the impact of different surfactants and oxidants on the morphology, electronic properties, and bipolaron/polaron ratios of PPy. The study compared PPy synthesized with SDS, CTAB, and Tween 80 as surfactants, revealing that SDS led to a sheet-like morphology and higher bipolaron and polaron ratios in the C–H deformation region, enhancing electronic properties. In contrast, PPy synthesized with SDS and iron as the oxidant (Py-SDS-Fe) formed particle-like clusters but exhibits higher conductivity and bipolaron/polaron ratio compared to Py-CTAB-Fe. The findings emphasized that while morphology may vary, the bipolaron/polaron ratio strongly corresponded with conductivity, with SDS playing a key role in enhancing bipolaron content and overall conductivity through electrostatic interactions.

Chapter 4 examined the impact of the CTAB-SDS catanionic system on PPy morphology and electronic properties during pyrrole polymerization. DLS and SEM analyses showed that varying CTAB and SDS ratios produced different particle sizes and morphologies, with a disc-like shape at a near 1:1 ratio. Higher SDS content favoured bipolaron structures, enhancing conductivity, while increasing CTAB content reduced it, as indicated by UV-Vis-NIR spectroscopy. The study found that larger particle sizes, associated with catanionic assembly, corresponded to higher conductivity, offering valuable insights for designing conductive polymers using catanionic surfactant systems. Additionally, analysis of packing density revealed that acyl chain arrangement and the balance between hydrophobic and hydrophilic environments influenced the dry morphology of PPy, particularly as chemical composition variables, such as Py concentration (as discussed in Chapter 2) or surfactant type (as examined in Chapter 3 and this chapter), were adjusted.

The studies discussed above highlighted the impact of various surfactants on the electrical conductivity and morphology of PPy. By incorporating different surfactant systems into pyrrole polymerization, the properties of PPy particles can be effectively tailored. In the next chapter, a case study involving the fabrication of PPy films on substrates was conducted to evaluate how the properties of PPy particles influence the overall film characteristics.

Chapter 5 presented a comprehensive strategy for preparing PPy particles with optimized morphology and conductivity by leveraging surfactant self-assembly. This approach used surfactants like SDS and CTAB, along with controlled polymerization techniques, to create specific structures, such as sheet-like forms that significantly enhance electrical performance. The chapter also reviewed various PPy film preparation methods, including chemical polymerization, electrochemical polymerization, and the LB technique, examining their impact on film packing, particle organization, and conductivity. A comparative case study on electrical performance concluded that, although traditional techniques offer thickness scalability, the surfactant-templated approach allows for superior control over morphology and electrical properties, making it suited for various applications.

Suggestions for Future Works

Based on the conclusions from each chapter of my research, here are two suggestions for future work that could further advance the study of PPy and its applications:

1. Optimization of Surfactant Systems for Enhanced Electrical Conductivity and Morphology Control

The research has demonstrated that surfactants like SDS, CTAB, and their combinations significantly influence the morphology and electrical properties of PPy. However, further exploration is needed to optimize these surfactant systems for even greater control over PPy's properties.

- **Investigation of new surfactant combinations**: Future studies could explore a broader range of surfactant combinations, including non-ionic and zwitterionic surfactants, to understand how these variations impact PPy morphology and conductivity. By systematically varying the surfactant type and concentration, researchers can identify optimal conditions for producing PPy with specific properties tailored for advanced electronic applications.
- **Mechanistic studies on surfactant-polymer interactions**: A deeper understanding of the molecular interactions between surfactants and PPy during polymerization could be achieved through advanced characterization techniques, such as in situ spectroscopy or molecular dynamics simulations. This could provide insights into the formation of bipolaron and polaron structures and how these influence the overall conductivity of the material.
- **Scaling up the polymerization** Process: Research could also focus on scaling up the optimized surfactant-polymer systems for industrial applications. This would involve addressing challenges such as maintaining uniformity and conductivity in larger-scale productions while ensuring that the material properties meet the required standards for commercial use.

2. Exploration of Substrate Fabrication Techniques and Applications in Advanced Devices

The case study involving PPy film fabrication on substrates highlights the potential for tailoring film properties based on the characteristics of the underlying PPy particles. Future work could expand on this by exploring advanced fabrication techniques and their applications in various devices.

- **Development of novel fabrication techniques**: Research could investigate advanced fabrication methods such as inkjet printing, electrospinning, or LB technique to create PPy films with precise control over thickness, uniformity, and orientation. These methods could be optimized to enhance the integration of PPy films into flexible electronics, sensors, or energy storage devices.
- **Application in next-generation electronic devices**: The unique properties of PPy films, such as high conductivity and tailored morphologies, could be leveraged in the development of next-generation electronic devices. Future studies could focus on integrating these films into wearable electronics, bioelectronics, or active layers in organic solar cells. Additionally, exploring the biocompatibility and environmental stability of PPy films could open up new avenues for their use in medical devices or environmentally sustainable technologies.
- **Evaluation of long-term stability and performance**: Future work should also consider the long-term stability and performance of PPy films in real-world applications. This would involve testing the films under various environmental conditions, such as humidity, temperature fluctuations, and mechanical stress, to ensure their reliability and durability in practical applications.

These two areas of focus—optimizing surfactant systems and exploring advanced fabrication techniques—provide a clear pathway for future research to build on the findings of my study. By addressing these topics, researchers can further enhance the performance and applicability of PPy in various fields, from electronics to energy storage.

Nomenclatures

P	=	Packing parameter
V	=	Volume of the hydrophobic tail
a_0	=	Area of the hydrophilic head
l_c	=	Length of the hydrophobic tail
α	=	The absorption coefficient
A	=	Light absorbance
d	=	Cell thickness (path length of cuvette cell)
hv	=	Photon energy
h	=	Planck's constant (6.6261×10^{-34} J·s)
v	=	Photon frequency
C	=	Speed of light (2.998×10^{8} m/s)
λ	=	Wavelength
E_g	=	Optical band gap or band gap
Ω	=	Ohm (unit of resistance)
α_o	=	Constant band-tailing parameter
n	=	Power factor
I	=	Current
V	=	Potential
R	=	Resistance
ρ	=	Resistivity
L	=	Thickness of silicon rubber
A	=	Area of the sample (for resistance calculation)
Log P	=	Octanol-water partition coefficient
ζ	=	Zeta potential
R-value	=	Packing density of acyl chain

List of Abbreviations

APS	=	Ammonium persulfate
B/P ratio	=	Bipolaron to Polaron Ratio
C–C	=	Carbon-Carbon bonding
CE	=	Counter electrode
C–H	=	Carbon-Hydrogen bonding
CMC	=	Critical micelle concentration
CTAB	=	Cetyltrimethylammonium bromide
CV	=	Cyclic voltammetry
DLS	=	Dynamic light scattering
EDS	=	Energy Dispersive X-ray Spectroscopy
ELS	=	Electrophoretic light scattering
Fe	=	Ferric chloride
ITO	=	Indium tin oxide
LSV	=	Linear sweep voltammetry
LB	=	Langmuir-Blodgett
OD	=	Optical density
PBS	=	Phosphate buffer solution
PCA	=	Polypyrrole sample with CTAB and APS
PdI	=	Polydispersity Index
PSA	=	Polypyrrole sample with SDS and APS
PSF	=	Polypyrrole sample with SDS and $FeCl_3$
PPy	=	Polypyrrole
Py	=	Pyrrole
RE	=	Reference electrode
Ref	=	Reference
RT	=	Room temperature
SDS	=	Sodium dodecyl sulfate
SEM	=	Scanning Electron Microscopy
TW, TW80	=	Tween 80
UV-Vis-NIR	=	Ultraviolet-Visible-Near Infrared
WE	=	Working electrode
XRD	=	X-ray Diffraction

References

Alekseeva, E., Bober, P., Trchová, M., Šeděnková, I., Prokeš, J., & Stejskal, J. The composites of silver with globular or nanotubular polypyrrole: The control of silver content. *Synthetic Metals*, **2015**, *209*, 105–111.

Antony, M. J., & Jayakannan, M. Amphiphilic Azobenzenesulfonic Acid Anionic Surfactant for Water-Soluble, Ordered, and Luminescent Polypyrrole Nanospheres. *The Journal of Physical Chemistry B*, **2007**, *111*(44), 12772–12780.

Antunes, P. A., Santana, C. M., Aroca, R. F., Oliveira, O. N., Constantino, C. J. L., & Riul, A. The use of Langmuir–Blodgett films of a perylene derivative and polypyrrole in the detection of trace levels of Cu2+ ions. *Synthetic Metals*, **2005**, *148*(1), 21–24.

Appel, G., Böhme, O., Mikalo, R., & Schmeißer, D. The polaron and bipolaron contributions to the electronic structure of polypyrrole films. *Chemical Physics Letters*, **1999**, *313*(3–4), 411–415.

Arai, N., Watanabe, S., & Miyahara, M. T. On the Convective Self-Assembly of Colloidal Particles in Nanofluid Based on in Situ Measurements of Interaction Forces. *Langmuir*, **2019**, *35*(35), 11533–11541.

Arnaud, D., Pandey, R. K., Miyajima, S., Nagamatsu, S., Prakash, R., Takashima, W., Hayase, S., & Kaneto, K. Fabrication of Large-scale Drop-cast Films of π-conjugated Polymers with Floating-film Transfer Method. *Transactions of the Materials Research Society of Japan*, **2013**, *38*(2), 305–308.

Ashery, A., Salem, M. A., & Farag, A. A. M. Optical and electrical performance of ploypyrrol thin films and its hybrid junction applications. *Optik*, **2018**, *172*, 302–310.

Atta, A., Negm, H., Abdeltwab, E., Rabia, M., & Abdelhamied, M. M. Facile fabrication of polypyrrole/NiOx core-shell nanocomposites for hydrogen production from wastewater. *Polymers for Advanced Technologies*, **2023**, *34*(5), 1633–1641.

Balint, R., Cassidy, N. J., & Cartmell, S. H. Conductive polymers: Towards a smart biomaterial for tissue engineering. *Acta Biomaterialia*, **2014**, *10*(6), 2341–2353.

Bayat, M., Izadan, H., Santiago, S., Estrany, F., Dinari, M., Semnani, D., Alemán, C., & Guirado, G. Study on the electrochromic properties of polypyrrole layers doped with different dye molecules. *Journal of Electroanalytical Chemistry*, **2021**, *886*, 115113.

Benramache, S., Belahssen, O., Guettaf, A., & Arif, A. Correlation between electrical conductivity—Optical band gap energy and precursor molarities ultrasonic spray deposition of ZnO thin films. *Journal of Semiconductors*, **2013**, *34*(11), 113001.

Bo, J., Luo, X., Huang, H., Li, L., Lai, W., & Yu, X. Morphology-controlled fabrication of polypyrrole hydrogel for solid-state supercapacitor. *Journal of Power Sources*, **2018**, *407*, 105–111.

Bober, P., Li, Y., Acharya, U., Panthi, Y., Pfleger, J., Humpolíček, P., Trchová, M., & Stejskal, J. Acid Blue dyes in polypyrrole synthesis: The control of polymer morphology at nanoscale in the promotion of high conductivity and the reduction of cytotoxicity. *Synthetic Metals*, **2018**, *237*, 40–49.

Brédas, J. L., Scott, J. C., Yakushi, K., & Street, G. B. Polarons and bipolarons in polypyrrole: Evolution of the band structure and optical spectrum upon doping. *Physical Review B*, **1984**, *30*(2), 1023–1025.

Brusamarello, C. Z., Santos, L. M., Romio, A. P., Domenico, M. D., Santos, A. F., de Araújo, P. H. H., & Sayer, C. Polypyrrole production through chemical polymerization using anionic and cationic dopants: The influence of synthesis conditions and reaction kinetics. *Materials Today Communications*, **2021**, *26*, 101740.

Chitte, H. K., Shinde, G. N., Bhat, N. V., & Walunj, V. E. Synthesis of Polypyrrole Using Ferric Chloride (FeCl₃) as Oxidant Together with Some Dopants for Use in Gas Sensors. *Journal of Sensor Technology*, **2011**, *01*(02), 47–56.

Choudhury, B., & Choudhury, A. Dopant induced changes in structural and optical properties of Cr3+ doped TiO2 nanoparticles. *Materials Chemistry and Physics*, **2012**, *132*(2–3), 1112–1118.

Dai, T., Yang, X., & Lu, Y. Controlled growth of polypyrrole nanotubule/wire in the presence of a cationic surfactant. *Nanotechnology*, **2006**, *17*(12), 3028–3034.

Danaei, M., Dehghankhold, M., Ataei, S., Hasanzadeh Davarani, F., Javanmard, R., Dokhani, A., Khorasani, S., & Mozafari, M. R. Impact of Particle Size and Polydispersity Index on the Clinical Applications of Lipidic Nanocarrier Systems. *Pharmaceutics*, **2018**, *10*(2), 57.

Das, I., Goel, N., Agrawal, N. R., & Gupta, S. K. Growth Patterns of Dendrimers and Electric Potential Oscillations during Electropolymerization of Pyrrole using Mono- and Mixed Surfactants. *The Journal of Physical Chemistry B*, **2010**, *114*(40), 12888–12896.

De Aguiar, M. F., Leal, A. N. R., De Melo, C. P., & Alves, K. G. B. Polypyrrole-coated electrospun polystyrene films as humidity sensors. *Talanta*, **2021**, *234*, 122636.

Deljoo Kojabad, Z., & Shojaosadati, S. A. Chemical synthesis of polypyrrole nanostructures: Optimization and applications for neural microelectrodes. *Materials & Design*, **2016**, *96*, 378–384.

Devida, J. M., Herrera, F., Daza Millone, M. A., Requejo, F. G., & Pallarola, D. Electrochemical Fine-Tuning of the Chemoresponsiveness of Langmuir–Blodgett Graphene Oxide Films. *ACS Omega*, **2023**, *8*(30), 27566–27575.

Dhanabalan, A., Mello, S. V., & Oliveira, O. N. Preparation of Langmuir−Blodgett Films of Soluble Polypyrrole. *Macromolecules*, **1998**, *31*(6), 1827–1832.

Direksilp, C., & Sirivat, A. Synthesis and Characterization of Hollow-Sphered Poly(N-methyaniline) for Enhanced Electrical Conductivity Based on the Anionic Surfactant Templates and Doping. *Polymers*, **2020**, *12*(5), 1023.

Dubey, N. A study on surfactant modified polypyrrole nanostructures and its applications in supercapacitors. *International Journal of Polymer Analysis and Characterization*, **2023**, *28*(6), 625–646.

Dubey, N. Chemical Synthesis and Characterization of Polyaniline-g-Cellulose Biocomposites in the Presence of Surfactants and Their Applications in pH Sensors. *Chemistry Africa*, **2023**, *6*(1), 205–220.

Dutta Gupta, N., Banerjee, D., Das, N. S., & Chattopadhyay, K. K. Kinetics of micelle formation and their effect on the optical and structural properties of polypyrrole nanoparticles. *Colloids and Surfaces A: Physicochemical and Engineering Aspects*, **2011**, *385*(1), 55–62.

Fan, X., Yang, Z., & He, N. Hierarchical nanostructured polypyrrole/graphene composites as supercapacitor electrode. *RSC Advances*, **2015**, *5*(20), 15096–15102.

Fernández-Peña, L., Abelenda-Nuñez, I., Hernández-Rivas, M., Ortega, F., Rubio, R. G., & Guzmán, E. Impact of the bulk aggregation on the adsorption of oppositely charged polyelectrolyte-surfactant mixtures onto solid surfaces. *Advances in Colloid and Interface Science*, **2020**, *282*, 102203.

Gangopadhyay, R. Peering into polypyrrole-SDS nanodispersions: Rheological view. *Journal of Applied Polymer Science*, **2012**, 1398–1408.

George, P. M., Lyckman, A. W., LaVan, D. A., Hegde, A., Leung, Y., Avasare, R., Testa, C., Alexander, P. M., Langer, R., & Sur, M. Fabrication and biocompatibility of polypyrrole implants suitable for neural prosthetics. *Biomaterials*, **2005**, *26*(17), 3511–3519.

Gopi, D., Kavitha, L., Ramya, S., & Rajeswari, D. Chapter 15—Chemical and green routes for the synthesis of multifunctional pure and substituted nanohydroxyapatite for biomedical applications. In A. M. Grumezescu (Ed.), *Engineering of Nanobiomaterials* (pp. 485–521). **2016**. William Andrew Publishing.

Guan, H., Ding, T., Zhou, W., Wang, Z., Zhang, J., & Cai, K. Hexagonal polypyrrole nanosheets from interface driven heterogeneous hybridization and self-assembly for photothermal cancer treatment. *Chemical Communications*, **2019**, *55*(30), 4359–4362.

Gupta, S. Hydrogen bubble-assisted syntheses of polypyrrole micro/nanostructures using electrochemistry: Structural and physical property characterization. *Journal of Raman Spectroscopy*, **2008**, *39*(10), 1343–1355.

Han, J., Suga, K., Hayashi, K., Okamoto, Y., & Umakoshi, H. Multi-Level Characterization of the Membrane Properties of Resveratrol-Incorporated Liposomes. *The Journal of Physical Chemistry B*, **2017**, *121*(16), 4091–4098.

Han, X., Xiao, G., Wang, Y., Chen, X., Duan, G., Wu, Y., Gong, X., & Wang, H. Design and fabrication of conductive polymer hydrogels and their applications in flexible supercapacitors. *Journal of Materials Chemistry A*, **2020**, *8*(44), 23059–23095.

Hazarika, J., & Kumar, A. Controllable synthesis and characterization of polypyrrole nanoparticles in sodium dodecylsulphate (SDS) micellar solutions. *Synthetic Metals*, **2013**, *175*, 155–162.

He, C., Yang, C., & Li, Y. Chemical synthesis of coral-like nanowires and nanowire networks of conducting polypyrrole. *Synthetic Metals*, **2003**, *139*(2), 539–545.

Hong, J., Dong, Z., Chen, X., Chen, W., Li, D., Yu, F., & Chen, Y. α–α Coupling-Dominated PPy Film with a Well-Conjugated Structure for Superlong Cycle Life Supercapacitors. *ACS Applied Materials & Interfaces*, **2024**, *16*(6), 7806–7818.

Hoshina, Y., Zaragoza-Contreras, E. A., Farnood, R., & Kobayashi, T. Nanosized polypyrrole affected by surfactant agitation for emulsion polymerization. *Polymer Bulletin*, **2012**, *68*(6), 1689–1705.

Hou, Y., Zhang, L., Chen, L. Y., Liu, P., Hirata, A., & Chen, M. W. Raman characterization of pseudocapacitive behavior of polypyrrole on nanoporous gold. *Physical Chemistry Chemical Physics*, **2014**, *16*(8), 3523.

Ishpal, & Kaur, A. Spectroscopic and electrical sensing mechanism in oxidant-mediated polypyrrole nanofibers/nanoparticles for ammonia gas. *Journal of Nanoparticle Research*, **2013**, *15*(5), 1637.

Israelachvili, J. N. *Intermolecular and Surface Forces* (3rd ed.). **2011**. Elsevier Inc.

Iurchenkova, A. A., Kallio, T., & Fedorovskaya, E. O. Relationships between polypyrrole synthesis conditions, its morphology and electronic structure with supercapacitor properties measured in electrolytes with different ions and pH values. *Electrochimica Acta*, **2021**, *391*, 138892.

Izza, N., Suga, K., Okamoto, Y., Watanabe, N., Bui, T. T., Wibisono, Y., Fadila, C. R., & Umakoshi, H. Systematic Characterization of Nanostructured Lipid Carriers from Cetyl Palmitate/Caprylic Triglyceride/Tween 80 Mixtures in an Aqueous Environment. *Langmuir*, **2021**, *37*(14), 4284–4293.

Jamdegni, M., & Kaur, A. Role of polarity of surfactants on the morphology of electrochemically synthesized polyaniline nanostructures: Towards faster and efficient electrochromic response. *Thin Solid Films*, **2020**, *714*, 138373.

Jayamurugan, P., Ponnuswamy, V., Subba Rao, Y. V., Ashokan, S., & Meenakshisundar, S. Influence of spin coating rate on the thickness, surface modification and optical properties of water dispersed PPy composite thin films. *Materials Science in Semiconductor Processing*, **2015**, *39*, 205–210.

Jeeju, P. P., Varma, S. J., Francis Xavier, P. A., Sajimol, A. M., & Jayalekshmi, S. Novel polypyrrole films with excellent crystallinity and good thermal stability. *Materials Chemistry and Physics*, **2012**, *134*(2–3), 803–808.

Johansson, E., Sandström, M. C., Bergström, M., & Edwards, K. On the Formation of Discoidal versus Threadlike Micelles in Dilute Aqueous Surfactant/Lipid Systems. *Langmuir*, **2008**, *24*(5), 1731–1739.

Jubu, P. R., Obaseki, O. S., Nathan-Abutu, A., Yam, F. K., Yusof, Y., & Ochang, M. B. Dispensability of the conventional Tauc's plot for accurate bandgap determination from UV–vis optical diffuse reflectance data. *Results in Optics*, **2022**, *9*, 100273.

Jurašin, D. D., Šegota, S., Čadež, V., Sikirć, A. S. and M. D., Jurašin, D. D., Šegota, S., Čadež, V., & Sikirć, A. S. and M. D. Recent Advances in Catanionic Mixtures. In *Application and Characterization of Surfactants*. **2017**. IntechOpen.

Kaliyaraj Selva Kumar, A., Zhang, Y., Li, D., & Compton, R. G. A mini-review: How reliable is the drop casting technique? *Electrochemistry Communications*, **2020**, *121*, 106867.

Kausaite-Minkstimiene, A., Mazeiko, V., Ramanaviciene, A., & Ramanavicius, A. Evaluation of chemical synthesis of polypyrrole particles. *Colloids and Surfaces A: Physicochemical and Engineering Aspects*, **2015**, *483*, 224–231.

Kawabata, Y., Ichiguchi, K., Ando, T., & Kato, T. Vesicle formations at critical vesicle concentration in a polyoxyethylene type nonionic surfactant system. *Colloids and Surfaces A: Physicochemical and Engineering Aspects*, **2014**, *462*, 179–185.

Kawabata, Y., Yashima, H., & Kato, T. 3D Structure of Lamellar Domains in a Surfactant Solution below the Krafft Temperature. *The Journal of Physical Chemistry B*, **2012**, *116*(5), 1593–1597.

Khadem, F., Pishvaei, M., Salami-Kalajahi, M., & Najafi, F. Morphology control of conducting polypyrrole nanostructures via operational conditions in the emulsion polymerization. *Journal of Applied Polymer Science*, **2017**, *134*(15).

Kim, H.-U., & Lim, K.-H. A model on the temperature dependence of critical micelle concentration. *Colloids and Surfaces A: Physicochemical and Engineering Aspects*, **2004**, *235*(1), 121–128.

Kumar, A., Shkir, M., Somaily, H. H., Singh, K. L., Choudhary, B. C., & Tripathi, S. K. A simple, low-cost modified drop-casting method to develop high-quality CH3NH3PbI3 perovskite thin films. *Physica B: Condensed Matter*, **2022**, *630*, 413678.

Kuperkar, K., Abezgauz, L., Danino, D., Verma, G., Hassan, P. A., Aswal, V. K., Varade, D., & Bahadur, P. Viscoelastic micellar water/CTAB/NaNO3 solutions: Rheology, SANS and cryo-TEM analysis. *Journal of Colloid and Interface Science*, **2008**, *323*(2), 403–409.

Le, T.-H., Kim, Y., & Yoon, H. Electrical and Electrochemical Properties of Conducting Polymers. *Polymers*, **2017**, *9*(4), Article 4.

Lee, H. L., Cheng, Y. S., Yeh, K. L., & Lee, T. A Novel Hydrate Form of Sodium Dodecyl Sulfate and Its Crystallization Process. *ACS Omega*, **2021**, *6*(24), 15770–15781.

Lertthanaphol, N., Prawiset, N., Soontornapaluk, P., Kitjanukit, N., Neamsung, W., Pienutsa, N., Chusri, K., Sornsuchat, T., Chanthara, P., Phadungbut, P., Seeharaj, P., Kim-Lohsoontorn, P., & Srinives, S. Soft template-assisted copper-doped sodium dititanate nanosheet/graphene oxide heterostructure for photoreduction of carbon dioxide to liquid fuels. *RSC Advances*, **2022**, *12*(37), 24362–24373.

Li, H., Mei, J., Ayzner, A. L., Toney, M. F., Tok, J. B.-H., & Bao, Z. A simple droplet pinning method for polymer film deposition for measuring charge transport in a thin film transistor. *Organic Electronics*, **2012**, *13*(11), 2450–2460.

Li, Y., Bober, P., Trchová, M., & Stejskal, J. Polypyrrole prepared in the presence of methyl orange and ethyl orange: Nanotubes versus globules in conductivity enhancement. *Journal of Materials Chemistry C*, **2017**, *5*(17), 4236–4245.

Lin, Q., Yang, Y., Ma, Y., Zhang, R., Wang, J., Chen, X., & Shao, Z. Bandgap Engineered Polypyrrole–Polydopamine Hybrid with Intrinsic Raman and Photoacoustic Imaging Contrasts. *Nano Letters*, **2018**, *18*(12), 7485–7493.

Liu, W., Kumar, J., Tripathy, S., & Samuelson, L. A. Enzymatic Synthesis of Conducting Polyaniline in Micelle Solutions. *Langmuir*, **2002**, *18*(25), 9696–9704.

Liu, Y.-C., & Hwang, B.-J. Identification of oxidized polypyrrole on Raman spectrum. *Synthetic Metals*, **2000**, *113*(1–2), 203–207.

Lone, M. S., Afzal, S., Chat, O. A., Aswal, V. K., & Dar, A. A. Temperature- and Composition-Induced Multiarchitectural Transitions in the Catanionic System of a Conventional Surfactant and a Surface-Active Ionic Liquid. *ACS Omega*, **2021**, *6*(18), 11974–11987.

Mahun, A., Abbrent, S., Bober, P., Brus, J., & Kobera, L. Effect of structural features of polypyrrole (PPy) on electrical conductivity reflected on 13C ssNMR parameters. *Synthetic Metals*, **2020**, *259*, 116250.

Makuła, P., Pacia, M., & Macyk, W. How To Correctly Determine the Band Gap Energy of Modified Semiconductor Photocatalysts Based on UV–Vis Spectra. *The Journal of Physical Chemistry Letters*, **2018**, *9*(23), 6814–6817.

Mal, A., Bag, S., Ghosh, S., & Moulik, S. P. Physicochemistry of CTAB-SDS interacted catanionic micelle-vesicle forming system: An extended exploration. *Colloids and Surfaces A: Physicochemical and Engineering Aspects*, **2018**, *553*, 633–644.

Mao, J., Li, C., Park, H. J., Rouabhia, M., & Zhang, Z. Conductive Polymer Waving in Liquid Nitrogen. *ACS Nano*, **2017**, *11*(10), 10409–10416.

Meng, M., & Lin, M. An electroanalytical sensor based on overoxidized polypyrrole-gold composite for the detection of tyramine in fermented food. *International Journal of Electrochemical Science*, **2023**, *18*(12), 100399.

Miah, M. R., Yang, M., Khandaker, S., Bashar, M. M., Alsukaibi, A. K. D., Hassan, H. M. A., Znad, H., & Awual, Md. R. Polypyrrole-based sensors for volatile organic compounds (VOCs) sensing and capturing: A comprehensive review. *Sensors and Actuators A: Physical*, **2022**, *347*, 113933.

Miao, J., Chen, Y., Li, Y., Cheng, J., Wu, Q., Ng, K. W., Cheng, X., Chen, R., Cheng, C., & Tang, Z. Proton Conducting Polyoxometalate/Polypyrrole Films and Their Humidity Sensing Performance. *ACS Applied Nano Materials*, **2018**, *1*(2), 564–571.

Molina, B. G., Cianga, L., Bendrea, A.-D., Cianga, I., Del Valle, L. J., Estrany, F., Alemán, C., & Armelin, E. Amphiphilic polypyrrole-poly(Schiff base) copolymers with poly(ethylene glycol) side chains: Synthesis, properties and applications. *Polymer Chemistry*, **2018**, *9*(31), 4218–4232.

Morávková, Z., Taboubi, O., Minisy, I. M., & Bober, P. The evolution of the molecular structure of polypyrrole during chemical polymerization. *Synthetic Metals*, **2021**, *271*, 116608.

Nagare, A. B., Harale, N. S., Dhas, S. D., Shembade, U. V., Ghatage, S. R., Patil, P. S., & Moholkar, A. V. Facile synthesis of nanogranular PPy thin films for sensitive and selective detection of toxic NO gas. *Inorganic Chemistry Communications*, **2022**, *146*, 110067.

Nah, J., Perkins, F. K., Lock, E. H., Nath, A., Boyd, A., Myers-Ward, R. L., Gaskill, D. K., Osofsky, M., & Rao, M. V. Electrical and Low Frequency Noise Characterization of Graphene Chemical Sensor Devices Having Different Geometries. *Sensors*, **2022**, *22*(3), Article 3.

Nakanishi, H., Tsuchiya, K., Ohkubo, T., Sakai, H., & Abe, M. Mechanism of Concentration-Dependent Vesicle-Micelle Transition in Aqueous Mixture of Cationic and Anionic Surfactants. *Journal of Oleo Science*, **2005**, *54*(8), 443–451.

O'Connor, A. J., Hatton, T. A., & Bose, A. Dynamics of Micelle−Vesicle Transitions in Aqueous Anionic/Cationic Surfactant Mixtures. *Langmuir*, **1997**, *13*(26), 6931–6940.

Oliveira, I., Silva, S., Do Vale, M., & Marques, E. Model Catanionic Vesicles from Biomimetic Serine-Based Surfactants: Effect of the Combination of Chain Lengths on Vesicle Properties and Vesicle-to-Micelle Transition. *Membranes*, **2023**, *13*(2), 178.

Omastová, M., Trchová, M., Kovářová, J., & Stejskal, J. Synthesis and Structural Study of Polypyrroles Prepared in the Presence of Surfactants. *Synthetic Metals*, **2003**, *138*, 447–455.

Pandey, R. K., Upadhyay, C., & Prakash, R. Pressure dependent surface morphology and Raman studies of semicrystalline poly(indole-5-carboxylic acid) by the Langmuir–Blodgett technique. *RSC Advances*, **2013**, *3*(36), 15712.

Pang, S.-K. Comprehensive study of polymerization of pyrrole: A theoretical approach. *Journal of Electroanalytical Chemistry*, **2020**, *859*, 113886.

Parayangattil Jyothibasu, J., & Lee, R.-H. Green synthesis of polypyrrole tubes using curcumin template for excellent electrochemical performance in supercapacitors. *Journal of Materials Chemistry A*, **2020**, *8*(6), 3186–3202.

Patil, A. O., Heeger, A. J., & Wudl, F. Optical properties of conducting polymers. *Chemical Reviews*, **1988**, *88*(1), 183–200.

Paúrová, M., Šeděnková, I., Hromádková, J., & Babič, M. Polypyrrole nanoparticles: Control of the size and morphology. *Journal of Polymer Research*, **2020**, *27*(12), 366.

Qin, G., & Qiu, J. Ordered polypyrrole nanorings with near-infrared spectrum absorption and photothermal conversion performance. *Chemical Engineering Journal*, **2019**, *359*, 652–661.

Rahman Poolakkandy, R., & Mol Menamparambath, M. Soft-template-assisted synthesis: A promising approach for the fabrication of transition metal oxides. *Nanoscale Advances*, **2020**, *2*(11), 5015–5045.

Ramanaviciene, A., Kausaite, A., Tautkus, S., & Ramanavicius, A. Biocompatibility of polypyrrole particles: An in-vivo study in mice. *Journal of Pharmacy and Pharmacology*, **2010**, *59*(2), 311–315.

Ravichandran, S., Nagarajan, S., Kokil, A., Ponrathnam, T., Bouldin, R. M., Bruno, F. F., Samuelson, L., Kumar, J., & Nagarajan, R. Micellar Nanoreactors for Hematin Catalyzed Synthesis of Electrically Conducting Polypyrrole. *Langmuir*, **2012**, *28*(37), 13380–13386.

Ren, H., Sun, R., Jin, Y., Xu, M., Pei, Y., Wang, Q., & Yan, M. Electrochemical Properties of Multi-Morphology Polypyrrole Electrode Materials Depended on Template Agents. *ChemistrySelect*, **2023**, *8*(37), e202302155.

Roohi, Z., Mighri, F., & Zhang, Z. A Simple Trick to Increase the Areal Specific Capacity of Polypyrrole Membrane: The Superposition Effect of Methyl Orange and Acid Treatment. *Polymers*, **2022**, *14*(21), 4693.

Salzner, U., Lagowski, J. B., Pickup, P. G., & Poirier, R. A. Comparison of geometries and electronic structures of polyacetylene, polyborole, polycyclopentadiene, polypyrrole, polyfuran, polysilole, polyphosphole, polythiophene, polyselenophene and polytellurophene. *Synthetic Metals*, **1998**, *96*(3), 177–189.

Samwang, T., Watanabe, N. M., Okamoto, Y., Srinives, S., & Umakoshi, H. Study of Chemical Polymerization of Polypyrrole with SDS Soft Template: Physical, Chemical, and Electrical Properties. *ACS Omega*, **2023**, *8*(51), 48946–48957.

Samwang, T., Watanabe, N. M., Okamoto, Y., & Umakoshi, H. Exploring the Influence of Morphology on Bipolaron–Polaron Ratios and Conductivity in Polypyrrole in the Presence of Surfactants. *Molecules*, **2024**, *29*(6), 1197.

Santos, M. J. L., Brolo, A. G., & Girotto, E. M. Study of polaron and bipolaron states in polypyrrole by in situ Raman spectroelectrochemistry. *Electrochimica Acta*, **2007**, *52*(20), 6141–6145.

Scott, J. C., Bredas, J. L., Yakushi, K., Pfluger, P., & Street, G. B. The evidence for bipolarons in pyrrole polymers. *Synthetic Metals*, **1984**, *9*(2), 165–172.

Šetka, M., Calavia, R., Vojkůvka, L., Llobet, E., Drbohlavová, J., & Vallejos, S. Raman and XPS studies of ammonia sensitive polypyrrole nanorods and nanoparticles. *Scientific Reports*, **2019**, *9*(1), Article 1.

Shabeeba, A., Rajan, L., Sidheekha, M. P., Thayyil, M. S., & Ismail, Y. A. Polypyrrole/hydrogel hybrid films as multi sensing supercapacitor electrodes. *Journal of Energy Storage*, **2022**, *55*, 105724.

Shen, X., Wei, X., Wang, T., Li, S., & Li, H. Polypyrrole embedded in nickel-cobalt sulfide nanosheets grown on nickel particles passivated silicon nanowire arrays for high-performance supercapacitors. *Chemical Engineering Journal*, **2023**, *461*, 141745.

Shinde, S. S., Gund, G. S., Dubal, D. P., Jambure, S. B., & Lokhande, C. D. Morphological modulation of polypyrrole thin films through oxidizing agents and their concurrent effect on supercapacitor performance. *Electrochimica Acta*, **2014**, *119*, 1–10.

Singh, D. V. K. Band Gap and Resistivity Measurements of Semiconductor Materials for Thin Films. *Journal of Emerging Technologies and Innovative Research*, **2017**, *4*(12).

Sravanthi, M., & Manjunatha, K. G. Synthesis and characterization of conducting polypyrrole with various dopants. *Materials Today: Proceedings*, **2021**, *46*, 5964–5968.

Suga, K., Otsuka, Y., Okamoto, Y., & Umakoshi, H. Gel-Phase-like Ordered Membrane Properties Observed in Dispersed Oleic Acid/1-Oleoylglycerol Self-Assemblies: Systematic Characterization Using Raman Spectroscopy and a Laurdan Fluorescent Probe. *Langmuir*, **2018**, *34*(5), 2081–2088.

Talens-Alesson, F. I., Hall, S. T., Hankins, N. P., & Azzopardi, B. J. Flocculation of SDS micelles with Fe3+. *Colloids and Surfaces A: Physicochemical and Engineering Aspects*, **2002**, *204*(1), 85–91.

Tang, F., Jiang, W., Xie, J., Zhao, D., Meng, Y., Yang, Z., Lv, Z., Xu, Y., Sun, W., & Jiang, Z. PPy-Coated Mo3S4/CoMo2S4 Nanotube-like Heterostructure for High-Performance Lithium Storage. *Molecules*, **2024**, *29*(1), Article 1.

Thompson, B. C., Moulton, S. E., Richardson, R. T., & Wallace, G. G. Effect of the dopant anion in polypyrrole on nerve growth and release of a neurotrophic protein. *Biomaterials*, **2011**, *32*(15), 3822–3831.

Trchová, M., & Stejskal, J. Resonance Raman Spectroscopy of Conducting Polypyrrole Nanotubes: Disordered Surface versus Ordered Body. *The Journal of Physical Chemistry A*, **2018**, *122*(48), 9298–9306.

Tumacder, D. V., Morávková, Z., & Bober, P. Enhanced electrochemical performance of electrosynthesized fibrillar polypyrrole film. *Materials Letters*, **2022**, *308*, 131295.

Veisi, H., Varshosaz, J., Rostami, M., & Mirian, M. Thermosensitive TMPO-oxidized lignocellulose/cationic agarose hydrogel loaded with deferasirox nanoparticles for photothermal therapy in melanoma. *International Journal of Biological Macromolecules*, **2023**, *238*, 124126.

Vernitskaya, T. V., & Efimov, O. N. Polypyrrole: A conducting polymer; its synthesis, properties and applications. *Russian Chemical Reviews*, **1997**, *66*(5), 443–457.

Vigmond, S. J., Ghaemmaghami, V., & Thompson, M. Raman and resonance-Raman spectra of polypyrrole with application to sensor – gas probe interactions. *Canadian Journal of Chemistry*, **1995**, *73*(10), 1711–1718.

Wang, J., Xu, S., Du, H., Zhang, Z., Lv, J., Sun, Y., & Wang, L. Mechanism research of SDBS-functionalized polypyrrole to improve electrochemical performance of screen-printed graphene electrode. *Electrochimica Acta*, **2023**, *454*, 142408.

Wang, Y., Song, R., Li, L., Fu, R., Liu, Z., & Li, B. High Crystalline Quality Conductive Polypyrrole Film Prepared by Interface Chemical Oxidation Polymerization Method. *Applied Sciences*, **2022**, *12*(1), Article 1.

Wang, Y., Wang, H., Zhang, W., Fei, G., Shu, K., Sun, L., Tian, S., Niu, H., Wang, M., Hu, G., & Duan, Y. A Simple Route to Fabricate Ultralong and Uniform Polypyrrole Nanowires with High Electrochemical Capacitance for Supercapacitor Electrodes. *ACS Applied Polymer Materials*, **2023**, *5*(2), 1254–1263.

Watanabe, N., Watase, S., Kadonishi, N., Okamoto, Y., & Umakoshi, H. Revealed Properties of Various Self-Assemblies in Two Catanionic Surfactant Systems in

Relation to Their Polarity and Molecular Packing State. *Langmuir*, **2022**, *38*(48), 14768–14778.

Weis, F., Thompson, R. F., & Jakobi, A. J. (Eds.). *Challenges and Solutions in Sample Preparation for High-Resolution Cryo-Electron Microscopy*. **2022**. Frontiers Media SA.

Weiss, T. M., Narayanan, T., & Gradzielski, M. Dynamics of Spontaneous Vesicle Formation in Fluorocarbon and Hydrocarbon Surfactant Mixtures. *Langmuir*, **2008**, *24*(8), 3759–3766.

Wen, J., Tian, Y., Mei, Z., Wu, W., & Tian, Y. Synthesis of polypyrrole nanoparticles and their applications in electrically conductive adhesives for improving conductivity. *RSC Advances*, **2017**, *7*(84), 53219–53225.

Xiaoqiang, L., Qian, S., Yan, K., Yanan, Z., Zengyuan, P., Yang, J., Mengjuan, L., & Chronakis, I. S. Self-powered humidity sensor based on polypyrrole modified melamine aerogel. *Materials Letters*, **2020**, *277*, 128281.

Xie, Y., Xu, J., Jin, H., Yi, Y., Shen, Y., Zhang, X., Liu, X., Sun, Y., Shi, W., He, Y., & Ge, D. Polypyrrole Nanosheets Prepared by Rapid In Situ Polymerization for NIR-II Photoacoustic-Guided Photothermal Tumor Therapy. *Coatings*, **2023**, *13*(6), Article 6.

Xing, S., & Zhao, G. Morphology, structure, and conductivity of polypyrrole prepared in the presence of mixed surfactants in aqueous solutions. *Journal of Applied Polymer Science*, **2007**, *104*(3), 1987–1996.

Yang, X., Lin, Z., Zheng, J., Huang, Y., Chen, B., Mai, Y., & Feng, X. Facile template-free synthesis of vertically aligned polypyrrole nanosheets on nickel foams for flexible all-solid-state asymmetric supercapacitors. *Nanoscale*, **2016**, *8*(16), 8650–8657.

Yang, Y., Jin, Y., He, H., Wang, Q., Tu, Y., Lu, H., & Ye, Z. Dopant-Induced Shape Evolution of Colloidal Nanocrystals: The Case of Zinc Oxide. *Journal of the American Chemical Society*, **2010**, *132*(38), 13381–13394.

Yu, H., Zhang, P., Chen, H., Yao, Y., Zhao, L., Zhao, M., Zhu, L., & Sun, H. Porous polypyrrole with a vesicle-like structure for efficient removal of per- and polyfluoroalkyl substances from water: Crucial role of porosity and morphology. *Journal of Hazardous Materials*, **2024**, *462*, 132748.

Yun, S.-R., Kim, G.-O., Lee, C. W., Jo, N.-J., Kang, Y., & Ryu, K.-S. Synthesis and Control of the Shell Thickness of Polyaniline and Polypyrrole Half Hollow Spheres Using the Polystyrene Cores. *Journal of Nanomaterials*, **2012**, *2012*, 1–9.

Yussuf, A., Al-Saleh, M., Al-Enezi, S., & Abraham, G. Synthesis and Characterization of Conductive Polypyrrole: The Influence of the Oxidants and Monomer on the Electrical, Thermal, and Morphological Properties. *International Journal of Polymer Science*, **2018**, *2018*, 1–8.

Zang, L., Liu, Q., Qiu, J., Yang, C., Wei, C., Liu, C., & Lao, L. Design and Fabrication of an All-Solid-State Polymer Supercapacitor with Highly Mechanical Flexibility Based on Polypyrrole Hydrogel. *ACS Applied Materials & Interfaces*, **2017**, *9*(39), 33941–33947.

Zhang, X., Zhang, J., Song, W., & Liu, Z. Controllable Synthesis of Conducting Polypyrrole Nanostructures. *The Journal of Physical Chemistry B*, **2006**, *110*(3), 1158–1165.

Zhou, M., Pagels, M., Geschke, B., & Heinze, J. Electropolymerization of Pyrrole and Electrochemical Study of Polypyrrole. 5. Controlled Electrochemical Synthesis and Solid-State Transition of Well-Defined Polypyrrole Variants. *The Journal of Physical Chemistry B*, **2002**, *106*(39), 10065–10073.

Zhou, Z., Shao, Y., Gao, X., Liu, Z., & Zhang, Q. Structural regulation of polypyrrole nanospheres guided by hydrophobic chain length of surfactants. *Journal of Materials Science*, **2019**, *54*(23), 14309–14319.

Zoromba, M. S., Abdel-Aziz, M. H., Bassyouni, M., Abusorrah, A. M., Attar, A., Baghdadi, N., & Salah, N. Polypyrrole sheets composed of nanoparticles as a promising room temperature thermo-electric material. *Physica E: Low-Dimensional Systems and Nanostructures*, **2021**, *134*, 114889.

List of Publications

[Papers]

(1) Thaneeya Samwang, Nozomi Morishita Watanabe, Yukihiro Okamoto, Sira Srinives, and Hiroshi Umakoshi, Study of Chemical Polymerization of Polypyrrole with SDS Soft Template: Physical, Chemical, and Electrical Properties.
ACS Omega, **8 (51)**, 48946-48957 (2023).

(2) Thaneeya Samwang, Nozomi Morishita Watanabe, Yukihiro Okamoto, and Hiroshi Umakoshi, Exploring the Influence of Morphology on Bipolaron–Polaron Ratios and Conductivity in Polypyrrole in the Presence of Surfactants.
Molecules, **29 (6)**, Article ID: 1197 (16 pages) (2024).

(3) Thaneeya Samwang, Nozomi Morishita Watanabe, Yukihiro Okamoto, and Hiroshi Umakoshi, Tailoring Polypyrrole Morphology and Electronic Properties through CTAB-SDS Self-Assembly.
Colloids and Surfaces A, **704**, Article ID: 135527 (12 pages) (2024).

[Symposium]

(1) Thaneeya Samwang, Nozomi Morishita Watanabe, Yukihiro Okamoto, and Hiroshi Umakoshi. Relation between size, morphology, electrical properties, and the bipolarons/polarons ratio of PPy in the presence of SDS. *The SCEJ 89th Annual Meeting International Chemical Engineering Symposia 2024*, Osaka, Japan. March (2024). (Poster)

(2) Thaneeya Samwang, Nozomi Morishita Watanabe, Yukihiro Okamoto, and Hiroshi Umakoshi. Investigating the Relationship in Morphology Impact on B/P Ratios and Conductivity in Polypyrrole Synthesis with Surfactants. *The SCEJ 55th Autumn Meeting*, Hokkaido, Japan, September (2024). (Poster)

[Awards]

(1) Scholarship for academic and supportive staff mobility (Mahidol University, Thailand, 2021).

(2) Royal Thai Government scholarship for study in PhD (Thailand, 2021).

Acknowledgement

The author extends her deepest gratitude to Prof. Dr. Hiroshi Umakoshi (Division of Chemical Engineering, Graduate School of Engineering Science, Osaka University) for his insightful comments, guidance, inspiration and warm encouragement throughout this work. She is also profoundly thankful to Prof. Dr. Norikazu Nishiyama, Prof. Dr. Tomoo Mizugaki (Division of Chemical Engineering, Graduate School of Engineering Science, Osaka University), and Assoc. Prof. Dr. Sira Srinives (Department of Chemical Engineering, Faculty of Engineering, Mahidol University) for their invaluable comments and suggestions, which greatly contributed to the completion of this thesis. The author also expresses her sincere thanks to Assoc. Prof. Dr. Ryohei Kishi (Division of Chemical Engineering, Graduate School of Engineering Science, Osaka University) for his valuable feedback and support during her presentation. Additionally, she is grateful to Assoc. Prof. Dr. Yukihiro Okamoto (Division of Chemical Engineering, Graduate School of Engineering Science, Osaka University) for his unwavering encouragement and comments in advancing this research. Special appreciation goes to Assist. Prof. Dr. Nozomi Morishita Watanabe (Division of Chemical Engineering, Graduate School of Engineering Science, Osaka University) for her invaluable comments and guidance throughout this study and for her support during the author's stay in Japan. The author is also deeply thankful to Ms. Keiko Fukumoto for her continuous support throughout her studies.

The author extends her heartfelt gratitude to Prof. Dr. Y. Kitagawa, Prof. Dr. Y. Okano, Prof. Dr. T. Hirai, Prof. Dr. N. Matsubayashi, Prof. Dr. S. Sakai and all the staff of Division of Chemical Engineering, Graduate School of Engineering Science, Osaka University for their invaluable cooperation throughout this research. She is also deeply appreciative of the support provided by the staff of the graduate section during her studies.

She also expresses her sincere appreciation to Dr. T. Takehara (Comprehensive Analysis Center, ISIR, Osaka University) and extends special thanks to Prof. Dr. K. Mitsuoka and Ms. A. Saitoh (Research Center for Ultra-High Voltage Electron Microscopy, Osaka University) for their invaluable assistance and collaboration.

The author is deeply grateful to Asst. Prof. Dr. W. Koo-amornpattana and Assoc. Prof. Dr. C. Sakdaronnarong (Department of Chemical Engineering, Faculty of Engineering, Mahidol University), and Assoc. Prof. Dr. Jackrit Suthakorn (Department of Biomedical Engineering, Faculty of Engineering, Mahidol University), and all the staff of the Faculty of Engineering, Mahidol University, for their generous support and encouragement. Special gratitude is extended to Assist. Prof. Dr. Bovonlak Oonkhanon, her former advisor, for his invaluable assistance and encouragement throughout this work.

The author expresses her gratitude to N. Nakanishi, H. Ishikawa, and N. Natsukawa for their invaluable assistance. Special thanks are extended to her colleagues and team members for their collaboration and constant support: Ni'matul Izza, M. Watanabe, W. Wakileh, Endang Ciptawati, S. Suankhem, N. Ito, N. Kadonishi, N. Fukuda, Y. Fujiyama, L. Junghu, A. Ajaikumar, Z. Nicolella, H. Takase, S. Watase, K. Hamaguchi, Y. Nagamura, Y. Niwa, T. Ozawa, Y. Suzaki, A. Suzuta, S. Sogabe, J. Nakamura, L. Weiyu, N. Yoshioka, K. Chatani, K.Watanabe, Y. Amatsu, K. Miura, K. Yamaguchi, D. Imanaka, K. Ogawa, A. Tsutsui, C. Inoue, S. Asano, D. Lim, PG. Deng, R. Xuehui and all members of the Bio-inspired Chemical Engineering (B-ICE) Laboratory. She would also like to extend her heartfelt appreciation to B-ICE Laboratory for providing the resources and facilities essential to this research.

The author wishes to thank her dear friends in Japan and Thailand: P. Soontornapaluk, P. Chantachotikul, M. Kalong, P. Massa-ard, W. Chamnansuta, and Dr. V. Raksanoh, as well as many others too numerous to mention individually, for their care and encouragement. She is grateful to her partner for his unwavering love and support throughout her studies. The author extends her most profound appreciation to her parents, P. Samwang and B. Samwang, and her entire family for their unconditional love, support, and patience during the challenging times, which provided the motivation and inspiration to complete her studies in Japan.

Lastly, the author acknowledges the Royal Thai Government Scholarship, Thailand, for their financial support during her studies in Japan and appreciates the administrative staff for their assistance throughout the process.